BROOKHAVEN NATIONAL LABORATORY

24 May 1996 BNL – 63158

The NLC ZDR Design Group and the NLC Physics Working Groups

Physics Goals of the Next Linear Collider*

S. Kuhlman *et al.*

(see list, pgs. 1 and 2)

and

William J. Marciano

Physics Department
Brookhaven National Laboratory
Upton, New York 11973

* Working Group notes

The NLC ZDR Design Group and the NLC Physics Working Groups

S. Kuhlman; *Argonne National Laboratory*

W. Marciano; *Brookhaven National Laboratory*

J. F. Gunion, T. Han, S. Lidia; *University of California, Davis, Davis, California, USA*

J. Rosenzweig; *University of California, Los Angeles, Los Angeles, California, USA*

J. Wudka; *University of California, Riverside*

N. Kroll; *University of California, San Diego, San Diego, California, USA*

D. A. Bauer, H. Nelson; *University of California, Santa Barbara*

H. Haber, C. Heusch, B. Schumm; *University of California, Santa Cruz*

M. Gintner, S. Godfrey, P. Kalyniak; *Carleton University*

A. Barker, M. Danielson, S. Fahey, M. Goluboff, U. Nauenberg, D. L. Wagner; *University of Colorado*

P. C. Rowson; *Columbia University*

J. Holt, K. Maeshima, R. Raja; *Fermilab National Laboratory, Batavia, Illinois, USA*

H. Baer, R. Munroe; *Florida State University*

X. Tata; *University of Hawaii*

R. van Kooten; *Indiana University*

John Byrd, S. Chattopadhyay, J. Corlett, W. Fawley, J. L. Feng, M. Furman, E. Henestroza, R. Jacobsen, K.-J. Kim, H. Li, H. Murayama, L. Reginato, R. Rimmer, D. Robin, M. Ronan, A. Sessler, D. Vanecek, J. Wurtele, M. Xie, S. Yu, A. Zholents; *Lawrence Berkeley National Laboratory, Berkeley, California, USA*

K. Bibber, D. Clem, F. Deadrick, T. Houck, D. E. Klem, M. Perry, G. Westenskow; *Lawrence Livermore National Laboratory, Livermore, California, USA*

B. Barakat; *Louisiana Tech University*

S. Hertzbach; *University of Massachusetts, Amherst, Massachusetts, USA*

A. Dragt, R. Gluckstern; *University of Maryland, College Park, Maryland, USA*

P. Burrows, M. Fero; *Massachusetts Institute of Technology*

M. Einhorn, G. L. Kane, K. Riles; *University of Michigan*

G. B. Cleaver, K. Tanaka; *Ohio State University*

J. Brau, R. Frey, D. Strom; *University of Oregon*

K. McDonald; *Princeton University*

G. Couture; *Université de Quebec à Montreal*

R. Hollebeek; *University of Pennsylvania*

D. Meyerhofer; *University of Rochester, Rochester, New York, USA*

C. Adolphsen, R. Aiello, R. Alley, R. Assmann, K. L. Bane, T. Barklow, J. Bogart, G. Bowden, G. Bower, M. Breidenbach, K. Brown, D. Burke, Y. Cai, G. Caryotakis, R. Cassel, P. Chen, S. Clark, J. Clendenin, C. Corvin, F.-J. Decker, A. Donaldson, R. Dubois, S. Ecklund, J. Eichner, P. Emma, L. Eriksson, Z.D. Farkas, A. Fisher, W.R. Fowkes, J. Frisch, L. Genova, S. Gold, G. Gross, S. Hanna, S. Hartman, S. Heifets, L. Hendrickson, R. Helm, J. Hewett, H.A. Hoag, J. Hodgson, J. Humphrey, R. Humphrey, J. Irwin, J. Jaros, R. K. Jobe, R. Jones, L. Keller, K. Ko, R.F. Koontz, E. Kraft, P. Krejcik, A. Kulikov, T. L. Lavine, Z. Li, W. Linebarger, G.A. Loew, T. Markiewicz, T. Maruyama, T. Mattison, B. McKee, R. Messner, R.H. Miller, M. Minty, M. Munro, R. Nelson, C. Ng, Y. Nosochkov, D. Palmer, J.M. Paterson, C. Pearson, M. E. Peskin, R. M. Phillips, N. Phinney, R. Pope, T. O. Raubenheimer, J. Rifkin, T. Rizzo, S. Rokni, M.C. Ross, R. Ruland, R.D. Ruth, A. Saab, H. Schwarz, B. Scott, J. Sheppard, H. Shoaee, S. Smith, W. Spence, C. Spencer, J. Spencer, D. Sprehn, G. Stupakov, H. Tang, S.G. Tantawi, P. Tenenbaum, F. Tian, S. Thomas, K. A. Thompson, J. Turner, T. Usher, A. Vlieks, D. Walz, J.W. Wang, A. Weidemann, D. Whittum, P. B. Wilson, Z. Wilson, M. Woodley, M. Woods, Y. Yan, D. Yeremian, F. Zimmermann; *Stanford Linear Accelerator Center, Stanford, California, USA*

B. F. L. Ward, A. Weidemann *University of Tennessee*

L. Sawyer, A. White *University of Texas, Arlington*

C. Baltay, S. Manly *Yale University*

M. Akemoto, T. Higo, K. Higashi, K. Kubo, K. Oide, K. Yokoya; *KEK National Laboratory, Tsukuba, Japan*

L. Rinolfi; *CERN, Geneva, Switzerland*

V. Telnov; *Budker Institute for Nuclear Physics, Novosibirsk, Russia*

T. Takahashi, T. Ohgaki; *Hiroshima University, Hiroshima, Japan*

G. Giordano; *University of Milano, Milan, Italy*

F. Cuypers; *Paul Scherrer Institute*

P. Minkowski; *University of Bern*

DISCLAIMER

PREFACE

We present the prospects for the next generation of high-energy physics experiments with electron-positron colliding beams. This report summarizes the current status of the design and technological basis of a linear collider of center of mass energy 500 GeV–1.5 TeV, and the opportunities for high-energy physics experiments that this machine is expected to open.

Over the past two decades, particle physics experiments have made an increasingly precise confirmation of the "Standard Model" of strong, weak, and electromagnetic interactions. High-energy physicists now feel confident that the basic structure of these once-mysterious interactions of elementary particles is now well understood. But the verification of this model has brought with it the realization that there is a missing piece to the story: The structure of the weak interactions is based on a symmetry principle, but we observe that symmetry to be broken, by an agent that we do not yet know. This agent, whatever its source, must provide new physical phenomena in the energy region between a few hundred GeV and 1 TeV.

The Large Hadron Collider (LHC) in Europe offers an entry into this energy regime with significant opportunity for discovery of new phenomena. An electron-positron collider at this next step in energy, the Next Linear Collider (NLC), will provide a complementary program of experiments with opportunities for both discovery and precision measurement. To understand the nature of the new phenomena at the TeV scale, to see how they fit together with the known particles and interactions into a grander picture, both of these facilities will be required.

In particular, electron-positron colliders offer specific features that are essential to understand the nature of these new interactions whatever their source. They allow precise and detailed studies of the two known particles that couple most strongly to these interactions, the W boson and the top quark. They provide a clean environment for the discovery of new particles whatever their nature, and they provide special tools, such as the use of electron beam polarization, to dissect the couplings of those particles.

All of this would be merely theoretical if the next-generation linear collider could not be realized. But, in the past few years, the technology of the linear collider has come of age. The experience gained from the operation of the Stanford Linear Collider (SLC) has provided a firm foundation on which to base the design and technology choices for the NLC. The fundamental new technologies needed to construct the NLC have been demonstrated experimentally. Microwave RF power sources have exceeded requirements for the initial stage of the NLC, and critical tests assure us that this technology can be expected to drive beams to a center of mass energies of a TeV or more. Essential demonstrations of prototype collider subsystems have either taken place or are now underway: The Final Focus Test Beam, has already operated successfully; a prototype linear accelerator and a prototype damping ring will be operated within the next year. A detailed engineering study, the Zeroth-Order Design Report (ZDR), has demonstrated that these components can be integrated into a complete machine design.

These reports provide a summary of both of these aspects of the linear collider project. Chapter 1 gives an overview of the NLC project and describes the genesis of this document. Chapter 2 gives a survey of models of new physics at the electroweak scale and presents, case by case, the unique and crucial experiments that the NLC will supply. Chapter 3 gives a summary of the ZDR and the status of the linear collider technology.

The Next Linear Collider can be constructed, and it will play an essential role in our understanding of physics at the TeV energy scale. It is time to begin the task of making this project a reality.

Physics Goals of the Next Linear Collider

May 19, 1996

TABLE OF CONTENTS

Physics Goals of the Next Linear Collider

0.1 Introduction

During the past several decades, significant advances have been made in elementary particle physics. We now have a renormalizable quantum field theory of strong and electroweak interactions, based on the principle of local $SU(3)_c \times SU(2)_L \times U(1)_Y$ gauge invariance. That theory properly describes the interactions of all known particles, incorporating the proven symmetries and successes of quantum electrodynamics, the quark model, and low energy V-A theory. It correctly predicted weak neutral currents, the now observed gluons and weak gauge bosons, and the special properties of the heavy fermions τ, b, and t. Since it is a renormalizable theory, its predictions can be tested at the quantum loop level by high precision experiments. It has already confronted a wealth of data at the level of 1% or better without any significant evidence of inconsistency. Because of those impressive successes, the $SU(3)_c \times SU(2)_L \times U(1)_Y$ theory has been given the title "The Standard Model", a designation which establishes it as the paradigm against which future experimental findings and new theoretical ideas must be compared.

The Standard Model cannot be the final theory of Nature, but it does represent the completion of a major stage toward the uncovering of that theory. To make further progress, we must examine both the strengths and failings of this model and direct experimental effort toward the weakest points in its structure.

The Standard Model is based on the interactions of fermions and vector gauge bosons. The fermions are grouped into three generations of leptons and quarks which span an enormous mass range. Their newest member, the top quark, is exceptionally heavy. Why is the top so massive, or why are the other fermions so light? This question highlights the broader problem of why Nature chose to repeat the fermion generations three times and endow quarks and leptons with their observed pattern of masses and mixing. It is likely that future intense scrutiny of the top quark's properties will provide new insights regarding this important problem.

The vector bosons of the Standard Model are grouped into eight massless gluons of $SU(3)_c$ which mediate the strong interactions, plus the $W^{\pm}$, Z, and γ which are responsible

for electroweak interactions. The $SU(3)_c$ gauge theory, called quantum chromodynamics (QCD), taken on its own, is an ideal theory. It has no arbitrary or free parameters but can, in principle, explain all hadronic dynamics including confinement, asymptotic freedom, proton structure, and baryon and meson spectroscopy. Confirming those properties and uncovering additional more subtle features of QCD remains an important experimental and theoretical challenge.

In contrast with QCD, the electroweak sector has many arbitrary parameters. Most stem from the Higgs mechanism which is used to break the $SU(2)_L \times U(1)_Y$ symmetry and endow particles with mass. In the simplest realization of this symmetry breaking, one introduces a scalar doublet ϕ, the Higgs field, which obtains a vacuum expectation value v. This assumption introduces into the theory an electroweak mass scale $v \simeq 250$ GeV. The masses of the W and Z bosons and the various quarks and leptons are proportional to v. Their disparity reflects extreme differences in their couplings to the scalar field ϕ. It is true that this simple model with one Higgs field can parametrize all electroweak masses, quark mixing, and even CP violation. But it does not provide insight into any of these phenomena, or even into the basic fact that the electroweak gauge symmetry is spontaneously broken. The many unanswered questions associated with the Higgs field, or whatever more complicated structure leads to the breaking of the electroweak symmetry, call for experiments which thoroughly explore this sector.

An important testable prediction of the simple Higgs model is the existence of a neutral spin-0 remnant particle H, called the Higgs scalar. Its mass depends on the self-coupling λ of the Higgs field through the relation

$$m_H = \sqrt{2\lambda} v \ , \tag{0.1}$$

but it is unspecified as long as λ is unknown. There is an experimental lower bound on m_H of 65 GeV from direct searches at LEP. That search reach is expected to be extended up to about 90 GeV at LEP II. There is also an approximate upper bound on the Higgs mass $m_H \lesssim 800$ GeV from theoretical bounds on λ. For example, perturbative partial wave unitarity in high energy scattering of longitudinal W bosons, $W_L W_L \to W_L W_L$ requires $|\lambda| \lesssim 8\pi/5$. This gives a large window in which to search. However, there is a much stronger upper bound which comes from the stronger assumption that the Higgs boson is a fundamental particle with no nonperturbative interactions up to the grand unification scale. This requires $m_H \lesssim 200$ GeV; we will refer to a Higgs boson satisfying this hypothesis as a 'light Higgs'.

Even more daunting than the problem of finding the Higgs boson H in the context of the simple Higgs theory is the prospect that this theory is inadequate to correctly describe the weak interaction scale. This simplest theory has theoretical problems of self-consistency, particularly when it is extrapolated to a unified theory at high energies. Also, the fact that its pattern of couplings must be input without any explanation is a sign that this theory is only a parametrization of electroweak symmetry breaking rather than being a fundamental explanation of this phenomenon. This state of affairs has led to many speculations on the true symmetry breaking mechanism and, from there, to interesting new physics possibilities beyond the Standard Model with observable manifestations at high energy.

In order to build a theory in which electroweak symmetry is naturally broken by the expectation value of a fundamental Higgs field, it is necessary to incorporate supersymmetry (SUSY) at the weak interaction scale. That elegant boson-fermion symmetry allows a simple connection to gauge or string theory unification and provides a logic for the symmetry-breaking form of the Higgs potential. Achieving these goals, howver, requires introducing novel partners for all Standard Model particles. It also requires at least two Higgs doublets and thus predicts five remnant scalars, h, H, A, $H^{\pm}$. The h should have a mass below about 150 GeV and should be most similar to the Standard Model Higgs boson. Finding that particle and determining its properties may be our first window to supersymmetry. If supersymmetry does indeed appear below 1 TeV, there will be a wealth of supersymmetry partner spectroscopy waiting to be explored. Currently, supersymmetry has no direct experimental support. However, there are two pieces of evidence that are very suggestive in favor of this theory. The first is the values of the $SU(3) \times SU(2) \times U(1)$ coupling constants, now measured with precision at Z^0 energies. These coupling constants are in just the relation predicted by a supersymmetric grand unified theory. The second is the tendency of the precision electroweak data to favor a light Higgs boson, which is an indication that the mechanism of electroweak symmetry breaking involves weakly-coupled fields.

Alternatively, one might imagine that there is no fundamental Higgs field, and that the electroweak symmetry is broken dynamically by fermion-antifermion condensation due to new strong forces at high energy. Scenarios ranging from $t\bar{t}$ condensation to complex extended technicolor models have been proposed. Their basic premise is very appealing, but no compelling model exists. Nevertheless, the generic idea of new underlying strong dynamics gives rise to testable consequences for anomalous top and gauge boson couplings and high energy scattering behavior.

This issue of whether the mechanism of electroweak symmetry breaking is weak-coupling or strong coupling is the most important question in elementary particle physics today. The NLC should resolve it definitively. For the case in which this physics is weak-coupling, the NLC should have a rich experimental program involving the detailed study of Higgs bosons and supersymmetric particles. The precise spectrum and branching ratio determinations for these particles should give information which, like the values of the strong and electroweak coupling constants, can be extrapolated to the unification scale. This scenario offers the tantalizing possibility that experimental data collected at the NLC would be directly relevant to supergravity and superstring theories at very high energy. On the other hand, if the mechanism of electroweak symmetry breaking is strong-coupling, this could imply a new spectroscopy at the TeV energy scale which the NLC might access directly.

In addition to these two options which relate directly to the physics of electroweak symmetry breaking, there are many other possibilities for new physics at the TeV energy scale. These include larger gauge groups with additional W' and Z' gauge bosons, heavy new fermions, and additional scalars. Many of these possibilities are realized in specific models of electroweak symmetry breaking, so a broad-based search for new phenomena is an essential part of the experimental program devoted to this question. The most direct way to uncover such new particles and their associated phenomena is to search at very high energies above

particle production threshold. Important indirect evidence can also be inferred from precision studies of Standard Model parameters such as m_W, $\sin^2\theta_W$, and the couplings of heavy quarks and W bosons to the γ and Z^0.

For the exploration of all of these possibilities, which defines the next step in experimental high-energy physics, the Next Linear Collider (NLC) will play an essential role. We envisage this machine as an e^+e^- collider which operates initially at a center of mass energy of about 500 GeV and can be upgraded to 1.5 TeV, providing a luminosity corresponding to 10^4 events per year for a process with the point cross section for QED pair production. This machine will employ polarized electrons and offers the possibility of e^-e^-, $e\gamma$, and $\gamma\gamma$ collider options. With such a facility, it is possible to carry out crucial and unique experiments across the whole range of possibilities we have just described for the physics of the weak interaction scale. In this report, we will summarize the capabilities of the NLC to explore the physics of the weak interaction scale across this broad front.

A design for the NLC is presented in an accompanying report, the *Zeroth Order Design Report* (ZDR) [1]. Chapter 2 of this report gives a summary of the ZDR and an explanation of its design strategy. In Section 2 of this chapter, we will summarize the basic conclusions of this report relevant to the physics studies, including the basic accelerator parameters of energy and luminosity. We will also describe the basic assumptions on detector performance that we will use to describe the physics capabilities of this machine. In Sections 11 and 12, after our discussion of the physics opportunities that the NLC will provide, we will give a more detailed description of a detector design and the constraints on the detector which come both from the physics goals and from the accelerator.

One of the first physics goals of the NLC will be the detailed study of the top quark at its threshold and just above. We will explain in Section 3 the special features of the $t\bar{t}$ threshold region which make it a unique laboratory for the precision measurement of the top mass and width, the QCD coupling of the top quark, and the possible couplings to the Higgs boson and other new particles. We will also describe how the NLC will make precision measurements of the couplings of top to electroweak gauge bosons, couplings which might contain signals of new strong interactions which connect top to the sector responsible for electroweak symmetry breaking.

Whether the electroweak gauge symmetry is broken by fundamental Higgs bosons or by new high-energy strong interactions, the NLC will bring important contributions to the experimental study of this sector. First of all, though the LHC and other facilities have the capability to find a light Higgs boson in many decay channels, the NLC is the only planned facility at which the existence of a light Higgs boson can be ruled out in a model-independent way. If the light Higgs boson is indeed present, we will show in Section 4 that the NLC will be able not only to discover this particle but also to characterize many of its interactions. We will show that the NLC has a unique capability to determine the couplings of the Higgs boson to Z and W, to heavy quarks and leptons, and to photons. These measurements dovetail nicely with the expected measurement of the Higgs production cross section from gluon fusion at the LHC to give the complete phenomenological profile of this particle.

If the presence of a relatively light fundamental Higgs particle is accompanied by the appearance of supersymmetry at the TeV scale, the NLC can perform crucial experiments to characterize the new supersymmetric particles. We will show in Section 5 that the NLC can detect the supersymmetric partners of W and Z over essentially the complete range of parameters expected in the model. But, even more importantly, the NLC can measure the masses and mixing angles of these particles and, in so doing, determine the most important underlying parameters of supersymmetry. This determination of parameters will be essential not only for the exploration of the physics of fermion partners at e^+e^- colliders, but also for the extraction of detailed information about the underlying theory from the complementary signatures of supersymmetry seen at hadron colliders.

If electroweak gauge symmetry is broken by new forces at high energy, one can look for the signs of these forces in the couplings of W bosons to the γ and Z and in the study of WW scattering. We will show in Section 6 that the NLC is an ideal machine for the study of the gauge couplings of the W, capable of achieving parts per mil precision on the W form factors. We will show in Section 7 that the NLC at the high end of its energy range can achieve constraints on WW scattering comparable to those of the LHC, in an environment with a number of qualitative advantages. We will also show that the NLC also offers new windows into WW interactions through the precision study of $e^+e^- \to W^+W^-$ and through high-energy $t\bar{t}$ production.

Finally, these capabilities of the NLC to explore specific models of electroweak symmetry breaking are balanced by the ability of this facility to perform broad searches for novel fermions, scalars, and gauge bosons. We will describe the abilities of the NLC to search for exotic particles in e^+e^- annihilation in Section 8. In Section 9, we will show how this broad capability is extended further by the availability of e^-e^-, $e\gamma$, and $\gamma\gamma$ collisions. In Section 10, we will show that the NLC will also contribute to the future program in the study of the strong interactions, in particular, through the precision measurement of α_s.

Section 14 will present our conclusions. We will review the unique capabilities of the NLC and contrast its prospects with those of the next generation of hadron colliders.

0.2 Standard Model Processes and Simulations

We begin by describing the basic assumptions underlying our study of the physics capabilities of the NLC. We will briefly discuss the expected energy and luminosity that the NLC will provide, the performance of the detector that we expect to have available, our simulation methods, and the magnitudes of the most important standard model background processes.

0.2.1 Accelerator and Detector

The NLC is envisaged as the first full-scale e^+e^- linear collider, a machine designed from the beginning with the goal of high-luminosity colliding beam physics and one which takes

account of the lessons of its prototype, the SLC. The NLC will be designed for an initial energy of 500 GeV in the center of mass, with an upgrade path to 1.5 TeV. It will provide a luminosity sufficient for a thorough experimental program on e^+e^- annihilation to standard and exotic particle pairs. It will provide a highly polarized e^- beam, and possibly also a polarized positron beam. Our basic assumptions on luminosity as a function of energy and on polarization are given in Table 0.1. These assumptions are justified in the description of the accelerator design given in Chapter 3 of this report and, at greater length, in [1].

Table 0.1: Basic Parameters of the Next Linear Collider

Energy (GeV)	Luminosity ($cm^{-2}s^{-1}$)	
500 GeV	5×10^{33}	
1000 GeV	1×10^{34}	
1500 GeV	1×10^{34}	
Polarization:		
	80% e^-, 0% e^+	Initial
	90% e^- 65% e^+	Possible

The NLC experiments can be carried out with a standard 4π multipurpose detector similar to those at LEP or SLC. In our concept of this detector, we include some innovations such as all-silicon tracking to minimize the effect of machine-related backgrounds, but for the most part the demands we have made on the detector are straightforwardly met. The essential performance assumptions we have made are shown in Table 0.2. Because of the small beam spot sizes at a linear collider, which allows us to bring a CCD vertex detector within 2 cm of the interaction point, the detector should have excellent b-tagging capabilities. The assumed curve of efficiency versus purity for b-tagging is shown in Fig. 0.1.

0.2.2 Simulations

In the studies presented here, the detector model has been used in concert with a set of familiar and newly-written simulation programs. In general, the background processes were generated by PYHTIA 5.7 [5], except for the background from $e^+e^- \to W^+W^-$, which plays an especially important role at linear collider energies. For this process we used a new generator [6] which is based on the formalism for this reaction presented by Hagiwara *et al.* [7]. This generator computed the total amplitude for W^+W^- production and subsequent decay to four fermions, retaining the full spin correlations through the process. It did make the approximation of treating the W's as on-shell particles, but it properly treated the effects of initial state electron polarization, beamstrahlung, collinear multi-photon initial state bremsstrahlung, and a nonzero W boson decay width. The same Monte Carlo program was used in the studies of nonstandard W physics reported in Sections 6 and 7. Many of the

Table 0.2: Summary of the detector parametrization used in the simulations.

Particle	Energy	Momentum
Electrons	$\frac{\delta E}{E} = \frac{12\%}{\sqrt{E}} + 1.0\%$ $E_s = E + \delta E$	$P_s^2 = E_s^2 - m_e^2$
Photons	$\frac{\delta E}{E} = \frac{12\%}{\sqrt{E}} + 1.0\%$ $E_s = E + \delta E$	$P_s = E_s$
Neutral Hadrons	$\frac{\delta E}{E} = \frac{45\%}{\sqrt{E}} + 2.0\%$ $E_s = E + \delta E$	$P_s^2 = E_s^2 - m_\pi^2$
Charged Hadrons	$E_s^2 = P_s^2 + m_\pi^2$	$\frac{\delta P_{x,y}}{P_{x,y}^2} = 0.0005 \oplus \frac{0.0015}{P_{x,y}\sqrt{P}(\sin\theta)^{2.5}}$ $\frac{\delta P_z}{P_z^2} = \frac{0.0015}{P_{x,y}\sqrt{P}(\sin\theta)^{2.5}}$ $(P_s)_i = P_i + \delta P_i$

Smeared quantities are denoted in the table by a subscript s.

other analyses used specialized generators at this level of sophistication to simulate the new physics processes. These are described in the various sections of this report. Except where it is reported otherwise, the hadronization of partons and subsequent decays were performed by JETSET 7.4 [5].

Four-vectors of stable particles emerging from the simulated reaction were adjusted by a detector resolution smearing routine, which implemented the parametrization summarized in Table 0.2. All quantities were parametrized as a function of theta. The smearing assumed Gaussian errors and populated tails out to 3.5σ. The parametrization assumed a dead cone about the beampipe of 150 mrad ($\cos\theta = 0.99$). The neutral particle and charged particle detection efficiencies were each taken to be 98%. For neutral hadrons, the momentum directions were Gaussian smeared in a cone about the original direction with a half-width of 15 mrad to simulate finite directional resolution. For photons and electrons, the directions were smeared by a cone of half-width 10 mrad.

0.2.3 Standard Model Processes at the NLC

Standard model processes, in addition to being interesting in their own right, are the background to searches for new physics at the NLC. Many of the standard model reactions at the NLC are familiar at lower energies and need only be extrapolated to higher energies. However, new processes, such as the pair production of gauge bosons, emerge as dominant

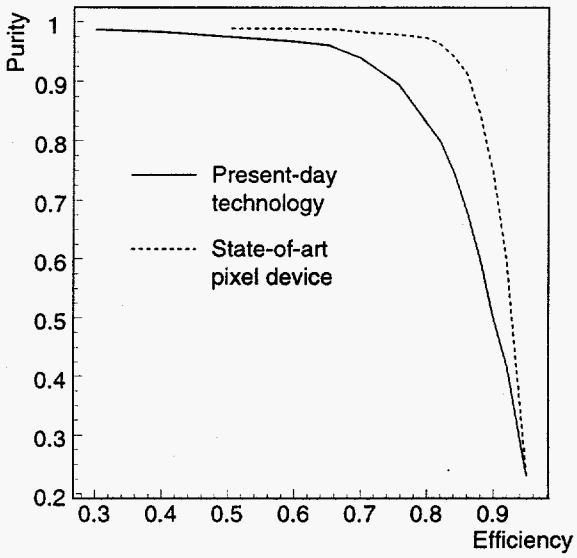

Figure 0.1: Efficiency versus purity relation for b-tagging with the NLC detector.

reactions.

The cross sections of Standard Model processes at an e^+e^- collider are shown as a function of center of mass energy in Fig. 0.2 [3]. From left to right across this plot, the familiar e^+e^- annihilation processes fall with energy according to the point cross section for $e^+e^- \to \mu^+\mu^-$ in QED,

$$1\ \mathrm{R} = \frac{4\pi\alpha^2}{3s} = \frac{87\ \mathrm{fb}}{s\ (\mathrm{TeV}^2)}\ . \tag{0.2}$$

At the same time, new processes involving pair production and multiple production of weak interaction vector bosons become important.

Another view of the standard model backgrounds is given in Fig. 0.3, where the cross sections for the dominant e^+e^- annihilation processes are shown as a function of the degree of longitudinal polarization. The curves were calculated using ISAJET 7.13 [2]. The peripheral two photon, t-channel Bhabha scattering and $e^+e^- \to Z^\circ\gamma$ processes are not shown; the cross sections for these reactions are relatively independent of polarization. The reactions $e^+e^- \to e^+\nu W^-, e^-\overline{\nu}W^+, e^+e^-Z^0$ are also not shown. The first of these is present only for left-handed e^-; the other two depend only weakly on e^- beam polarization. The most troublesome source of background in many of the physics analyses is the reaction $e^+e^- \to W^+W^-$, whose special role we have already pointed out. It is noteworthy that the cross section for this process can be reduced substantially by adjusting the electron beam polarization.

Cuts on other quantities, such as the acoplanarity and production angle will also be useful for removing standard model background. The distributions in these variables for standard model annihilation processes are shown in Figs. 0.4 and 0.5.

In general, the two photon and $e^+e^- \to Z^0\gamma$ processes are not important as backgrounds to annihilation processes because they may be removed easily from the data sample by low

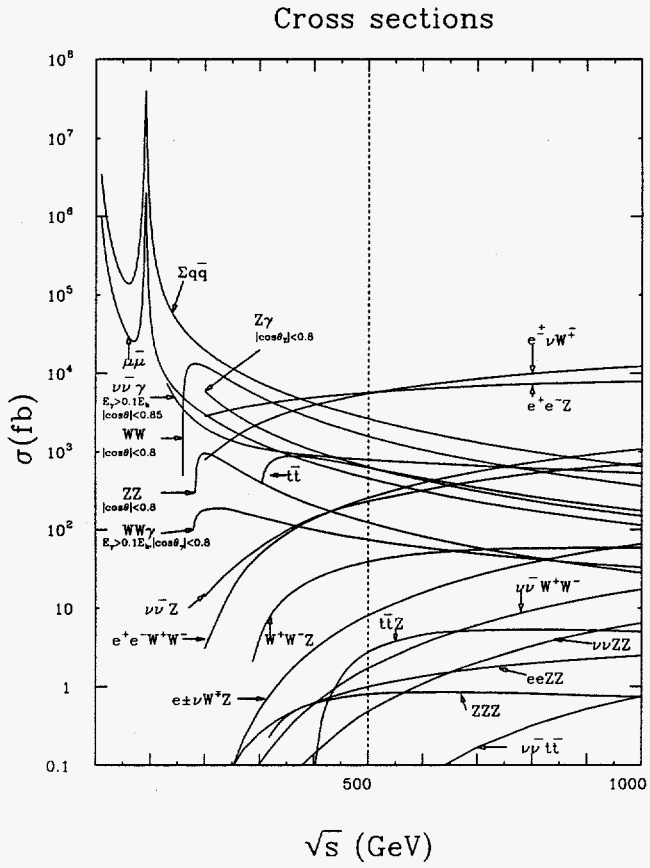

Figure 0.2: Cross sections for Standard Model physics processes in e^+e^- annihilation, as a function of center of mass energy, from [3].

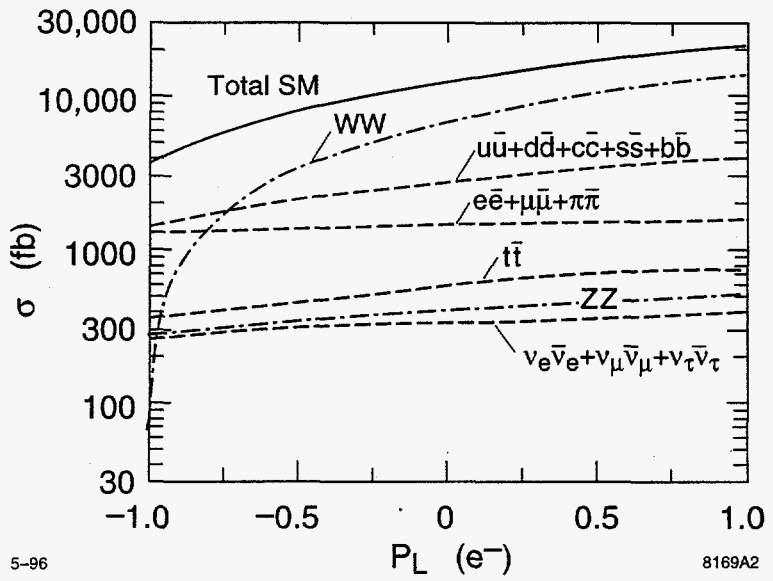

Figure 0.3: Cross sections for Standard Model physics processes in e^+e^- annihilation at 500 GeV, as a function of the electron longitudinal polarization.

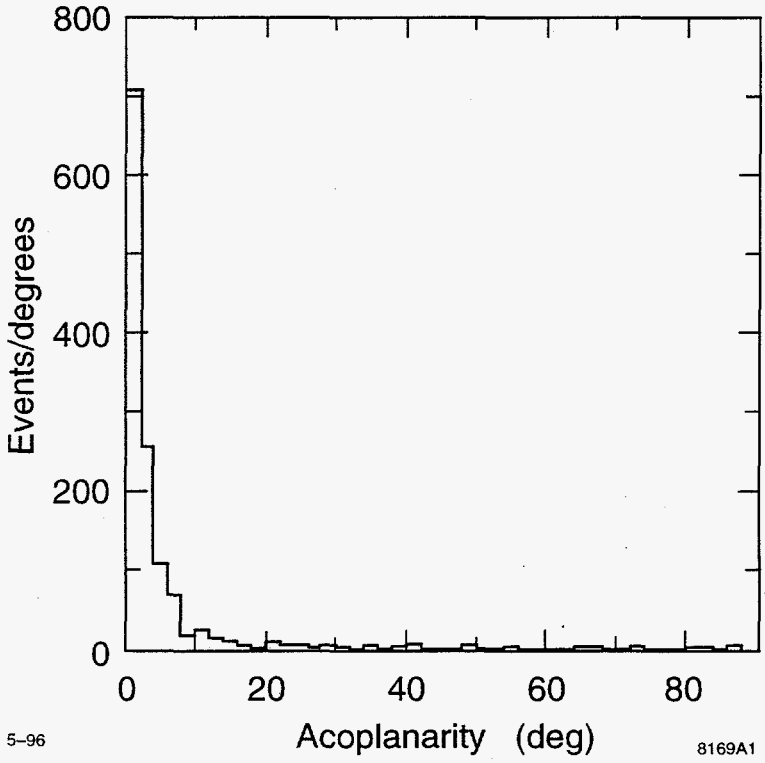

Figure 0.4: Expectation for the acoplanarity distribution in $e^+e^- \to W^+W^-$ events in which both W bosons decay to hadrons.

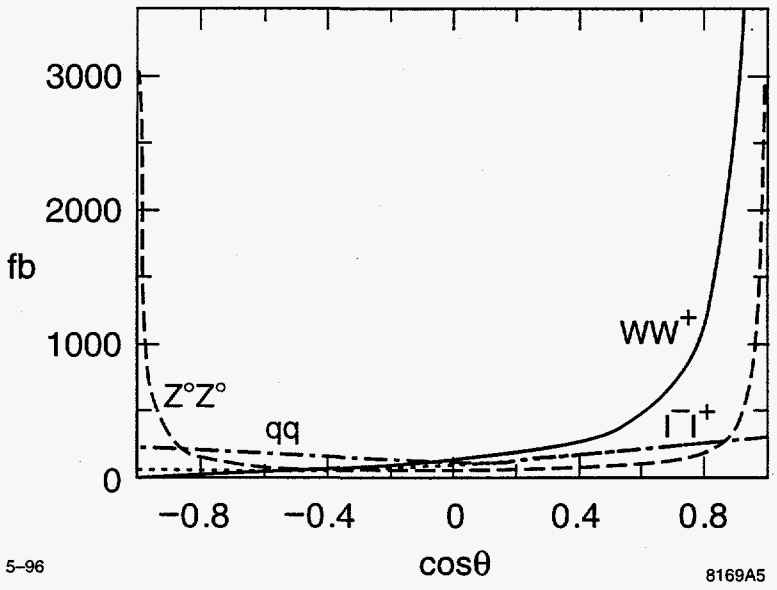

Figure 0.5: Expectation for the $\cos\theta$ distribution due to standard model processes.

transverse momentum and multiplicity cuts [4]. The cross section for Bhabha scattering is very large in the forward direction but drops to a few units of R at large angles.

0.3 Top Quark Physics

The stage for the future of top physics has been set by the recent discovery [8] of top at Fermilab. The very large top mass, $m_t \approx 175 \pm 9$ GeV/c^2, forces one to consider the possibility that the top quark plays a special role in particle physics. At the very least, the properties of the top quark could reveal important information about the physics of electroweak symmetry breaking. In this context, the determination of the complete set of top quark properties should be an important goal. A high-energy future linear e^+e^- collider provides a very impressive tool to carry out a detailed top quark physics program.

The $t\bar{t}$ threshold region has a rich phenomenology which derives from its mix of toponium and continuum structure. Only in e^-e^+ collisions can this threshold structure be properly resolved, making possible definitive measurements of the top mass and width and tests of the QCD potential at very short range. Above threshold, the NLC makes it possible to measure the complete set of top couplings to gauge bosons, both for neutral current (γ and Z^0) and charged current interactions. The high electron-beam polarization available at NLC plays an important role in such studies, simplifying the search for anomalous top couplings and CP violating effects. A complete understanding of electroweak symmetry breaking will require the measurement of the Higgs boson couplings to fermions; of these, the coupling to top is the most accessible. At the NLC, this quantity can be measured by direct $t\bar{t}H$ production above threshold and also, if the Higgs boson is light, by the effect of Higgs boson exchange on the threshold properties. Finally, the NLC provides a the relatively clean final state and precise vertex detection which make it straightforward to study the decays of the top. All standard decay modes can be reconstructed with reasonable efficiency, and exotic decay modes, in those examples studied to date, can be readily identified.

The physics program for the top quark also imposes important constraints on the NLC design. The energy must be adjustible, to run both at the $t\bar{t}$ threshold and at a point in the continuum about 100 GeV above threshold. The study of the threshold region requires that the center-of-mass energy spread be much smaller than the top quark width, and that tails in the energy distribution be understood. Experimenters must be able to determine both the absolute energy and the differential luminosity spectrum.

0.3.1 Top Production, Decay, and Measurement

The large mass of the top quark causes it to have a very large decay width, and this exerts a decisive influence on its phenomenology. In the Standard Model, the weak decay of top proceeds very rapidly via $t \to bW$, resulting in a total decay width given by

$$\Gamma_t \approx (0.18)(m_t/m_W)^3 \text{ GeV} . \tag{0.3}$$

For $m_t = 180$ GeV/c^2 this lowest-order prediction is $\Gamma_t = 1.71$ GeV. After first-order QCD and electroweak corrections [9], this becomes 1.57 GeV. Hence, top decay is much more rapid than the characteristic time for hadron formation, for which the scale is $1/\Lambda_{\rm QCD}$. This

implies that the phenomenology of top physics is fundamentally different than that of the lighter quarks. For example, there will be no top-flavored mesons. While we lose the familiar study of the spectroscopy of these states, we gain unique clarity in the ability to reconstruct the properties of the elementary quark itself. This may prove to be a crucial advantage toward uncovering fundamental issues.

The top decay also provides a natural cutoff for gluon emission. Indeed, in $t\bar{t}$ processes, the nonperturbative color strings appear in fragmentation only after the tops decay and form along the separating b and $\bar{b}$ lines. Hard gluons emitted from the top and its product bottom quark can exhibit interference phenomena which are sensitive to the value of Γ_t [10, 11].

In the Standard Model, $|V_{tb}| \approx 1$, so that the decay mode $t \to bW$ completely saturates the decay width. Then the branching ratios are determined by the W decay modes from the $b\bar{b}W^+W^-$ intermediate state. This gives 6-jet, 4-jet + lepton, and 2-lepton final states in the ratio 4:4:1, or, including QCD corrections to the W decay rates, $\mathrm{BR}(t\bar{t} \to b\bar{b}qq'qq') = 0.455$; $\mathrm{BR}(t\bar{t} \to b\bar{b}qq'\ell\nu) = 0.439$; $\mathrm{BR}(t\bar{t} \to \ell\nu\ell\nu) = 0.106$, where $q = u, c$, $q' = d, s$, and $\ell = e, \mu, \tau$.

The parton-like decay of top implies that, unlike other quarks, its spin is transferred to a readily reconstructable final state. Measurement of the $b\bar{b}W^+W^-$ final state therefore provides a powerful means of probing new physics manifested by top with helicity analyses. This is explored in Section 0.3.3. Another implication of the large m_t is the Standard Model prediction that the decay $t \to bW$ produces mostly longitudinally polarized W bosons; the degree of longitudinal polarization is given by $m_t^2/(m_t^2 + 2m_W^2) \approx 72\%$ for $m_t = 180$ GeV/c^2. This reflects the fact that the longitudinally polarized W bosons contain degrees of freedom from the electroweak symmetry breaking sector.

The $t\bar{t}$ cross section due to s-channel e^+e^- annihilation mediated by γ, Z bosons increases abruptly just below threshold (see Fig. 0.6), reaches a maximum at roughly 50 GeV above threshold, then falls roughly proportional to the point cross section, Eq. 0.2, as the energy increases. At $\sqrt{s} = 500$ GeV the lowest-order total cross section for unpolarized beams is 0.54 pb; it is 0.74 (0.34) for a fully left-hand (right-hand) polarized electron beam. Hence, in a design year of integrated luminosity (50 fb^{-1}) at $\sqrt{s} = 500$ GeV we can produce 25,000 $t\bar{t}$ events. The cross sections for t-channel processes, resulting, for example, in final states such as $e^+e^-t\bar{t}$ or $\nu\bar{\nu}t\bar{t}$, increase with energy, but are still relatively small. We will discuss these processes in Section 7.3.

The emphasis of most event selection strategies has been to take advantage of the multi-jet topology of the roughly 90% of $t\bar{t}$ events with 4 or 6 jets in the final state. Therefore, cuts on thrust or number of jets drastically reduces the light fermion pair background. In addition, one can use the multi-jet mass constraints $M(\text{jet-jet}) \approx m_W$ and $M(3\text{-jet}) \approx m_t$. Simulation studies [12] have shown that multi-jet resolutions of 5 GeV/c^2 and 15 GeV/c^2 for the 2-jet and 3-jet masses, respectively, are adequate and readily achievable with LEP/SLC detectors. A detection efficiency of about 70% with a signal to background ratio of 10 was attained by selecting 6-jet final states just above threshold. These numbers are typical also for studies which select the 4-jet+$\ell\nu$ decay mode.

Of the backgrounds considered in this study, that from W-pair production is the most

difficult to eliminate. However, in the limit that the electron beam is fully right-hand polarized, the W^+W^- cross section is dramatically reduced. Thus it is possible to use the beam polarization to experimentally control and measure the background. We note, though, that the signal is also somewhat reduced by running with a right-handed polarized beam. A possible strategy might be to run with a right-handed polarized beam only long enough to make a significant check of the background due to W pairs. Another important technique is that of precision vertex detection. The present experience with SLC/SLD can be used as a rather good model of what is possible at NLC. The small and stable interaction point, along with the small beam sizes and bunch timing, make the NLC ideal for pushing the techniques of vertex detection. This has important implications for top physics. Rather loose b-tagging, applied in conjunction with the standard topological and mass cuts mentioned above, should lead to substantially improved top event selection efficiencies and purities.

0.3.2 Threshold Physics

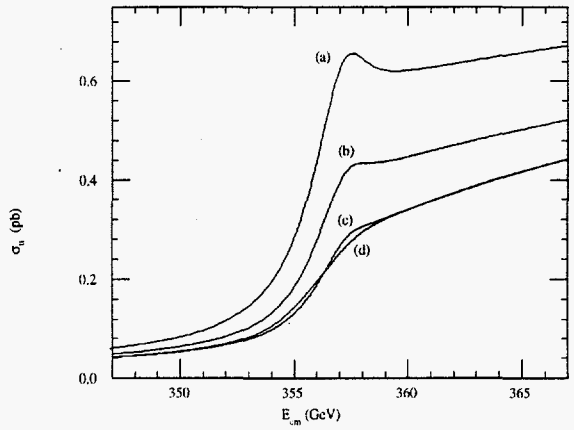

Figure 0.6: Production cross section for top-quark pairs near threshold for $m_t = 180$ GeV/c^2. The ideal theoretical cross section is given by curve (a). In curves (b), (c) and (d), we add, successively, the effects of initial-state radition, beamstrahlung, and beam energy spread.

In Fig. 0.6 we show the cross section for $t\bar{t}$ production as a function of nominal center-of-mass energy for $m_t = 180$ GeV/c^2. In this discussion, m_t is the pole mass in QCD perturbation theory. The theoretical cross section, indicated as curve (a), is based on the results of Strassler and Peskin [13], using the $q\bar{q}$ potential of QCD with $\alpha_s(M_Z^2) = 0.12$ and Standard Model couplings to γ and Z. To this curve, the energy-smearing mechanisms of initial-state radiation, beamstrahlung, and beam energy spread, have been successively applied; curve (d) includes all effects. The beam effects were calculated using NLC design parameters.

The threshold enhancement given by the predicted cross section curve of Fig. 0.6a reflects

the Coulomb-like attraction of the produced $t\bar{t}$ state due to the short-distance QCD potential

$$V(r) \sim -C_F \frac{\alpha_s(\mu)}{r} , \tag{0.4}$$

where $C_F = 4/3$ and μ is evaluated at the scale of the Bohr radius of this toponium atom: $\mu \sim \alpha_s m_t$. The level spacings of the QCD potential, approximately given by the Rydberg energy, $\sim \alpha_s^2 m_t$, turn out to be comparable to the widths of the resonance states, given by $\Gamma_\theta \approx 2\Gamma_t$. Thus, the bound state exists, on average, only for approximately one classical revolution before one of the top quarks undergoes a weak decay. The level spacings of the QCD potential approximately given by the Rydberg energy, $\sim \alpha_s^2 m_t$, turn out to be comparable to the widths of the resonance states, given by $\Gamma_\theta \approx 2\Gamma_t$. Therefore the various toponium states become smeared together, as seen in Fig. 0.6, where only the bump at the position of the 1S resonance is distinguishable. The infrared cutoff imposed by the large top width also implies [14] that the physics is independent of the long-distance behavior of the QCD potential. The assumed intermediate-distance potential is also found [12] to have a negligible impact. Hence, the threshold physics measurements depend only on the short-distance potential (Eq. 0.4) of perturbative QCD.

An increase of α_s deepens the QCD potential, thereby increasing the wave function at the origin and producing an enhanced 1S resonance bump. In addition, the binding energy of the state varies roughly as the Rydberg energy $\sim \alpha_s^2 m_t$. So the larger α_s has the combined effect of increasing the cross section as well as shifting the apparent position of the threshold to lower energy. The latter effect is also what is expected for a shift to lower m_t. Therefore, there exists a significant correlation between the measurements of α_s and m_t from a threshold scan.

A number of studies have been carried out to simulate the measurement of the $t\bar{t}$ threshold cross section. Figure 0.7a depicts a threshold scan [12] for which an integrated luminosity of 1 fb^{-1} has been expended at each of 10 energy points across the threshold, plus one point below threshold to measure backgrounds. A value of $m_t = 150$ GeV/c^2 was used. No beam polarization was assumed. A fit of the data points to the theoretical cross section, including all radiative and beam effects discussed above, results in a sensitivity for the measurement of m_t and α_s shown in Fig. 0.7b. The correlation between these two parameters is apparent. Even for the modest luminosity assumed here, the cross section measurement gives quite good sensitivity to these quantities. If no prior knowledge is assumed, the errors for m_t and α_s are 200 MeV/c^2 and 0.005, respectively. Conversely, the single-parameter sensitivity for m_t approaches 100 MeV/c^2 if α_s is known to much better than 2% accuracy. We will describe a method for the precision measurement of α_s in Section 10.1. The theoretical systematic error due to uncertainties in the $t\bar{t}$ threshold cross section is of order 200 MeV.

For a quarkonium state, we expect the cross section at the 1S peak to vary with the total width roughly as $\sigma_{1S} \sim |V_{tb}|/\Gamma_t$, and therefore is very sensitive to the width, as indicated in Fig. 0.8 for rather wide variations in Γ_t relative to the Standard Model expectation. (It is noted that the calculations of Figs. 0.6 and 0.8 use the uncorrected top width, so that the resonance structure will be slighty more pronounced than what is shown.) After applying a

correction for initial-state radiation and the beam-related energy spread, the width is affected as shown in Fig. 0.8. This implies that a scan strategy optimized for measuring Γ_t would spend a relatively large fraction of running time below the 1S peak. The threshold physics, combining the cross section information with the momentum and asymmetry results, as discussed below, represents what is most likely the best opportunity to measure Γ_t.

In addition to the QCD potential, the t-$\bar{t}$ pair is also subject to the Yukawa potential associated with Higgs exchange:

$$V_Y = -\frac{\lambda^2}{4\pi}\,\frac{e^{-m_H r}}{r}\,, \tag{0.5}$$

where m_H is the Higgs mass and λ is the $t\bar{t}$-Higgs Yukawa coupling, $\lambda = m_t/v = [\sqrt{2}G_F]^{1/2}\, m_t$. Because of the extremely short range of the Yukawa potential, its effect is primarily to alter the wave function at the origin, and hence to shift the level of the cross section. This exciting possibility is discussed further in Section 0.3.4. The physics of the threshold cross section is, in summary, expected to depend on the following set of parameters:

$$\sigma = \sigma(m_t, \alpha_s, \Gamma_t, m_H, \lambda)\ . \tag{0.6}$$

As we have discussed, the lifetime of the toponium resonance is determined by the first top quark to undergo weak decay, rather than by the annihilation process. This has the interesting implication that the kinetic energy (or momentum) of the top quark as reconstructed from its decay products reflects the potential energy of the top in the QCD potential. Hence, a measurement of the momentum distribution will be sensitive to α_s and Γ_t. The theory [15] and phenomenology [12, 16] of this physics has been extensively studied. A convenient observable which has been used to characterize the distribution is the position of the peak in the reconstructed top quark momentum distribution. The position of this peak at a given center-of-mass energy is indeed found to be sensitive to Γ_t and the other parameters in Eq. 0.6.

Yet another, quite different observable has been studied [17, 12] to help further pin down the physics parameters at threshold. Top is produced symmetrically when produced in the 1S state. The vector coupling of $t\bar{t}$ to the γ and Z can create S- and D-wave resonance states. On the other hand, the axial-vector coupling of the top quark to the Z gives rise to P-wave resonance states. Hence, there is naturally interference between S- and P-waves which gives rise to a forward-backward asymmetry (A_{FB}) proportional to $\beta\cos\theta$. Because of the large width of the resonance states, due to the large Γ_t, these states do overlap to a significant extent, and a sizeable A_{FB} develops. The value of A_{FB} varies from about 5% to 12% across the threshold, with the minimum value near the 1S resonance. Since the top width controls the amount of S-P overlap, we expect the forward-backward asymmetry to be a sensitive method for measuring Γ_t.

In summary, a data set of 50 fb^{-1} at threshold would provide sensitivity to m_t and α_s at the level of 120 MeV/c^2 and 0.0025, respectively. Similarly, the sensitivity to the total top decay width is 5–10%. Accelerator and detector designs have become sufficiently stable

to make possible calculations which incorporate the systematics associated with luminosity spectra and backgrounds. This would allow better determination of the limiting systematic errors at threshold, which are presently estimated to be at or below the sensitivities above. The measurement of the luminosity spectrum is discussed in more detail in Section 13.

0.3.3 Top Couplings

At the NLC, $e^+e^- \to t\bar{t}$ above threshold will provide a unique opportunity to measure simultaneously all of the top couplings. Due to its rapid weak decay, the top spin is transferred directly to the final state with negligible hadronization uncertainties, therefore allowing the helicity-dependent information contained in the Lagrangian to be propagated to the final state. This final state, expected to be dominated by $bW^+\bar{b}W^-$, can be fully reconstructed with good efficiency and purity, so that a complete helicity analysis can be performed.

The top neutral-current coupling can be generalized to the following expression for the $Zt\bar{t}$ or $\gamma t\bar{t}$ vertex factor:

$$\mathcal{M}^{\mu(\gamma,Z)} = e\gamma^\mu \left[Q_V^{\gamma,Z} F_{1V}^{\gamma,Z} + Q_A^{\gamma,Z} F_{1A}^{\gamma,Z} \gamma^5\right] + \frac{ie}{2m_t}\sigma^{\mu\nu}k_\nu \left[Q_V^{\gamma,Z} F_{2V}^{\gamma,Z} + Q_A^{\gamma,Z} F_{2A}^{\gamma,Z} \gamma^5\right] . \quad (0.7)$$

This expression reduces to the familiar Standard Model tree level expression when we set the form factors to $F_{1V}^{\gamma} = F_{1V}^{Z} = F_{1A}^{Z} = 1$, with all others zero. The quantities $Q_{A,V}^{\gamma,Z}$ are the usual SM coupling constants: $Q_V^\gamma = Q_A^\gamma = \frac{2}{3}$, $Q_V^Z = (1 - \frac{8}{3}\sin^2\theta_W)/(4\sin\theta_W\cos\theta_W)$, and $Q_A^Z = -1/(4\sin\theta_W\cos\theta_W)$. The non-standard couplings $F_{2V}^{\gamma,Z}$ and $F_{2A}^{\gamma,Z}$ correspond to the electroweak magnetic and electric dipole moments, respectively. While these couplings are zero at tree level in the Standard Model, the analog of the magnetic dipole coupling is expected to attain a value of order α_s/π due to corrections beyond leading order. On the other hand, the electric dipole term violates CP and is expected to be zero in the Standard Model through two loops [18]. Such a non-standard coupling necessarily involves a top spin flip, hence is proportional to m_t.

The form factors can be measured through their distinct dependences on the helicities of the e^-, e^+, t, and $\bar{t}$, which can be accessed experimentally through the beam polarization and the angular distributions in the final state. The production and decay angles can be defined as shown in Fig. 0.9. The angle χ_W is defined in the W rest frame. The analogous statement holds for the definition of χ_t. Experimentally, all such angles, including the angles corresponding to χ_t and χ_W for the $\bar{t}$ hemisphere, are accessible. Given the large number of constraints available in these events, full event reconstruction is entirely feasible. To reconstruct θ one must also take into account photon and gluon radiation. Photon radiation from the initial state is an important effect, which, however, represents a purely longitudinal boost which can be handled within the framework of final-state mass constraints. Gluon radiation can be more subtle. Jets remaining after reconstruction of t and $\bar{t}$ can be due to gluon radiation from t or b, and the correct assignment must be decided based on the kinematic constraints and the expectations of QCD.

The distributions of the production angle θ for the SM in terms of the various helicity states are given in Fig. 0.10 for left and right-hand polarized electron beam. We see, for example, that for a left-hand polarized electron beam, top quarks produced at forward angles are predominantly left handed, while forward-produced top quarks are predominantly right handed when the electron beam is right-hand polarized. These helicity amplitudes combine to produce the following general form for the angular distribution [19]:

$$\frac{d\sigma}{d\cos\theta} = \frac{\beta_t}{32\pi s}\left[c_0 \sin^2\theta + c_+(1+\cos\theta)^2 + c_-(1-\cos\theta)^2\right] , \tag{0.8}$$

where c_0 and $c_\pm$ are functions of the form factors of Eq. 0.7, including any non-standard couplings. The helicity structure of the event is highly constrained by the measurements of beam polarization and production angle.

For the measurement of the decay form factors, there are two alternative methods that might provide higher statistics. The first is to measure the top quark decay distributions using polarized beams at the $t\bar{t}$ threshold, making use of the fact that the spin of the nonrelativistic top quarks follows the spin of the incident electron and positron [20]. The second is to analyze the polarization of top quarks above threshold using the beam axis boosted to the top frame; this gives a very high polarization for the decay analysis [21].

For the top charged-current coupling we can write the Wtb vertex factor as

$$\mathcal{M}^{\mu,W} = \frac{g}{\sqrt{2}}\gamma^\mu \left[P_L F_{1L}^W + P_R F_{1R}^W\right] + \frac{ig}{2\sqrt{2}\,m_t}\sigma^{\mu\nu}k_\nu \left[P_L F_{2L}^W + P_R F_{2R}^W\right], \tag{0.9}$$

where the quantities $P_{L,R}$ are the left-right projectors. In the Standard Model, we have $F_{1L}^W = 1$ and all others zero. The form factor F_{1R}^W represents a right-handed, or $V+A$, charged current component. As mentioned earlier, the case where the W is longitudinally polarized is particularly relevant for heavy top, and the χ_t and χ_W distributions are sensitive to this behavior.

We now outline an analysis [22] to measure or set limits on the various form factors mentioned above. We consider a modest integrated luminosity of 10 fb^{-1}, $m_t = 180$ GeV/c^2, and $\sqrt{s} = 500$ GeV. Electron beam polarization is assumed to be $\pm 80\%$. The decays are assumed to be $t \to bW$. In general, one needs to distinguish t from $\bar{t}$. The most straightforward method for this is to demand that at least one of the W decays be leptonic, and to use the charge of the lepton as the tag. (One might imagine using other techniques, for example with topological secondary vertex detection one could perhaps distinguish b from $\bar{b}$.) So we assume the following decay chain:

$$t\bar{t} \to b\bar{b}WW \to b\bar{b}q\bar{q}'\ell\nu, \tag{0.10}$$

where $\ell = e, \mu$. The branching fraction for this decay chain is 29%.

Since the top production and decay information is correlated, it is possible to combine all relevant observables to ensure maximum sensitivity to the couplings. In this study, a likelihood function is used to combine the observables. We use the Monte Carlo generator

developed by Schmidt [23], which includes $t\bar{t}(g)$ production to $\mathcal{O}(\alpha_s)$. Most significantly, the Monte Carlo correctly includes the helicity information at all stages. The top decay products, including any jets due to hard gluon radiation, must be correctly assigned with good probability. The correct assignments are rather easily arbitrated using the W and top mass constraints. When the effects of initial-state radiation and beamstrahlung are included, it has been shown [19] that the correct event reconstruction can be performed with an efficiency of about 70%. The overall efficiency of the analysis, including branching fractions, reconstruction efficiency, and acceptance, is about 18%.

After simple, phenomenological detection resolution and acceptance functions are applied, the resulting helicity angles (see Fig. 0.9) are then used to form a likelihood which is the square of the theoretical amplitude for these angles given an assumed set of form factors. Table 0.3 summarizes some of the results of this analysis. The upper and lower limits of the top quark couplings in their departures from the Standard Model values are given at 68% and 90% CL. All couplings, with real and imaginary parts, can be determined in this way. The right-handed charged-current coupling is shown both for unpolarized and 80% left-polarized electron beam, whereas the other results assume 80% left-polarized beam only. We see that even with a modest integrated luminosity of 10 fb^{-1} at $\sqrt{s} = 500$ GeV, the sensitivity to the form factors is quite good, at the level of 5–10% relative to Standard Model couplings. In terms of absolute units, the 90% CL limit of F_{2A}^Z at 0.15, for example, corresponds to a t-Z electric dipole moment of 8×10^{-18} e-cm.

Table 0.3: Results from the global top quark form factor analysis described in the text, for a data sample of 10 fb^{-1} and $\sqrt{s} = 500$ GeV.

Form Factor	SM Value (Lowest Order)	Limit 68% CL	Limit 90% CL
$F_{1R}^W(P=0)$	0	± 0.13	± 0.18
$F_{1R}^W(P=80\%)$	0	± 0.06	± 0.10
F_{1A}^Z	1	1 ± 0.08	1 ± 0.13
F_{1V}^Z	1	1 ± 0.10	1 ± 0.16
F_{2A}^γ	0	± 0.05	± 0.08
F_{2V}^γ	0	± 0.07	$^{+0.13}_{-0.11}$
F_{2A}^Z	0	± 0.09	± 0.15
F_{2V}^Z	0	± 0.07	± 0.10
$\Im(F_{2A}^Z)$	0	± 0.06	± 0.09

0.3.4 The Higgs-Top Yukawa Coupling

The coupling strength of the Higgs boson to a fermion is proportional to the fermion's mass. The Higgs-top coupling is consequently large and may be unique among the Higgs-fermion couplings in that it is accessible to direct measurement. Such measurements have been contemplated at LHC [24], but they require efficient vertex tagging in high-luminosity running. The environment at NLC is much cleaner, but the luminosity requirements are comparable. With the availability of large data sets (> 50 fb^{-1}), several approaches are tractable at NLC: (1) for light to moderate mass Higgs bosons, the $t\bar{t}$ production cross-section near threshold is sensitive to the Higgs contribution to the $t\bar{t}$ potential; (2) for relatively light Higgs, the yield of $t\bar{t}H$ events measures the Higgs-top coupling; and (3) for Higgs masses exceeding the $t\bar{t}$ threshold, the Higgs boson resonance can appear in $t\bar{t}Z$ events and exhibit the Higgs-top coupling.

Threshold measurements have been discussed above for their intrinsic interest and sensitivity to basic top parameters. Here we note that the presence of an additional attractive, short range force arising from Higgs exchange increases the modulus of the toponium wavefunction at the origin, and thereby enhances the cross-section. Fig. 0.11 shows the distinctive energy dependence of the Higgs enhancement factor, which peaks at the 1S state [25]. Fujii *et al.*[12] have simulated a threshold scan of 10 points, spaced at 1 GeV intervals, to determine the sensitivity to the Higgs-top coupling strength. Their results imply that a 10% measurement is possible with 100 fb^{-1} evenly distributed over the 10 points for $M_H = 100$ GeV. The enhancement is roughly inversely proportional to the Higgs mass, so the scan would yield a 20% (30%) measurement for a 200 (300) GeV Higgs mass. An optimized scan will do better.

The $t\bar{t}H$ events almost always result from "Higgs-strahlung", radiation of the Higgs boson from one of the top quarks, so their yield provides a measure of the square of the Higgs-top coupling. The cross-section for the process is small [26], in the $\mathcal{O}(1)$ fb range for a 500 GeV NLC and $M_H < 100$ GeV. Detection of the events is challenging; they typically contain 8 jets, including 4 b jets. The process $e^+e^- \to t\bar{t}Z$ occurs at comparable rate, and along with $e^+e^- \to t\bar{t}jj$ constitutes the important background. Preliminary studies [12, 27] show that a 100 fb^{-1} sample at 500 GeV will give a $\leq 15\%$ measurement of the Higgs-top coupling for $M_H \leq 100$ GeV. At $\sqrt{s} = 1000$ GeV, the sensitivity extends to over 200 GeV for a measurement of similar accuracy.

The cross-section for $e^+e^- \to t\bar{t}Z$ is about 5 fb between 500 and 1000 GeV center-of-mass energies. When the Higgs mass is above the $t\bar{t}$ threshold, this cross section is enhanced by the process $e^+e^- \to Z^0H^0$, with Higgs decay to $t\bar{t}$. Fujii *et al.* [28] have studied the process for $m_t = 130$ GeV, and concluded that, with an integrated luminosity of 60 fb^{-1} at $\sqrt{s} = 600$ GeV, one could measure the top-Higgs coupling within 10% for a 300 GeV Higgs. For Higgs masses above $2m_t$, the cross-section is lower, and the increased width of the Higgs will make isolating a signal in the $t\bar{t}$ invariant mass distribution more difficult. Even so, one could measure the Higgs-top coupling for a 400 GeV Higgs produced at $\sqrt{s} = 1000$ GeV within about 35% with a data sample of 100 fb^{-1}.

The Higgs-strahlung process is also sensitive to deviations from the Standard Model involving extended Higgs sectors. The $t\bar{t}H$ final state can result from Higgs emission from the t (or $\bar{t}$), or from the intermediate Z. Interference between these sub-processes can give rise to large CP violating effects in extended Higgs models. This was studied in Ref. [29] for a range of two-Higgs doublet models, and it was found that for roughly 100 fb^{-1} of data at $\sqrt{s} = 800$ GeV it would be possible to observe a significant CP asymmetry in a number of final-state observables.

The Higgs-top coupling can be determined in the case that the Higgs is very heavy ($M_H > 400$ GeV/c^2) by measuring the rate of the process $e^+e^- \to \nu\bar{\nu}t\bar{t}$ At $\sqrt{s} = 1500$ GeV, the cross section for this process is about 2 fb in the absence of a Higgs, but will be enhanced by more than a factor of two for Higgs masses in the range 400–1000 GeV/c^2. Preliminary studies by Fujii [28] show that care is required to eliminate radiative $t\bar{t}$, $e^+e^-t\bar{t}$, and $t\bar{t}Z$ backgrounds, but suggest that the Higgs-top coupling can be measurable up to $m_H = 1$ TeV/c^2. The case of a very heavy Higgs boson is discussed in more detail in Section 7.3.

0.3.5 Top Physics Reach of NLC and Hadron Colliders

Table 0.4 summarizes the top physics reach of the NLC and several hadron colliders. The Tevatron Upgrade (TeV*) will establish the baseline for top quark physics in the LHC/NLC era, and will address many subjects of interest in top physics. Its reach has been studied in a report by Amidei *et al.* [30]. The Atlas TDR [24] provides some information on the top physics reach at LHC; this subject will certainly be developed further in the future. The table at best represents what has been studied to date. If a particular measurement at a particular machine has not yet been analyzed, the corresponding entry has been left blank. An "X" marks measurements that cannot be made at a particular machine, by virtue of excessive backgrounds, insufficient signal, or unavailable production mechanisms.

The table demonstrates how crucial a role the NLC plays in obtaining a complete picture of top quark physics. NLC will provide the definitive top mass measurement. It will provide the only direct measure of the top width; at hadron colliders, the total width can be inferred only from a V_{tb} measurement using the assumption that the top has no unobserved exotic decays. The NLC will measure the axial-vector and vector electroweak couplings, some of the charged-current couplings (expressed here as CKM elements), the top-Higgs coupling, and the flavor specific strong coupling. Hadron colliders will also measure the charged current couplings (although V_{td} is probably impossible at both hadron and e^+e^- colliders), and the strong and electromagnetic couplings, but not the couplings to the Z. The LHC may probe the top-Higgs coupling by isolating $t\bar{t}H$ events, but only with difficulty. The NLC can measure the top decay form factors, checking for longitudinal W production and searching for right-handed W's, as can the hadron colliders. Only the NLC can measure the electroweak magnetic and electric dipole moments, because they depend on the neutral current production mechanism. We should note that LHC can be sensitive to top-associated CP violation through more complicated effective interactions [31, 32]. Rare decays with

Table 0.4: Top Physics at Future Facilities

Quantity	TeV* ($1\ \text{fb}^{-1}$)	TeV33 ($10\ \text{fb}^{-1}$)	LHC ($100\ \text{fb}^{-1}$)	NLC($\sqrt{s}=360$) ($50\ \text{fb}^{-1}$)	NLC($\sqrt{s}=500$) ($50\ \text{fb}^{-1}$)
Δm_t	3.5 GeV/c^2	2.0 GeV/c^2	2 GeV/c^2	0.20 GeV/c^2	
$\Delta\Gamma_t$				6–8%	
Δa_t	X	X	X		4%
Δv_t	X	X	X		5%
ΔV_{tb}	14%	6%	X		
ΔV_{ts}	X	X	X?	?	?
ΔV_{td}	X	X	X	X	X
$\Delta\lambda_t$	X	X	?	14%	20%
$\Delta\alpha_s^t$	$(\sigma_{t\bar{t}}=11\%)$	$(\sigma_{t\bar{t}}=4\%)$		0.005	
$\Delta B(t\to bW^0)$	4%	1.3%		1%	
$\Delta B(t\to bW_R)$	2%	0.6%			2%
$\Delta\delta$	X	X	X		$<0.3\,e\hbar/2m_t$
Δd	X	X	X		$<4\times10^{-18}$ e-cm
$B(t\to H^+b)$	$<15\%$	$<6\%$	$<1.4\%$		$<2\%$
$B(t\to\tilde{t}\tilde{\chi}^0)$					$<1\%$
$B(t\to c\gamma)$	$<0.3\%$	$<0.04\%$			
$B(t\to cZ)$	$<1.5\%$	$<0.4\%$	$<5\times10^{-5}$		$<10^{-4}$
$B(t\to ch^0)$				$<1\%$	

distinctive signatures can be sought in either environment, with the advantage to hadron decays by virtue of the large statistical samples anticipated. The more exotic decays, *e.g.* $t\to\tilde{t}\tilde{\chi}^0$, are more sensitively sought in the clean environment of the NLC.

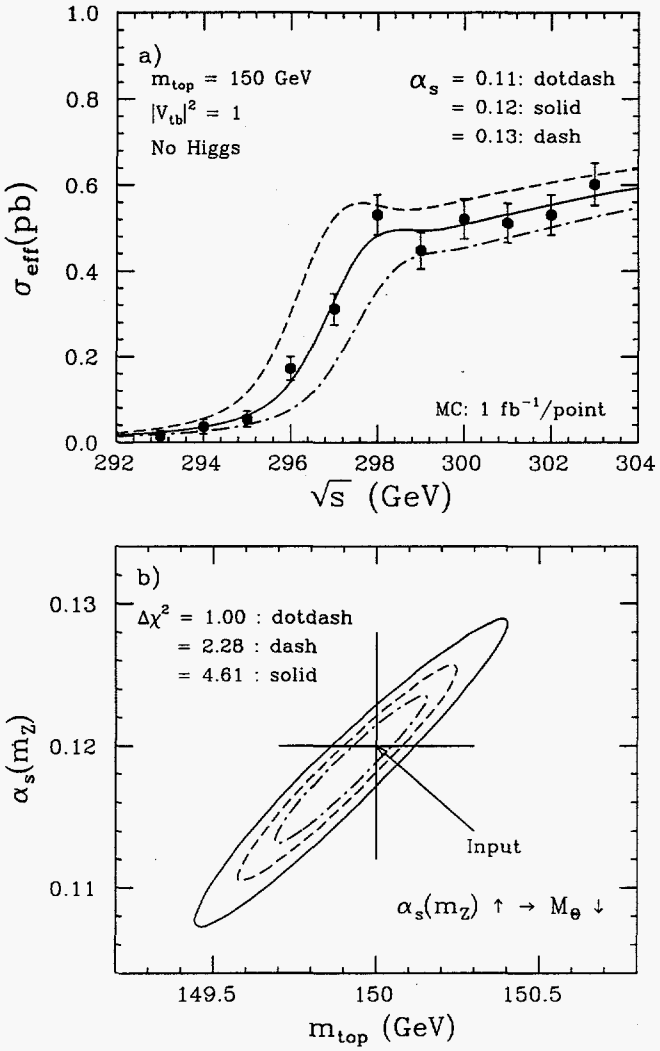

Figure 0.7: (a) Top threshold scan; (b) corresponding error ellipse for m_t and α_s. A value for m_t of 150 GeV/c^2 was assumed.

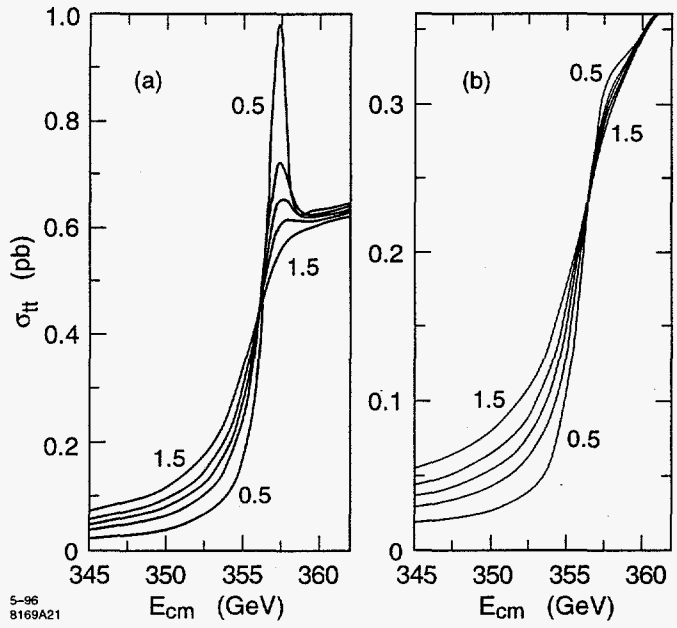

Figure 0.8: Variation of the $t\bar{t}$ threshold cross section with the top width for $m_t = 180$ GeV/c^2. The curves correspond to values of Γ_t/Γ_{SM} of 0.5, 0.8, 1.0, 1.2, and 1.5, presented in the order indicated, for (a) the theoretical cross section, and (b) the cross section after including radiative and beam effects.

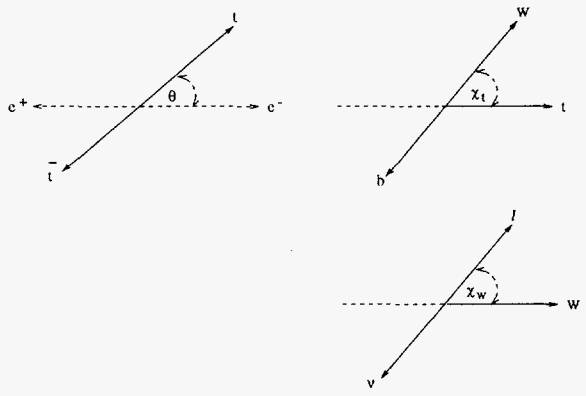

Figure 0.9: Definitions of helicity angles. (a) Production angle θ in $t\bar{t}$ rest frame; (b) χ_t measured in the top rest frame as shown; and (c) χ_W in the W rest frame.

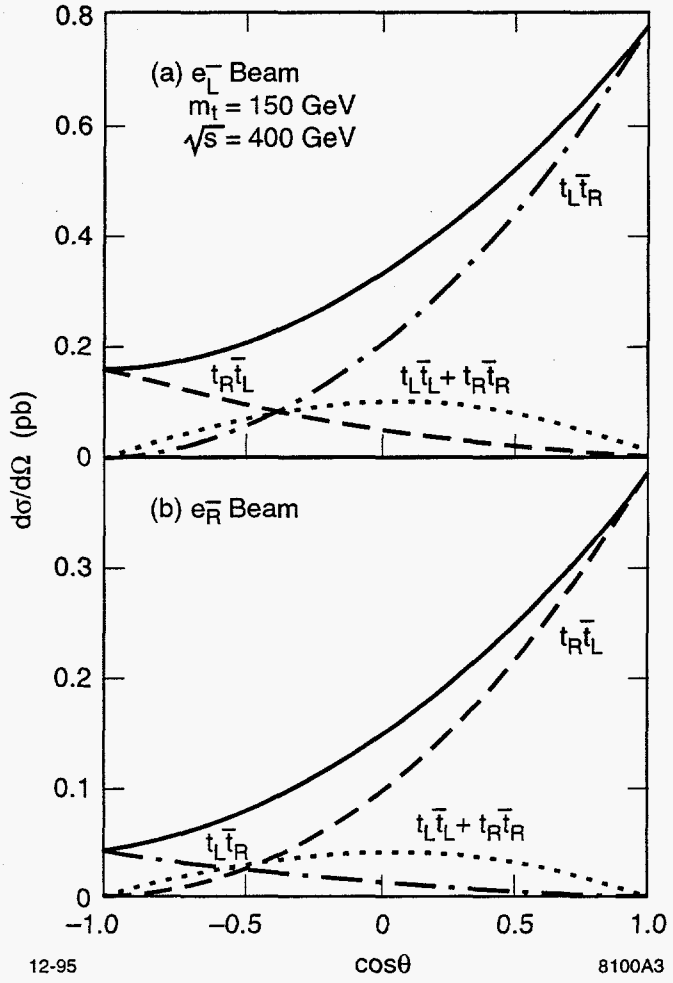

Figure 0.10: Production angle for $t\bar{t}$ for the possible final-state helicity combinations, as indicated, for 100% polarized beams with (a) left-hand polarized electrons, and (b) right-hand polarized electrons. The complete cross sections are the solid curves.

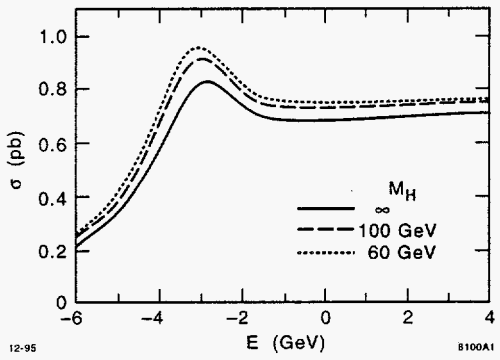

Figure 0.11: Theoretical cross section as a function of Higgs mass for $m_t = 180$ GeV/c^2.

0.4 Higgs Boson Searches and Properties

0.4.1 Introduction

Despite the extraordinary success of the Standard Model (SM) in describing particle physics up to the highest energy available today, the mechanism responsible for electroweak symmetry breaking (EWSB) has yet to be determined. In particular, the Higgs boson [33, 34, 35] predicted in the minimal Standard Model and the theoretically attractive Supersymmetric (SUSY) Grand Unified Theory (GUT) extensions thereof have yet to be observed. If EWSB does indeed derive from non-zero vacuum expectation values for elementary scalar Higgs fields, then one of the primary goals of constructing future colliders must be to *completely* delineate the associated Higgs boson sector. In particular, it will be crucial to discover all of the physical Higgs bosons and determine their masses, widths and couplings. Conversely, if a fundamental Higgs boson does not exist, it is essential to demonstrate this unambiguously.

The EWSB mechanism in the Standard Model is phenomenologically characterized by a single Higgs boson (h_{SM}) in the physical particle spectrum. The mass of the h_{SM} is undetermined by the theory, but its couplings to fermions and vector bosons are completely determined. In SUSY theories, there are two Higgs doublets with vacuum expectation values v_1, v_2. These contribute mass terms for the gauge bosons proportional to $(v_1^2 + v_2^2)$, masses for down-type fermions proportional to v_1, and masses for up-type fermions proportional to v_2. In the Minimal Supersymmetric Standard Model (MSSM) [36, 37] these two doublets give rise to five physical Higgs bosons: h^0, the lighter of the two CP-even states; H^0, the heavier CP-even state; the CP-odd A^0 boson, and a pair of charged bosons $H^{\pm}$. The mass of the minimal SM Higgs boson is unspecified, but in the MSSM, there are tree-level relations which determine the spectrum of masses in terms of one of the boson masses (e.g., the mass of the A^0) and the ratio of the vacuum expectation values, v_2/v_1. The CP-even and CP-odd neutral Higgs bosons have nontrivial mixing angles α and β, respectively, which affect their couplings and decays. In particular, $v_2/v_1 = \tan\beta$. Both masses and couplings receive further radiative corrections which are functions of the SUSY Higgs mass parameter, μ, the scale of mass at which SUSY is broken, M_{SUSY}, the mass of the top quark, and the A_i parameters of the soft supersymmetry-breaking interaction. Finally in non-supersymmetric models with two Higgs doublets (2HDM), the Higgs bosons may have mixed CP character due to CP violation effects.

Supersymmetry has exciting implications for the discovery potential for the Higgs bosons that it predicts. In the MSSM, considering renormalization group improved radiative corrections and assuming $m_t = 180$ GeV with the stop mass less than 1 TeV, the lightest Higgs boson must have mass $M_{h^0} \lesssim 130$ GeV. An even more sweeping statement can be made [38] that $M_{h^0} \lesssim 150$ GeV for *any* SUSY theory with a grand unification at high energy which includes the elementary Higgs fields.

0.4.2 Present and Future Limits

The best direct limits on the SM Higgs boson come from searches at LEP, with the present limit [39] being $M_{h_{SM}} > 65.2$ GeV at 95% confidence level (C.L.). These limits can also be interpreted in the framework of the MSSM to exclude the lightest SUSY Higgs with mass less than approximately 45 GeV. Electroweak radiative corrections including the top quark and the Higgs boson affect precision electroweak measurements, and global fits [40] using data from LEP, SLC, the Tevatron, and neutrino scattering give the relatively weak limits implying that $M_{h_{SM}} < 300$ GeV (95% C.L.).

LEP2

The limit on the Higgs boson mass will be improved in the near future with the operation of the LEP2 energy upgrade of the LEP collider. With an integrated luminosity of 150 pb^{-1} in each of the four LEP detectors, expected from one year of design luminosity, the 5σ discovery reach can be increased [41] to about 95 GeV with running at center-of-mass energies of 192 GeV scheduled for 1997. At the same energy and luminosity, a cross section in excess of 65 (30) fb can be discovered (excluded) in the $e^+e^- \to hA$ channel when supersymmetric decays are closed. The resultant exclusion region in the MSSM parameter space can be found in Fig. 0.13. The possibility of running at 205 GeV, which would result in an extension of limits close to the MSSM bound, is currently being investigated.

Upgraded Tevatron

The associated production of a Higgs boson and a W or Z boson, with the Higgs decaying to $b\bar{b}$ and the W or Z decaying leptonically, is a possible way to detect the Higgs in the mass range 60–130 GeV, at a high luminosity Tevatron collider [30]. The Higgs decays give rise to 2 jets, thus one will use b tagging to reduce the large $W + 2$ jet backgrounds. It appears that the present b tagging capability at CDF is more than adequate to reduce this background (at moderate Run II luminosities, e.g., $10^{32}\times$ cm^{-2} s^{-1}, 1 TeV $\times$ 1 TeV) if this capability is extended to larger rapidities (as is planned in Run II for both CDF and D0). After b tagging, the largest background at Higgs masses below 100 GeV is QCD production of $W + b\bar{b}$ and top backgrounds for masses above 100 GeV. Figure 0.12 shows the dijet mass distribution for the sum of all these backgrounds, plus the $W + H$ signal for 10 fb^{-1}. An observation of the Higgs for masses below 100 GeV is possible after the Main Injector upgrade, and is within reach of the present Run II accelerator after several years of data-taking. For higher mass Higgs bosons, these statistics are too low; that one would need about 25 fb^{-1} to observe the 120 GeV Higgs. This study assumed an approximate 20% improvement in dijet mass resolution obtained from applying a clustering algorithm that reduces the effect of gluon radiation at large angles to the jet. This dijet mass resolution and jet clustering is crucial in seeing the Higgs. It has been argued that the $h \to \tau^+\tau^-$ and $Z \to \nu\bar{\nu}$ channels can be used to improve these results [42].

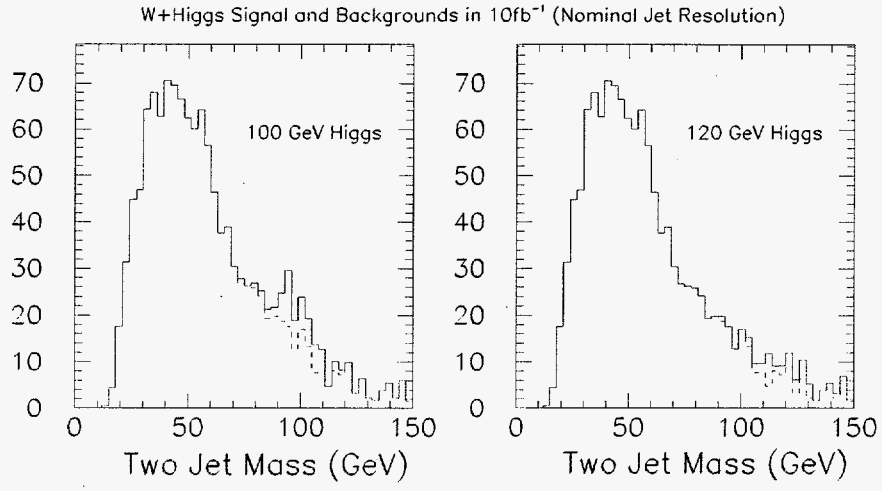

Figure 0.12: The signal plus background mass distributions for the WH process with 10 fb^{-1} of data at 2 TeV. The solid line is signal+background, the dashed line the sum of all backgrounds.

Large Hadron Collider

At the Large Hadron Collider (LHC), detection of the SM h_{SM} is possible through the process $gg \to h_{SM} \to \gamma\gamma$ for $M_{h_{SM}} < 150$ GeV and through $gg \to h_{SM} \to ZZ^{(*)} \to 4\ell$ for $M_{h_{SM}} > 130$ GeV. A heavy h_{SM} is also detectable in the reaction $WW \to h_{SM}$, with the Higgs decaying to ZZ and also, possibly, to WW. The $\gamma\gamma$ channel that is crucial for a light h_{SM} demands an excellent electromagnetic calorimeter, and much attention has been devoted to this in the LHC detector designs. For $M_{h_{SM}} < 120$ GeV, it will also be possible to detect $t\bar{t}h_{SM}$ and (possibly) Wh_{SM} with $h_{SM} \to b\bar{b}$, provided that the high b-tagging efficiency and purity projections are realized. Detection of the h_{SM} in the intermediate mass region when $M_{h_{SM}} < 2M_W$ generally requires accumulating data for at least a year when the LHC is run at full luminosity. This should be contrasted with e^+e^- collisions, where the $e^+e^- \to Zh_{SM}$ mode will allow detection in the same mass region in a matter of a few hours, assuming full instantaneous luminosity.

In the case of the MSSM for large M_{A^0}, the h^0 is similar to the Standard Model Higgs h_{SM}. As for the h_{SM}, the h^0 is straightforward to detect at an e^+e^- collider. On the other hand, the H^0 and A^0 do not resemble the Standard Model Higgs boson, and so one must separately consider their production process. We will show below that the observability of H^0 and A^0 at an e^+e^- collider depends only on the beam energy: for $\sqrt{s} > 2M_{A^0} - 20$ GeV, these particles are found in the reaction $e^+e^- \to Z^* \to H^0A^0$.

The story at the LHC is much more complex. The reactions which can be used to detect the Higgs particles of the MSSM, and their limits of applicability in parameter space, are displayed in Fig. 0.13 [35]. This figure represents the limit of the LHC capability, summing the results of two detectors in a multi-year run at design luminosity. For values of $M_A > 200$

GeV, the LHC can detect the H^0 and A^0 only in certain specific decay channels, shown in the figure, whose availability depends on the value of $\tan\beta$. Since this figure summarizes a great deal of analysis, we must point out at least a few of the assumptions which are used. The channel $A^0, H^0 \to \tau^+\tau^-$ can be used only when the branching ratio to τ is enhanced by a large value of $\tan\beta$. For small $\tan\beta$, modes with $b\bar{b}$ or $t\bar{t}$ in the final states require b tagging capabilities that will be challenging in the detection environment of the LHC. In addition, it should be noted that the process $A^0, H^0 \to t\bar{t}$ has so far been studied only at the level of the comparison of cross sections for signal and background, and that, since the signal is 2–10% of the background, an excellent knowledge of the $gg \to t\bar{t}$ cross section is required. Finally, though the h^0 should be detected for the generic situation illustrated in Fig. 0.13, there are regions of the full parameter space of the MSSM where the h^0 would not be observed [43]. Thus, it is unlikely that the whole MSSM Higgs spectrum would be observed at the LHC, and it is not possible to rule out the MSSM if none of its Higgs bosons are seen at the LHC.

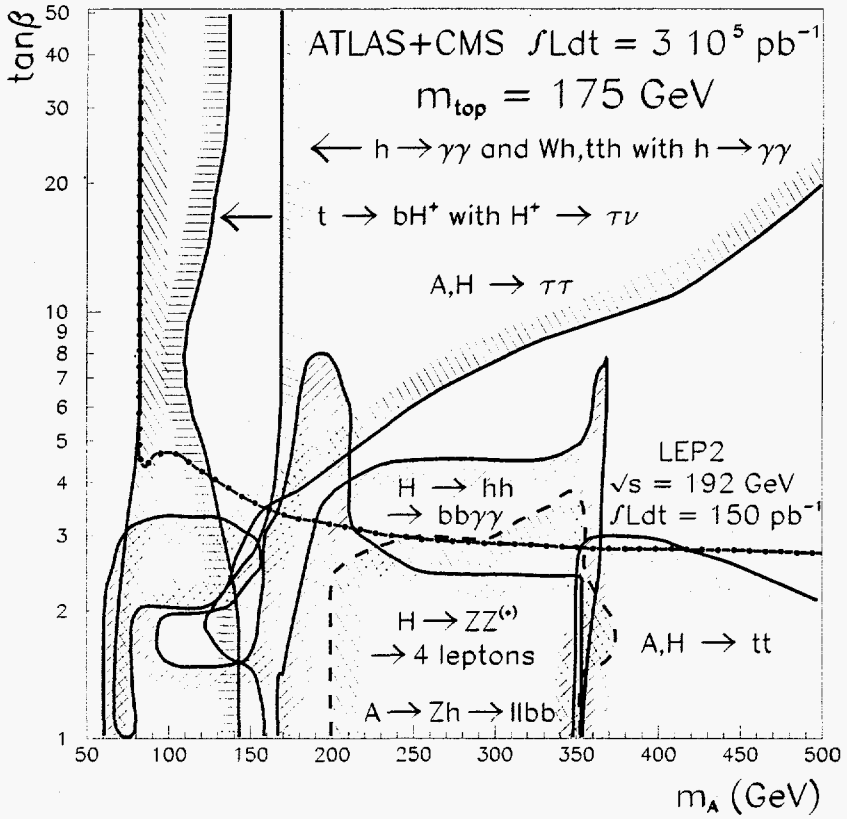

Figure 0.13: Higgs discovery contours (5σ) in the generic parameter space of the MSSM for ATLAS+CMS at the LHC, for a multi-year run at design luminosity, 300 fb^{-1} per detector, from [35]. Renormalization group improved radiative corrections are included for M_{h^0} and M_{H^0}, assuming $m_{\tilde{t}} = 1$ TeV and no squark mixing.

0.4.3 Standard Model Higgs

The main production processes for the SM Higgs in e^+e^- annihilation are $e^+e^- \to ZH$ and the gauge boson fusion processes $e^+e^- \to \nu\bar{\nu}H$ (WW fusion) and $e^+e^- \to e^+e^-H$ (ZZ fusion). The cross sections for these processes are shown in Fig. 0.14. With a typical integrated luminosity of 10 fb^{-1} at $\sqrt{s} = 500$ GeV with $M_H = 150$ GeV, about 1000 signal events would be expected before cuts and branching ratios. Handy "rules of thumb" are that the peak for ZH production occurs at $\sqrt{s} \approx M_Z + \sqrt{2}M_H$ and that the cross-over for equal cross sections from the fusion and bremsstrahlung mechanisms occurs at $\sqrt{s} \approx 0.6M_H + 400$ GeV.

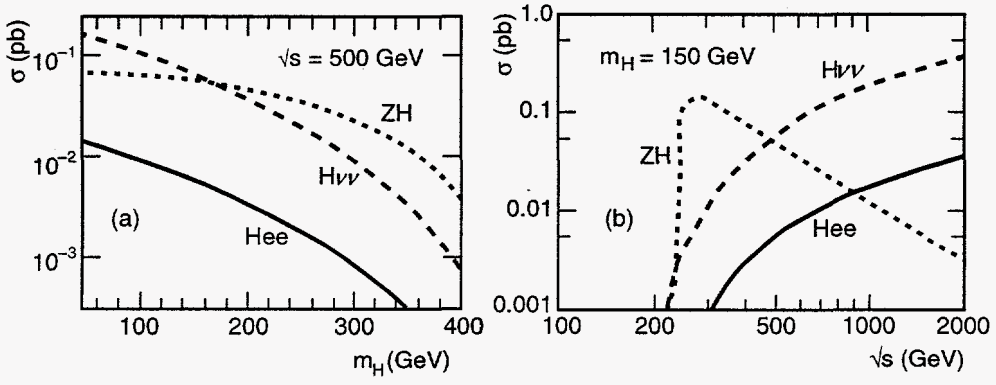

Figure 0.14: Cross section for Standard Model Higgs boson production.

The decay modes of the Standard Model Higgs depend strongly upon its mass. The branching ratios of the Standard Model Higgs are shown in Fig. 0.15. A very interesting region is the intermediate mass Higgs with $M_Z < M_H < 2M_W$, which at a hadron collider is relatively more difficult to detect than a heavy Higgs boson. Almost all of the decays, both those to fermions and those into pairs of gauge bosons are itentifiable in e^+e^- experiments, and it should be possible to measure individual branching ratios. For an intermediate mass Higgs, the dominant decay channel is clearly $H^0 \to b\bar{b}$, with the branching ratio for $H^0 \to W^+W^{-(*)}$ growing with increasing mass (even for $E_{cm} < 2M_W$ where one of the W's must be off shell). This latter channel remains dominant for heavy Higgs bosons, and is joined by ZZ and $t\bar{t}$ modes when kinematically accessible.

Signal Topologies and Backgrounds

Typical signal topologies in the intermediate mass range are shown in Fig. 0.16. The associated production $e^+e^- \to Z^0H^0$, is followed by standard decays of the Z^0 (10% $\ell^+\ell^-$, 20% $\nu\bar{\nu}$, and 70% $q\bar{q}$) and decays of the H^0 mostly into $b\bar{b}$, occasionally into $\tau^+\tau^-$, and more rarely into $c\bar{c}$ and gg. After straightforward cuts, the most serious backgrounds are due to irreducible Standard Model processes, $e^+e^- \to ZZ$, $Z\nu\bar{\nu}$, and $We\nu$.

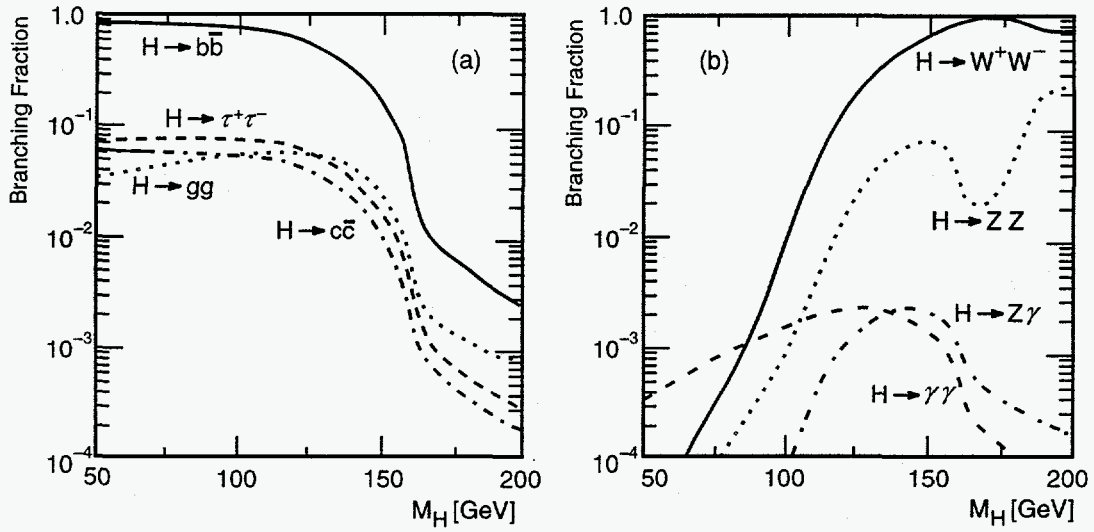

Figure 0.15: Branching fractions of a SM Higgs boson.

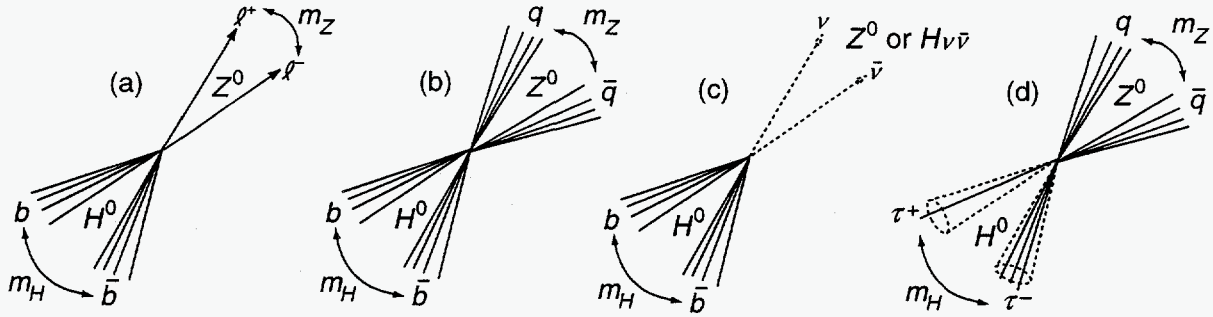

Figure 0.16: Important signal topologies for an intermediate mass SM Higgs boson.

Experimental Studies

The detection of Higgs bosons in e^+e^- collisions at high energy has been studied extensively in simulations [48, 45, 46]. The detector simulations that have been employed usually emulate LEP/SLC-type detectors using smeared four-vectors, while some consider simulations of a more ambitious JLC-type detector [47]. Most studies include the effects of "beamstrahlung", the radiation of photons in the intense electromagnetic fields of the beam-beam collision. Like more standard initial-state radiation, this effect is usually taken into account in kinematic fits by allowing for an unknown missing momentum along the beam axis.

In the topology of Fig. 0.16a, one can first identify two leptons with invariant mass close to the mass of the Z^0, and then investigate the remaining hadronic mass or use kinematic constraints to study the missing or recoil mass in the event:

$$M_{miss} = \sqrt{(\sqrt{s} - E_{\ell+} - E_{\ell-})^2 - (\vec{p}_{\ell+} + \vec{p}_{\ell-})^2}.$$

This quantity has a large peak at the Z^0 mass from the irreducible background process $e^+e^- \to Z^0Z^0$; $Z^0 \to \ell^+\ell^-$; $Z^0 \to q\bar{q}$. If $M_H \approx M_Z$, the signal and the ZZ background are kinematically equivalent, and one would need b-quark tagging to distinguish the signal. Since $Br(Z^0 \to b\bar{b}) \simeq 20\%$, while $Br(H^0 \to b\bar{b}) \simeq 85\%$ at this mass, an analysis in this worst case would require 50 fb^{-1} of data.

The four-jet topology of Fig. 0.16b has been considered in a number of studies, in particular, in a comprehensive study by Janot [48] at $\sqrt{s} = 500$ GeV which assumed an integrated luminosity of 10 fb^{-1}. After selection cuts, for $M_H = 110$ GeV, a small signal is observed above the background, which comes mainly from $e^+e^- \to W^+W^-$, Z^0Z^0, and $qq(\gamma)$. This signal is greatly enhanced, as shown in Fig. 0.17b, by requiring that at least one of the jets forming the Higgs signal peak come from a tagged b quark. The vertex-tagger is assumed to have the conservative performance $\epsilon_{b\bar{b}} = 50\%$, $\epsilon_{c\bar{c}} = 2.5\%$, $\epsilon_{c\bar{s}} = 0.3\%$, and $\epsilon_{q\bar{q}} = 0.1\%$, where the numbers give the efficiency for tagging a particular quark combination. The importance of b tagging is even greater as one moves up in mass.

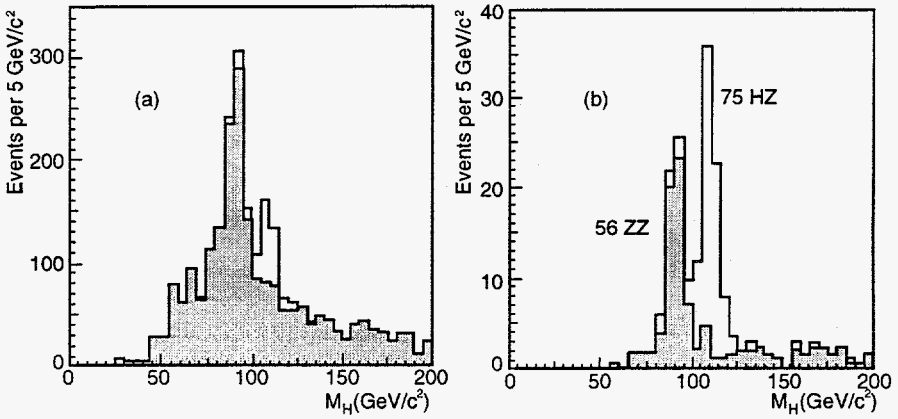

Figure 0.17: Distribution of the invariant mass of the Higgs jet pair in the four-jet topology (a) before and (b) after b-quark tagging, for all known backgrounds (shaded histograms) and for the signal ($M_H = 110$ GeV) (adapted from Ref. 10).

The missing energy topology shown in Fig. 0.16c can arise either from the ZH process, with $(Z^0 \to \nu\overline{\nu})(H^0 \to b\bar{b})$, or from WW fusion. The resultant events will have large missing energy, transverse momentum, and mass, plus the presence of acoplanar jets. This distinctive signature offsets the loss of the Z-mass constraint. The last topology of Fig. 0.16d can be isolated by tagging two τ leptons either from their one- or three-prong decays recoiling against a reconstructed Z^0 decaying into $q\bar{q}$. Using a kinematically-constrained fit the missing neutrinos from the τ decay can be taken into account.

The examples given so far rely primarily on the large branching ratio for $H^0 \to b\bar{b}$. As the H^0 gets heavier, other decay modes begin to become important. For example, for $M_H = 140$ GeV, $Br(H^0 \to W^*W) \simeq 45\%$. The mode $(Z^0 \to q\bar{q})(H^0 \to W^*W)$ has been investigated [49] by demanding a six-jet event with a reconstructed Z^0 hadronic decay, one

jet pair reconstructing to M_W, and the last pair peaking at $m < M_W$, depending on M_H. Similarly, for $M_H = 160$ GeV, the decay $H^0 \to W^+W^-$ dominates, and for production via fusion, $e^+e^- \to H\nu\overline{\nu}$, the result is an acoplanar pair of reconstructed W bosons and a total visible mass peaking at the H mass which is expected to be well above background without the need for b-tagging.

Studies have therefore shown that with a detector similar to the LEP/SLC detectors, with b-quark vertex tagging provided by silicon microvertex detectors using present technology, an intermediate-mass SM Higgs boson cannot escape detection at an e^+e^- linear collider at $\sqrt{s} = 500$ GeV. Figure 0.18 shows an estimate [48] of the minimum luminosity required to discover at the 5σ level a SM Higgs boson of a particular mass. An integrated luminosity of only 5 fb^{-1} would be adequate to cover the entire intermediate mass range, while 20 fb^{-1} would allow a reach in mass up to about $\sqrt{s}/2$.

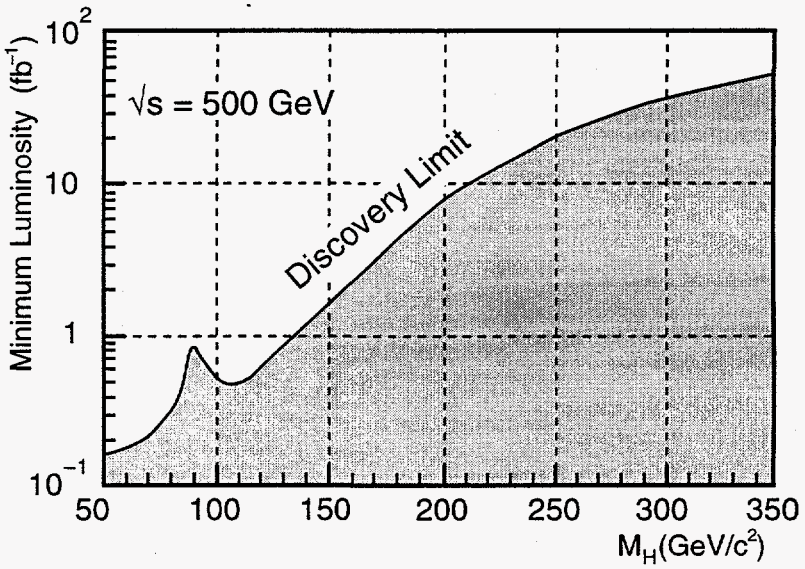

Figure 0.18: Minimum luminosity needed to discover a SM Higgs boson at a center-of-mass energy of 500 GeV.

Higher $\sqrt{s}$ would of course allow one to probe for the existence of much heavier Higgs bosons, mostly through WW fusion and decay into pairs of vector bosons. At center of mass energies of 1–2 TeV, different backgrounds such as $e^+e^-W^+W^-$ and $e^+\nu_e W^- Z^0$ need to be addressed. Even though there exist older studies [4, 50] of searches for heavy Higgs bosons in 1–2 TeV e^+e^- collisions, these investigations need to be updated with more detailed simulations and to keep abreast of theoretical developments [51] regarding backgrounds and the decay of heavy Higgs bosons. For very large Higgs boson masses, this study becomes a part of the general problem of studying WW scattering at high energies; we discuss this problem in some detail in Section 7.2.

0.4.4 Minimal Supersymmetric Standard Model Higgs

In the framework of the MSSM, production of the lightest CP-even state h^0 is similar to that of the SM higgs boson. It is produced by the Zh and WW fusion processes just described, with h^0 replacing h_{SM}. In addition, new modes of production also open up, involving the heavy Higgs bosons H^0 and A^0. The various production processes for h^0 and H^0 in e^+e^- annihilation depend on the mixing angles α and β as indicated in Table 0.5. Notice the sum rule: One process in each line always has a substantial rate. As $m_A \to \infty$ in the MSSM, $\cos(\beta - \alpha) \to 0$, and only the processes in the left-hand column of the table occur. In this limit, the rates of the h^0 production processes are identical to those for the Standard Model Higgs.

Table 0.5: Dependence of the cross section on Higgs boson mixing angles for various Higgs boson production processes in the MSSM.

$\sin^2(\beta-\alpha)$	$\cos^2(\beta-\alpha)$
h^0Z^0	H^0Z^0
$h^0\nu\overline{\nu}$	$H^0\nu\overline{\nu}$
H^0A^0	h^0A^0

The phenomenology of the SUSY Higgs bosons varies in a smooth way as M_A is varied. The contours of Higgs mass over the MSSM parameter space are shown in Fig. 0.19 [52]. If $M_A < 125$ GeV, then A^0 and h^0 are close in mass; if $M_A > 125$ GeV, then $M_A \simeq M_H$ and we begin to approach the large M_A limit. However, if $M_A < 230$ GeV, then all of the MSSM Higgs bosons should still be observable at the NLC with $\sqrt{s} = 500$ GeV. If $M_A > 230$ GeV, it is possible that, at the $\sqrt{s} = 500$ GeV stage of the NLC, only the lightest SUSY Higgs h^0 may be observable *and* it would have production rates virtually indistinguishable from those of a minimal Standard Model Higgs boson. The remaining Higgs states could be discovered at higher $\sqrt{s}$, and there are also precision tests available, to be described later, which could distinguish a Standard Model Higgs from a supersymmetric Higgs. However, since the h^0 will result in decay topologies similar to that of the SM Higgs, if this lightest h^0 is not observed, then the MSSM is categorically ruled out. If the h^0 is not seen below 150 GeV, the more general supersymmetry models incorporating grand unification are also excluded.

In general for an intermediate mass boson, the branching ratio for a minimal SM Higgs boson to $b\bar{b}$ is very close to that of the light CP-even state h^0. For large values of $\tan\beta$, the other neutral MSSM Higgs bosons decay predominantly into $b\bar{b}$, with a 3% branching ratio into $\tau^+\tau^-$. This simple pattern becomes more complex for smaller values of $\tan\beta$ [51] with modes such as $H^0, A^0 \to t\bar{t}$ (for $M_{A^0} \approx M_{H^0} > 2m_t$) and $H^0 \to h^0h^0$ and $A^0 \to Zh^0$ (for $M_{A^0} \approx M_{H^0} < 2m_t$) becoming more important. Despite more complicated cascade

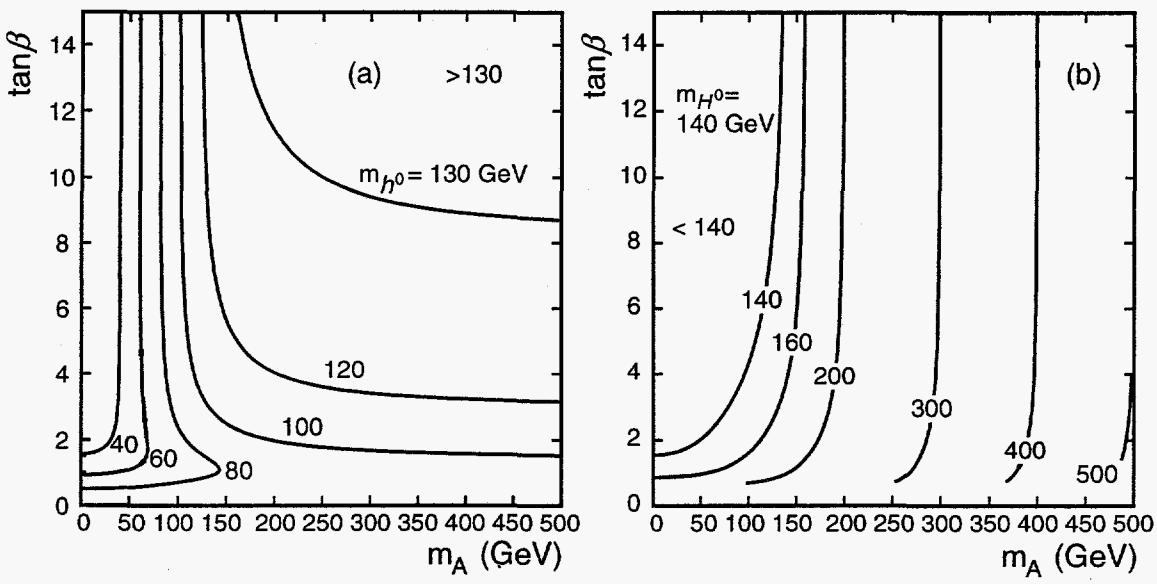

Figure 0.19: Contours of the values of (a) M_h and (b) M_H in the MSSM for $m_t = 180$ GeV, assuming $m_{SUSY} = 1$ TeV and maximal top squark mixing.

decays into lighter Higgs states, the bottom line remains clear: There should be plenty of jets from b-quarks to tag and elucidate signals. A case in point is the spectacular decay of H^0A^0 into six b jets $H^0 \to h^0h^0$, $h^0 \to b\bar{b}$. Most final states decay into at least four b-quark jets, underlining the overwhelming importance of b-tagging in experimental studies. An interesting case deserving further study in simulations is the heavy Higgs decay into $t\bar{t}^{(*)}$.

Experimental Studies

All of the topologies of Fig. 0.16 can be explored in the MSSM with the h^0 taking the role of the Standard Model Higgs boson. A repetition of the analyses described earlier either would observe a single h^0 similar to that of the SM Higgs, or, if $\sin^2(\beta - \alpha) \simeq 0.5$, would observe both the h^0 and H^0 states as shown in Fig. 0.20a [48].

An identical preselection for a four-jet topology can be used to search for HA. We require in this case that all four jets in $(H^0 \to b\bar{b})(A^0 \to b\bar{b})$ be tagged as b jets. For large enough M_A and $\tan\beta$, we have $M_A \simeq M_H$, and we can demand that the two jet-pair masses of the possible combinations to be close to equal. Then a signal as shown in Fig. 0.20b is possible. Since all the neutral SUSY Higgs decay into $\tau^+\tau^-$ at some level, it is possible to observe all three MSSM states in a single analysis by looking at the invariant mass of both the $\tau^+\tau^-$ and $q\bar{q}$ in the $\tau^+\tau^- q\bar{q}$ final state. In Fig. 0.21, we show the regions of plane of M_A versus M_h in which is it possible to observe all three neutral Higgs states of the MSSM at a linear collider with $\sqrt{s} = 500$ GeV, or, conversely the region where only the h^0 can be observed [53].

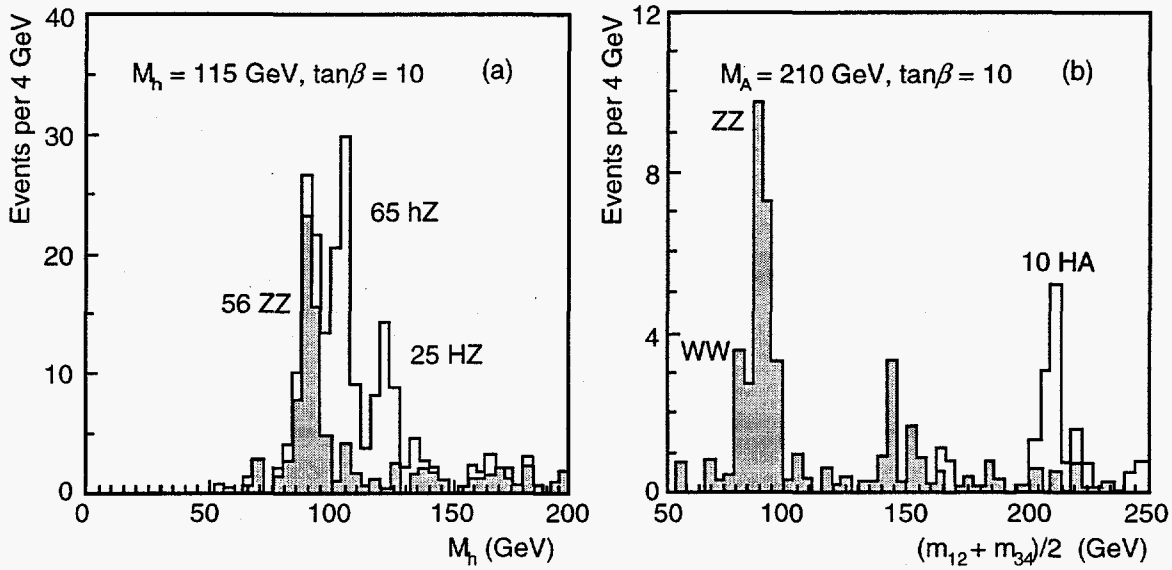

Figure 0.20: (a) Jet masses recoiling from a reconstructed Z^0 after b tagging for $\sin^2(\beta-\alpha) \simeq 0.5$, and integrated luminosity of 10^{-1} fb; (b) average of the two jet-pairs closest in invariant mass in an identified $b\bar{b}b\bar{b}$ final state with $M_A = 210$ GeV (adapted from [48]).

In theories with multiple Higgs doublets such as the MSSM, searches for the charged Higgs bosons $H^{\pm}$ are also important. An e^+e^- collider should be able to better resolve the hadronic decays of the $H^{\pm}$ compared to a hadronic collider, and all of the expected final states $H^+H^- \rightarrow c\bar{s}\,\bar{c}s$, $t\bar{b}\bar{t}b$, plus the easier topologies of $c\bar{s}\tau^-\nu$ and $\tau^+\nu\tau^-\overline{\nu}$ should be observable. A detailed simulation analysis [54] at $\sqrt{s} = 500$ GeV with an integrated luminosity of 10 fb^{-1}, which makes heavy uses of b-tagging, has shown that oen can establish a signal over the $e^+e^- \rightarrow t\bar{t}$ and W^+W^- background in all of these channels. The results show a detection sensitivity for charged Higgs bosons up to about 210 GeV at $\sqrt{s} = 500$ GeV, independent of decay mode. These conclusions can be strengthened further by adding the decay $t \rightarrow bH^+$. The bottom line is that if the A^0 is lighter than about 200 GeV, then the $H^{\pm}$ should be observable also.

If one is considering SUSY Higgs bosons, one should allow for the possibility of their decay into other SUSY particles. As an example, it is possible for h^0 or H^0 to decay into a pair of the lightest neutralinos (mixtures of fermionic partners of the Z and γ) that would be stable and neutral. The result would be an "invisible" decay of the Higgs. This topology can be identified in the same way as described previously by studying the missing mass in a hZ or HZ event where the Z decays into a pair of electrons or muons. Both missing mass resolution and backgrounds (smaller direct $Z\nu\overline{\nu}$ cross section) improve with lower center-of-mass energy, and such an analysis would benefit from running at $\sqrt{s} \simeq 300$ GeV. The possibility of SUSY Higgs decays into other SUSY particles [51] such as SUSY partners of quarks and leptons warrant further experimental simulations.

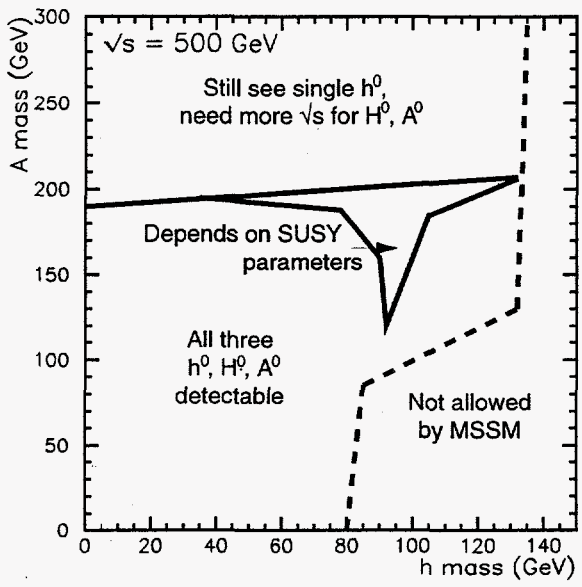

Figure 0.21: Regions of simultaneous detectability of h^0, H^0, and A^0 at center-of-mass energy of 500 GeV [53].

0.4.5 Determination of Properties of Higgs Bosons

Mass Measurement

To measure the mass of one or more of the possible Higgs bosons, one would probably optimize the running conditions to have smaller center-of-mass energy (for better momentum resolution) and as small a level of beamstrahlung as possible. For an intermediate mass Higgs, $\sqrt{s}$ = 200–300 GeV is appropriate. Under these conditions, one can precisely measure the recoil mass in $e^+e^- \to Z^0h^0$ events opposite to the reconstructed leptonic decay $Z^0 \to e^+e^-$ or $\mu^+\mu^-$. Other modes, such as the four-jet topology, can also be employed. In all cases, kinematic fitting would be used to constrain the leptons or jets from a Z^0 to reconstruct to M_Z and to allow for missing E_γ along the beam axis. A typical jet-jet mass resolution of $\sigma_M \simeq 2.0$ GeV can be achieved assuming the excellent momentum resolution of $\sigma_{p_t}/p_t = 1 \times 10^{-4} \oplus 0.1\%$ envisaged for the JLC detector [47]. For our NLC detector design, we could achieve $\sigma_M \simeq 3.9$ GeV, as shown in Fig. 0.22. The differences between detector designs are much smaller when kinematic constrained fitting is included in the analysis. The JLC-type detector has been estimated to provide a estimated precision on the Higgs mass of approximately 0.1% for $\sqrt{s}$ = 300 GeV, $\int L \cdot dt$ = 30 fb^{-1}, and a 2.0% full width beam energy spread [55]. On the other hand, the NLC-type detector gives $\Delta M_h \leq 160$ MeV up to $M_h \simeq 160$ GeV with 50 fb^{-1} at $\sqrt{s} = 500$ GeV.

Once M_H is known precisely, it can be used as an input to check the experimental measurements of branching ratios and the production cross section with Standard Model predictions. Its value can also be compared to the theoretical value obtained from precision

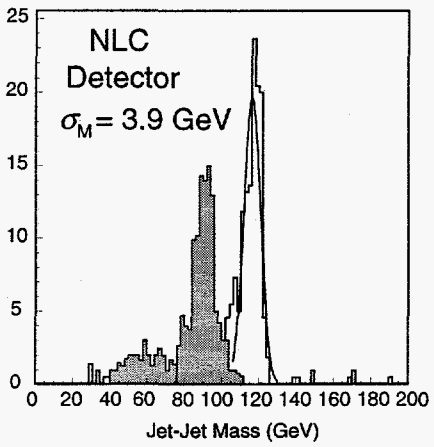

Figure 0.22: Mass resolution of $\sigma_M \simeq 3.9$ GeV in the jet-jet invariant mass for jets from Higgs decay assuming the performance of a NLC detector (see text) for a simulated signal (open histogram) of a 120 GeV SM Higgs boson and all known backgrounds (shaded histogram) at 300 GeV with 10 fb^{-1}.

electroweak measurements, combined with the measurements of M_W and m_{top} expected from a linear collider.

Cross Section Measurement

Measuring the production cross section of the Higgs provides one way of disentangling a SM Higgs boson from a SUSY Higgs, if one can observe the cross section suppression due to mixing

$$\sigma(e^+e^- \to h^0 Z^0) = \sin^2(\beta - \alpha) \cdot \sigma(e^+e^- \to h^0_{SM} Z^0).$$

A distinct advantage of e^+e^- linear colliders over hadronic colliders is the ability to almost unambiguously tag the Z^0 in hZ events and being able to study all of the decays $h^0 \to X$ with small backgrounds. Both total absolute cross sections and individual Higgs branching ratios can then be measured. By using leptonic decays of the Z^0 and kinematical fitting, the absolute production cross section can be measured [55] with a precision of 7% with an integrated luminosity of 30 fb^{-1} and to 5% with 50 fb^{-1}. However it should be kept in mind that for a large area of SUSY parameter space, the SUSY Higgs cross section is less than 10% different from the SM Higgs cross section.

Spin-Parity and CP Determination

In principle, the spin and parity of the Higgs boson can be found by studying both the production angular distribution of the Higgs and also the resulting angular distribution of the decay products of the Z^0 in its rest frame in HZ events. In the high energy limit, Table 0.6 shows the expected angular distribution of scalar (*e.g.*, h^0, H^0) and pseudoscalar (*e.g.*,

A^0) Higgs bosons. In the table, θ is the production angle of the Higgs boson and θ_* is the polar angle of the fermions from Z decay measured in the Z rest frame. In practice, however, a purely CP-odd Higgs boson couples to ZZ only at the one-loop level, and then the ZA cross section would be very small. For a Higgs boson that is a mixture of CP-even and CP-odd components, the production would mainly be sensitive to the CP-even part, and the angular distributions would not reveal the CP-odd component [56].

Table 0.6: Expected angular distributions for Higgs bosons with different spin-parity.

	Scalar, 0^{++}	Pseudoscalar, 0^{-+}
$d\sigma(e^+e^- \to \phi Z^0)/d\cos\theta$	$\propto \sin^2\theta$	$\propto (1-\sin^2\theta)$
$d\sigma(Z^0 \to f\bar{f})/d\cos\theta_*$	$\propto \sin^2\theta_*$	$\propto (1 \pm \cos\theta_*)^2$

A much better way to determine the Higgs' CP character is with polarized $\gamma\gamma$ collisions [57, 58]. In this technique, which we will discuss in detail in Section 9.2, the Higgs boson is produced as an s-channel resonance. Then it is possible to study the angular correlations of the decay products of the resonance in decays such as $\phi \to \tau^+\tau^-$ and $t\bar{t}$. By spin analyzing the subsequent decays $t \to b\ell\nu$ for top quarks from heavy Higgs boson decay, and $\tau \to \pi\nu$ or $\tau \to \rho\nu$ for CP-odd state can be distinguished [56, 59]. This CP state separation is much better in the angular correlations between top quark decay products.

Branching Ratio Measurements

The measurement of the branching ratios of any observed Higgs boson is an essential ingredient to understand the nature of the symmetry breaking and to make predictions about other aspects of the Higgs sector. This is especially when only a single neutral Higgs is observed, which might be either the Standard Model Higgs or the lightest neutral Higgs from SUSY. The clean environment in e^+e^- annihilation permits one to tag a Z^0 in one hemisphere, and then observe the decay $h^0 \to X$ in any decay mode in the opposite hemisphere. An example of such an analysis [49] at $\sqrt{s} = 400$ GeV simulating an SLD-like detector first identifies a Z^0 in a HZ event and then considers those decays where the recoiling Higgs decays into jets. The Higgs decays to two jets can be separated by flavor by counting the number of tracks with a significantly large impact parameter: $b_{norm} = b/\sigma_b > 3$, where b is the impact parameter and σ_b is the error on b. The decay $h \to WW^{(*)}$ is identified by demanding that the event be consistent with containing six jets, and that a jet pair with invariant mass close to the W mass is found. With 50 fb^{-1} of data, $Br(h \to b\bar{b})$ can be measured to a statistical precision of 7%, and branching ratios into WW^* and $(c\bar{c}+gg)$ to 24% and 39% respectively. These relative errors are shown superimposed upon the Standard Model values in Fig. 0.23a. The figures also shows the variation in branching ratios that one would expect from the

variation of $\tan\beta$. In the MSSM, it is very difficult to arrange such a large variation in $\tan\beta$ without a compensatory variation in α, but the figure shows the utility of this measurement in Higgs studies in a more general context. For the comparison of the Standard Model Higgs boson to the MSSM, one should consult Fig. 0.23b, where the branching ratio of a light Higgs boson into $b\bar{b}$ is compared for these two possibilities over the MSSM parameter space.

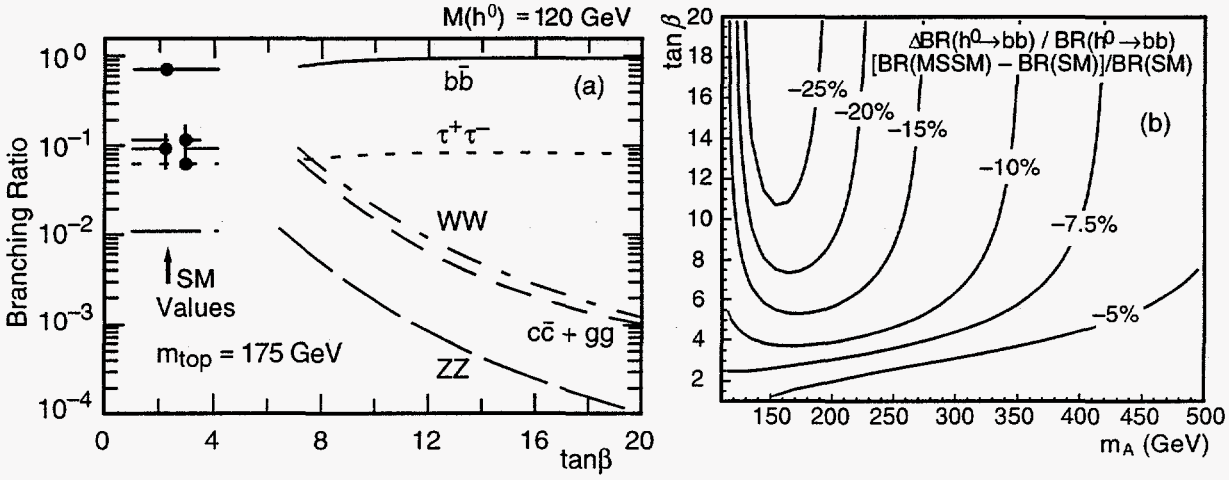

Figure 0.23: (a) Expected errors on the Standard Model branching fractions compared to those predicted for a 120 GeV h^0 MSSM Higgs boson; (b) contour lines of fractional deviation of $Br(h^0 \to b\bar{b})$ ($m_t = 175$ GeV, $m_{SUSY} = 1$ TeV).

An interesting quantity [61] is the ratio of branching ratios to $c\bar{c}$ versus $b\bar{b}$. At tree level,

$$\frac{Br(h \to c\bar{c})}{Br(h \to b\bar{b})} \approx \frac{m_c^2}{m_b^2} \cdot \left(\frac{M_h^2 - M_A^2}{M_A^2 - M_Z^2} \right)^2 ,$$

where m_c and m_b are the c and b quark masses respectively. (We should note that this formula can receive substantial radiative corrections in some regions of the MSSM parameter space.) If the branching ratios indicated are measured along with M_h, it is possible to estimate M_A. In a simulation study of this measurement [62] at $\sqrt{s} = 300$ GeV, HZ events are selected for each decay mode of the Z^0, and the decay mode of the Higgs is determined using three-dimensional impact parameters. Flavor tagging is performed by selecting charged tracks that satisfy $b/\sigma_b \geq 2.5$ and counting the number in each jet from the Higgs decay. For $M_H = 120$ GeV, 50 fb^{-1} of data, and assuming 90% polarization of the electron beam, the statistical error on the ratio of branching ratios $Br(h \to c\bar{c}+gg)/Br(h \to b\bar{b})$ would be 20.4%, varying with the Higgs mass as shown in Fig. 0.24a. This does not include a substantial systematic uncertainty from m_c/m_b, which we believe will be reduced in the next few years through lattice gauge theory calculations. Then, as shown in Fig. 0.24b, this measurement could be sensitive to A^0 masses to 400 GeV, well above the maximum kinematic reach of a 500 GeV collider. Observation of the A^0 in this way would help to plan the next step in energy.

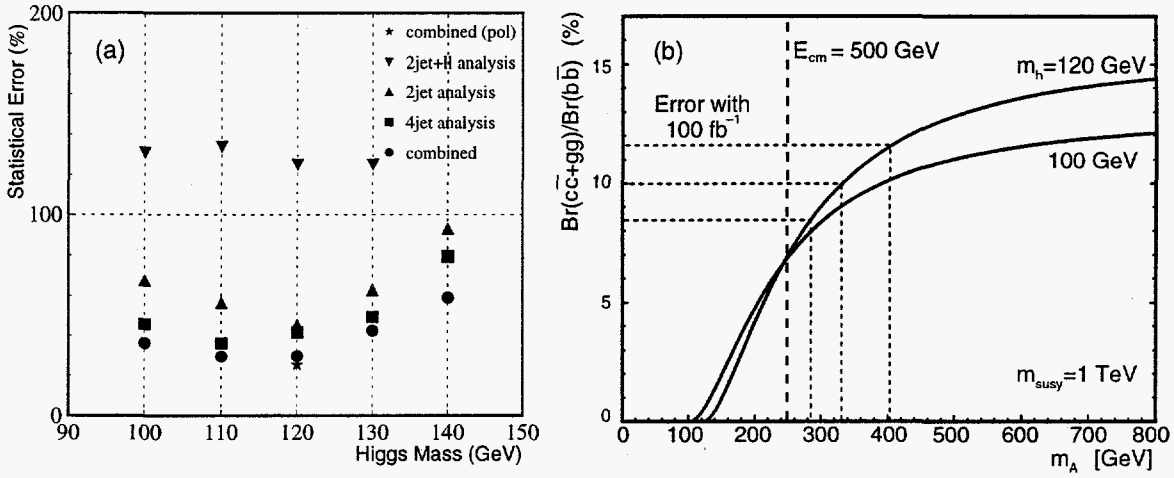

Figure 0.24: (a) Statistical error with 50 fb^{-1} of data on $Br(h \to c\bar{c} + gg)/Br(h \to b\bar{b})$ as a function of Higgs mass; (b) implications for estimation of A^0 mass.

For the decay $h \to \gamma\gamma$, it is difficult to measure the branching ratio at an e^+e^- collider because this mode is relatively rare. However, it should be possible to measure the absolute partial width $\Gamma(h \to \gamma\gamma)$ by exploiting the ability of an electron collider to be run as a $\gamma\gamma$ collider. This measurement is discussed in Section 9.2.

Determination of Higgs Total Width

In the preceding sections, we have indicated many ways in which measurements at the NLC can distinguish between the Standard Model Higgs and the light Higgs h^0 of the MSSM. There are also a number of quantities at the LHC which are sensitive to this difference, as outlined in [35]. However, to obtain the complete set of partial width of the Higgs boson in a model-independent way, measurements from LHC must be combined with data both from e^+e^- and $\gamma\gamma$ collisions at the NLC. A possible procedure is the following. First determine $Br(b\bar{b})$ from Zh events and combine with $\sigma(WW \to h) \cdot Br(b\bar{b})$ both measured at the NLC to obtain the WWh coupling. Alternatively, a measurement of $\sigma(e^+e^- \to Zh)$ at the NLC gives the ZZH coupling and ratio of the WWh and ZZh couplings given by $M_W^2/M_Z^2 = \cos^2\theta_W$ also gives the WWh coupling. This coupling and a measurement of $\sigma(Wh) \cdot Br(\gamma\gamma)$ at the LHC can be used to determine $Br(\gamma\gamma)$. Therefore one can combine $Br(b\bar{b})$ with the $\gamma\gamma$ collider measurement of $\sigma(\gamma\gamma \to h) \cdot Br(b\bar{b})$ to obtain $\Gamma(h \to \gamma\gamma)$. We can then finally compute the total width $\Gamma_h^{\rm tot} = \Gamma(h \to \gamma\gamma)/Br(\gamma\gamma)$ and $\Gamma(h \to b\bar{b}) = Br(b\bar{b})\Gamma_h^{\rm tot}$. A simpler route exists using only e^+e^- data when the Higgs boson is heavy enough that the branching ratio to WW^* is relatively large, so that it can be measured accurately. In this case, we can simply measure $Br(h \to WW^*)$ and infer $\Gamma_h^{\rm tot} = \Gamma(h \to WW^{(*)})/Br(WW^{(*)})$. Although the accumulation of errors may be significant, the basic point is that data from all three colliders or from the NLC alone can be combined to complete a *model-independent* determination of

the properties of a light Higgs boson.

0.4.6 Summary

From the studies described, the discovery of a Standard Model intermediate-mass Higgs boson at an e^+e^- linear collider at $\sqrt{s} = 500$ GeV can easily be achieved with an integrated luminosity of only 10 fb^{-1}. Such a machine allows the detection of *at least* the lightest MSSM Higgs h^0, if not all three SUSY neutral states. If the lightest Higgs is not observed, then not only is the Minimal Supersymmetric Standard Model ruled out, but also the general idea that the Higgs boson is a fundamental particle up to the unification scale is called into question. If the A^0 is not kinematically accessible at $\sqrt{s} = 500$ GeV, then the measurement of h^0 branching ratios can give hints of the values of M_A and $\tan\beta$ and tell us where to go next in energy. For definitive evidence, $\sqrt{s} > 2M_A$ would still be needed. For Higgs bosons above the intermediate mass range, their decay into pairs of vector bosons makes them straightforward to detect at the NLC as at the LHC; however, more up-to-date experimental simulations are needed. Just as important as its ability to discover the Higgs boson is the ability of the linear collider to make precision measurements of the properties and couplings of a Higgs boson. Even if the Higgs boson is discovered earlier at LEP2 or at the LHC, we will need the NLC to learn its complete story.

0.5 Supersymmetry

To build a complete unified theory with a fundamental Higgs boson, one is led to introduce supersymmetry, the symmetry between fermions and bosons in space-time. Supersymmetry is the only known principle with sufficient structure to allow the construction of grand unified theories in which fundamental scalar particles can naturally be very light compared to the unification scale. Supersymmetric unification models explain the values of the Standard Model coupling constants as measured at Z^0 energies, and also incorporate a mechanism of electroweak symmetry breaking associated with the heavy top quark. General reviews of supersymmetric models can be found in [36, 37, 63, 64]. Supersymmetry also offers the more speculative but tantalizing possibility of a connection between phenomena observable at collider energies and string theory and other profound mathematical theories of the fundamental forces [65, 66].

In this section, we will examine the manner in which supersymmetry (SUSY) might manifest itself at a 0.5-1.0 TeV e^+e^- Linear Collider (NLC). Our discussion here is part of a broader, and continuing, investigation. At present, our study is being carried out within the supersymmetry scenario based on the minimal supergravity model with gauge coupling unification and radiative electroweak symmetry breaking (SUGRA). We have calculated most of the relevant cross sections and angular distributions for the production and decay of supersymmetric particles, and we include a report of them as an appendix [67]. Because of the difficulty of knowing where and how supersymmetry will manifest itself, we must study the phenomenology of supersymmetry over a wide range of its parameters. In this study, we have chosen five points in the parameter space of the SUGRA model which illustrate qualitatively different possibilities for the spectrum of new particles [67]. Because of the power of the experimental tools offered by the NLC, our goals are much more ambitious than simply to discover the existence of supersymmetry. We would like to measure the masses of supersymmetric particles with precision, and determine the underlying values of the basic parameters of the theory. In the most optimistic scenario, the extrapolation of these parameters to the unification scale would give evidence into the details of the fundamental unified model [68].

The number of supersymmetric particles is quite large. Hence, it is typical that many of these particles will be produced in the same data sample at a particular energy center-of-mass energy. One of the properties of e^+e^- linear colliders is that the electron can be longitudinally polarized and its orientation can be changed at will. Already, the SLC provides an electron beam with 77% polarization. We expect that, in the future, this magnitude can be increased substantially. The ability to have electron beams with high longitudinal polarization is very useful to discriminate between the various supersymmetric signals and to understand and remove the Standard Model background processes [69]. This can be seen by examining the standard model cross sections as a function of polarization, shown already in Fig. 0.3, and comparing these to the polarization-dependence of the cross sections for the supersymmetric production processes, shown for two representative points in Fig. 0.25. Having a 90% longitudinally polarized electron in the right handed mode will reduce the production

rate of Standard Model background processes such as W^+W^- pair production by an order of magnitude while enhancing some of the supersymmetric particle signals. The left-handed supersymmetric particles, like the Standard Model background, are also suppressed, while the right-handed ones are enhanced. This is seen in Fig. 0.25. Hence, by varying the polarization we can determine which of the supersymmetric particles are giving us a particular signal. Polarization of the positrons could give an additional advantage. For example, if we could collide totally right-handed electrons with totally left-handed positrons, all of the standard model backgrounds from e^+e^- annihilation processes would disappear, while the supersymmetric signals from $\tilde{e}_R^-\tilde{e}_R^+$ production would remain. (Some background would also remain due to two-photon reactions [70].) An additional handle on our ability to discriminate among the various supersymmetric signals is their different angular distributions [67]. These distributions for a typical case are shown in Fig. 0.26. A third powerful discriminating tool is the adjustment of the center-of-mass energy. Once one has an estimate of the masses of the lightest supersymmetric particles, it is advantageous to decrease the energy of the collider so that only these lightest states are produced, measure their properties at this lower energy, and then increase the energy of the collider systematically.

In our study, have generated signal and background processes using the simulation program ISAJET [2]. This program allows for both electron and positron longitudinal polarization. The influence of the detector is accounted for by smearing the generated momenta and directions of the particles produced in the simulation with resolution functions as described in Section 2.

The spectrum of supersymmetric particles for the five parameter sets that we have chosen for detailed study are exhibited in Table 0.7. These spectra are computed consistently from a supergravity model with $m_t = 180$ GeV. The values of the underlying parameters for these scenarios is given in [67].

In each of the five cases, the lowest mass supersymmetric particle is the χ_1^0. In the class of models we discuss, there is a conserved R-parity which implies that this particle is stable. It then passes through the detector without leaving a signal. This particle is in all cases sufficiently massive that it carries away significant missing energy. On the other hand, Standard Model background processes can mimic this signal because, as a result of their peaked differential cross-section in the forward and backward directions [67], many of the particles in the final state go along the beam direction. Also it is possible that neutrinos can carry away a sizable portion of the energy, or that the event is mismeasured due to the detector resolution.

In Fig. 0.27 we show the expected observed energy for the Standard Model processes $e^+e^- \to W^+W^-, Z^0Z^0, q\bar{q}$ after a requirement that at least three particles be present in each hemisphere. This allows us to avoid including the $e\nu W$ final state and most of the events where the W's and Z's decay into leptons and neutrinos; only a few events with τ in the final state remain. The figure shows the effect of various assumptions about the calorimetric coverage in $\cos(\theta)$, to determine how much energy is lost in the beam direction. We note that the tail of events with low visible energy (E $\approx$ 100 GeV or less) begins to increase noticeably

Table 0.7: Supersymmetric particle masses at five representative points in the parameter space of phenomenological supergravity models.

Parameter Set	1	2	3	4	5
χ_1^0	85.87	128.51	44.41	77.83	57.00
χ_2^0	175.24	257.05	96.73	115.29	111.21
χ_3^0	514.96	549.08	267.81	146.84	440.03
χ_4^0	523.78	556.07	284.18	292.40	460.12
$\chi_1^\pm$	175.12	257.02	96.10	96.06	109.82
$\chi_2^\pm$	522.82	555.72	282.52	292.45	457.09
h^0	84.86	92.24	68.82	130.58	102.15
H^0	766.47	698.24	389.39	201.72	619.21
A^0	762.32	693.30	381.75	200.00	616.45
$H^\pm$	765.70	697.05	388.81	214.75	620.52
$\tilde{q}_L$	605.23	670.84	317.23	1000.00	464.04
$\tilde{b}_L$	516,58	621.43	272.31	1000.00	384.70
$\tilde{t}_1$	417.65	537.12	265.55	923.13	179.85
$\tilde{q}_R$	605.23	670.84	317.23	1000.00	464.04
$\tilde{b}_R$	597.15	655.70	313.40	1000.00	457.79
$\tilde{t}_2$	547.20	655.21	328.15	1099.35	495.72
$\tilde{l}_L^-$	425.96	238.35	215.72	1000.00	320.69
$\tilde{\nu}_L$	421.43	230.16	206.63	1000.00	314.65
$\tilde{l}_R^-$	408.80	156.97	206.54	1000.00	307.45
$\tilde{g}$	552.19	760.16	298.15	900.00	428.03

for $\cos(\theta) < 0.97$ or so. Hence good calorimetric coverage is imperative if we want to use the low visible energy as a signal for supersymmetric particles. We do not smear the particles in this plot to determine the true loss of particles down the beam direction. The detector design presented in this report has calorimetric coverage down to $\cos(\theta) = 0.99$, which, as we will see, is sufficient to allow us to see the signal due to supersymmetric particles.

We have made a study of the signals seen in the various sets of SUGRA parameters [67]. We show here some of the results for the signal to background ratios for the SUGRA parameter set 4. In this scenario, the main signals are due to the pair-production of the charginos $\chi_1^{\pm}$ and the neutralinos χ_1^0, χ_2^0. The visible (observed) energy for these signals and the others [67] is shown in Fig. 0.28. The signal is in the region of 100 GeV visible energy; hence our requirement that there needs to be calorimetric coverage down to small angles. In Fig. 0.29 we show the visible energy distribution, properly normalized with the relative cross section for background Standard Model events and signal from supersymmetric events. A small bump can be observed in the region of small visible energy. To isolate the signal due to chargino ($\chi_1^+\chi_1^-$) production, we require that there be at least five hadrons in each hemisphere. After additional cuts in the data to enhance the signal, we are able to obtain a signal to background ratio of 12 to 1 as shown in Fig. 0.30. This signal is then used to determine the masses of the $\chi_1^{\pm}$ and the χ_1^0 as described below. Similarly, with appropriate cuts we obtain a signal for $\chi_2^0\chi_1^0$ production with no background from the Standard Model processes, but, as shown in Fig. 0.31, a background of $\approx 10\%$ background from $\chi_1^+\chi_1^-$. (We expect to reduce this background with further analysis.) The complete observed signal is shown in Fig. 0.32. This can then be used to determine the masses of the χ_2^0 and χ_1^0. It is interesting to check that the two determinations of the χ_1^0 mass agree. This self consistency would give us confidence that we are seeing the consequences of a consistent model and would encourage us to use the resulting model parameters to predict the masses of the other particles. These levels of signal to background seen in this analysis are typical for scenarios of supersymmetric particle production processes in e^+e^- colliders.

We will now discuss in more detail the measurement of the masses, spins, and cross-sections of the various possible supersymmetric signals. Some very beautiful studies on these issues have already been reported in [68], [71], [72]. These papers indicate that, indeed, linear collider experimentation provides very powerful methods by which to measure the production and decay parameters of the various supersymmetric particles. This should allow us to uncover which of the various supersymmetric models is the correct one. One recent study [68] has shown that, for slepton or chargino pair-production, we can use the upper and lower limits of the energy spectrum of the secondaries from supersymmetric particle decays to determine these particle masses. In addition, we can use the angular distribution of the signal to say something about the spin of the sparticles producing these distributions. A threshold scan will also differentiate between scalars and fermions by determining whether the energy dependence follows a a β or a β^3 law.

In this study, we expand on this work by increasing the number of cases that have been studied and attempt to determine how much these measurements constrain the possible region of parameter space. Here we will describe how well we can determine the masses

of the supersymmetric particles using the simulated resolution parameters in our detector design. For brevity, we will only consider here the parameters sets 3 and 5. In case 3, the most important supersymmetry cross section for an incident 95% left-hand polarized electron beam is that of of sneutrino pair production, $\tilde{\nu}_e\tilde{\nu}_e$, as shown in Fig. 0.25. The branching ratio for $\tilde{\nu}_e \to e^-\chi_1^+$ is 61%. The χ_1^+ decays mostly to $W^+\chi_1^0$. Hence, 5-10% of the time we can have a final state signal $e^\mp e^\pm\mu^\pm$ +2 jets. This signal will have hardly any Standard Model background. The energy distribution of the $e^\mp$ can be used to determine the $\tilde{\nu}_e$ mass. The $e^\mp$ energy spectrum, based on a 20 fb^{-1} data sample, is shown in Fig. 0.33. The background is shown by the dotted line. A fit to this energy spectrum leads to the following values for the masses:

$$M_{\tilde{\nu}_e} = 207.5 \pm 2.5 \quad (4) \quad \text{GeV}$$

$$M_{\chi_1^+} = 97.0 \pm 1.2 \quad (2) \quad \text{GeV}$$

at the 68% (90%) confidence level. These results should be compared with the input values, given in the table, of 206.6 and 96.1 GeV respectively.

Another interesting signal is the $\tilde{e}_L^+\tilde{e}_L^-$ process in order to determine the mass of the $\tilde{e}_L$ (left-handed slepton). The useful signal is due to the decay chain $\tilde{e}_L^- \to e^-\chi_2^0 \to e^-Z^0\chi_1^0 \to e^-\mu^-\mu^+\chi_1^0$. This leads to a final state with one electron, one positron, four muons, and a small visible energy. We can also consider the analogous decay chain for $\tilde{\mu}_L^+\tilde{\mu}_L^-$. We considered these two possibilities together by isolating final states with 6 leptons and missing energy, in which the highest energy leptons are either e^+e^- or $\mu^+\mu^-$. This analysis assumes that $\tilde{e}_L^-$ and $\tilde{\mu}_L^-$ have the same mass; with higher statistics, a mass splitting would be apparent. The results for an effective 1 year run (50 fb^{-1}) is shown in Fig. 0.34. The fit to the lepton energy spectrum gives the following values for the masses:

$$M_{\tilde{e}_L} = 221.6 \pm 5.6 \quad (8) \quad \text{GeV}$$

$$M_{\chi_2^0} = 94.7 \pm 5.3 \quad (10) \quad \text{GeV}$$

Since $M_{\tilde{\nu}} - M_{\tilde{e}_L}$ is determined by just $SU(2)$ symmetry, these measurements lead to a model-independent constraint on the parameter $\tan(\beta)$ according to the equation:

$$M_{\tilde{\nu}}^2 - M_{\tilde{e}_L}^2 = M_W^2 \cos(2\beta)$$

The fit to the lepton energy spectrum gives the following values for the masses:

$$M_{\tilde{e}_L} = 221.6 \pm 5.6 \quad (8) \quad \text{GeV}$$

$$M_{\chi_2^0} = 94.7 \pm 5.3 \quad (10) \quad \text{GeV}$$

at the 68% (90%) confidence level, which are quite close to the input values of 215.7 and 96.8 GeV in spite of the low statistics in this sample.

In the case of SUGRA parameter 5 we have a series of signals whose masses can be determined. This point includes a low mass stop squark $\tilde{t}_1$, a chargino χ_1^+, neutralinos χ_1^0

and χ_2^0, and the light Higgs boson h^0. We measure the χ_1^+ and χ_1^0 masses by studying the production process $e^+e^- \rightarrow \chi_1^+ + \chi_1^-$. For a 95% left handed polarized electron the cross-section is ≈ 0.75 pb so that for a 1 year run at our standard luminosity we get over 10^4 events. The χ_1^+ decays into the 3 body final states $q\bar{q}\chi_1^0$ and $e\nu\chi_1^0$, with the branching ratios predicted for the Standard Model W boson decay into the similar channels. Hence, about 68% of the time it will decay into two hadronic jets + χ_1^0. To isolate this signal we use similar cuts to those discussed above associated with Fig. 0.30. The resulting E_{jj} values, the energies of each of the 2 jet systems from the $\tilde{\chi}_1^+$ decays, has no sharp end point behavior due to the 3 body nature of its decay. Hence we cannot easily use the E_{jj} spectrum to determine the masses. Since the combined mass of the 2 jets, M_{jj} does not vary much in this case, and since we have a large sample of events, we can force two body kinematics on this process by selecting a slice of M_{jj} around a given value, which in our case is chosen to be 30 GeV. Hence the E_{jj} distribution follows approximately the two body kinematics of the process $\tilde{\chi}_1^+ \rightarrow \tilde{\chi}_1^0 + (jj)$ (30 GeV). The E_{jj} distribution and the best mass fit to the data is shown in Fig. 0.35. The result is:

$$M_{chipa} = 107.5 \pm 6.5 \text{ GeV}$$

$$M_{\tilde{\chi}_1^0} = 55.0 \pm 3.5 \text{ GeV}$$

at the 68% confidence level. This is to be compared with the input values of 109.8 and 57.0 GeV respectively.

Finally, for parameter point 5, we have also studied determining the mass of the $\tilde{t}_1$ (stop) quark. Here we note that the process $e^+e^- \rightarrow \tilde{t}_1^+\tilde{t}_1^- \rightarrow b\tilde{\chi}_1^+\bar{b}\tilde{\chi}_1^-$ occurs with a 100 % branching ratio. Since this cross section hardly depends on the electron polarization we study this case with a 95% right handed polarized electron ($P_L(e^-) = -0.9$) to minimize the background from WW pair production [67]. We isolate the events with ≥ 5 jets, and we select from these events with two tagged b's, and no isolated leptons or τ jets. Finally we require a missing mass > 140 GeV. For our standard 1 year run we obtain a SUSY signal of 286 events with a WW background of 36 events. The energy distribution of the b-jets is shown in Fig. 0.36. This distribution depends on the mass of the $\tilde{t}_1$ and the mass of the $\tilde{\chi}_1^+$. The masses we obtain are:

$$M_{\tilde{t}_1} = 182 \pm 11 GeV$$

$$M_{\tilde{\chi}_1^+} = 114 \pm 8 GeV$$

to be compared with the input values of 180 and 110 GeV respectively. Other interesting work on squark mass determination [73] has also been carried out.

We hope that in this short presentation we have indicated the effectiveness of an 0.5-1.0 TeV e^+e^- Linear Collider in determining the masses of the Supersymmetric particles. We have not discussed how to determine the spin of these. This we propose to accomplish where possible by looking at their production angular distribution and by looking at their production behavior as a function of the electron longitudinal polarization. This work will

continue in order to determine further what additional parameters need to be determined to be able to guarantee that the signals we are observed are due to supersymmetric particles.

To conclude, we make a brief comparison of the relative reach capabilities of a 0.5-1.5 TeV e^+e^- Linear Collider and the CERN LHC pp collider as to their ability to determine whether the observed signals are due to supersymmetric particles. First of all, the NLC, operating at $E_{cm} \geq$ 250-300 GeV should be able to search for the light Higgs boson, h^0, over the entire parameter space range of the minimal supersymmetry model. If the NLC does not observe the h^0, then this model must be ruled out. In addition, since the h^0 is expected to behave very nearly like a Standard Model Higgs boson, even if it is discovered, it may be difficult to tell if it is a SUSY or Standard Model Higgs. Hence, discovery of the h^0 alone may not be sufficient evidence for supersymmetry. On the other hand, the NLC has a substantial ability to discover many of the superpartners.

In Fig. 0.37, we show our estimates of the reach of NLC and LHC into the SUGRA parameter space, defined by underlying mass parameters m_0 and $m_{1/2}$. In the top figure, we have plotted the contours corresponding to $\tilde{\ell}_R$ and $\tilde{\chi}_1^{\pm}$ masses of 250, 500 and 750 GeV, approximately representing the reach of NLC(0.5 TeV), NLC(1.0) and NLC(1.5) in observing these supersymmetric particles. We also show the reach for supersymmetry recently calculated [74] for the CERN LHC assuming 10 fb^{-1} of integrated luminosity. Comparing the two figures we note that the reach of the LHC is larger than that of the NLC at 500 GeV, but its reach is comparable to that of the NLC at 1 TeV. It is important to note that the reactions at NLC and LHC typically access different particles in the supersymmetry spectrum, so the experiments at these colliders should be considered cooperative rather than competitive. In addition, precision measurements of particle properties such as mass, spin, and mixing angles will be much easier at the NLC [68] than at the LHC. The LHC might be able to provide complementary information via squark and gluino production channels which may not be accessible at the NLC.

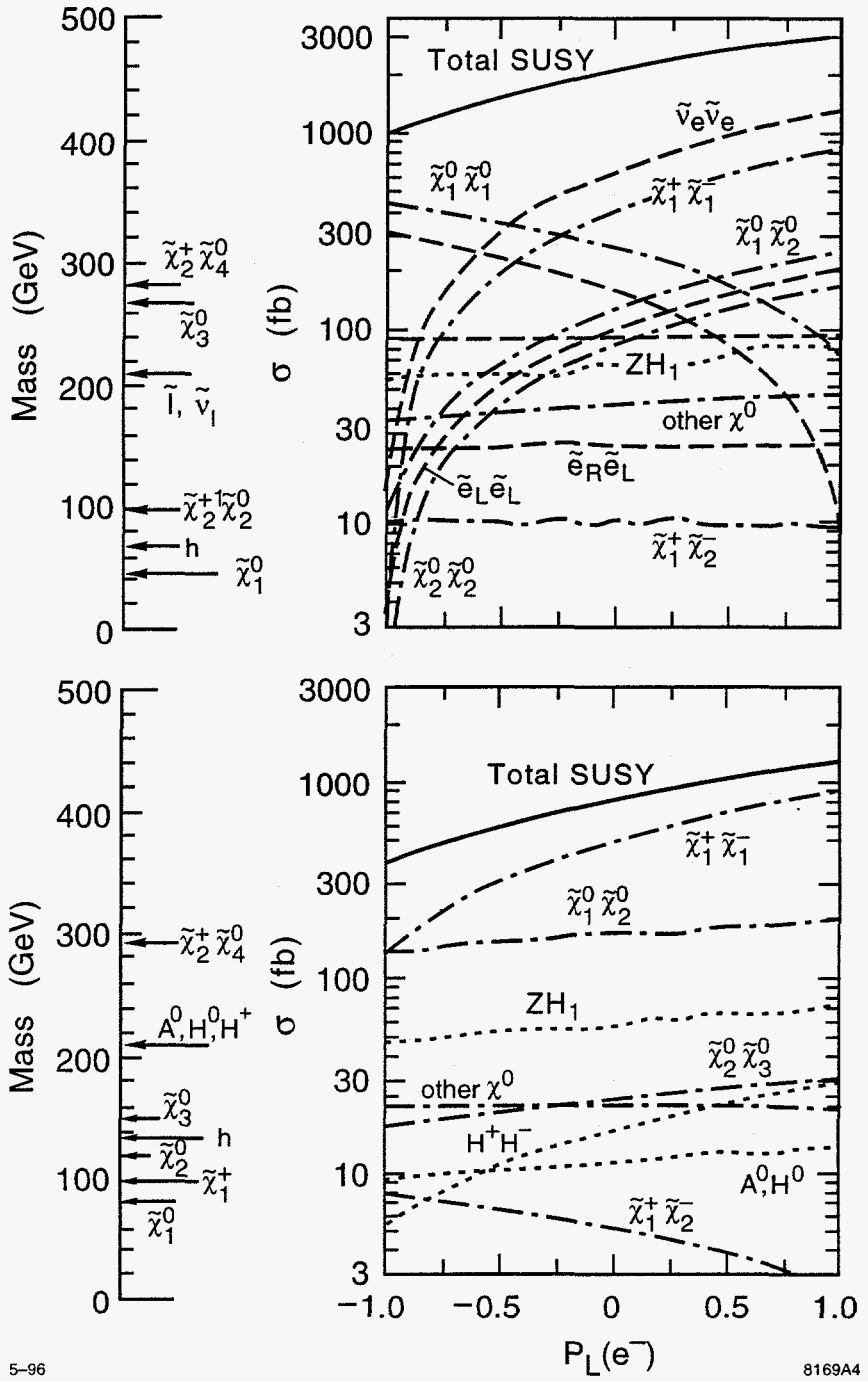

Figure 0.25: The cross section of Supersymmetric particle production at $E_{cm} = 0.5$ TeV as a function of the electron polarization for points 3, 4 in our parameter space.

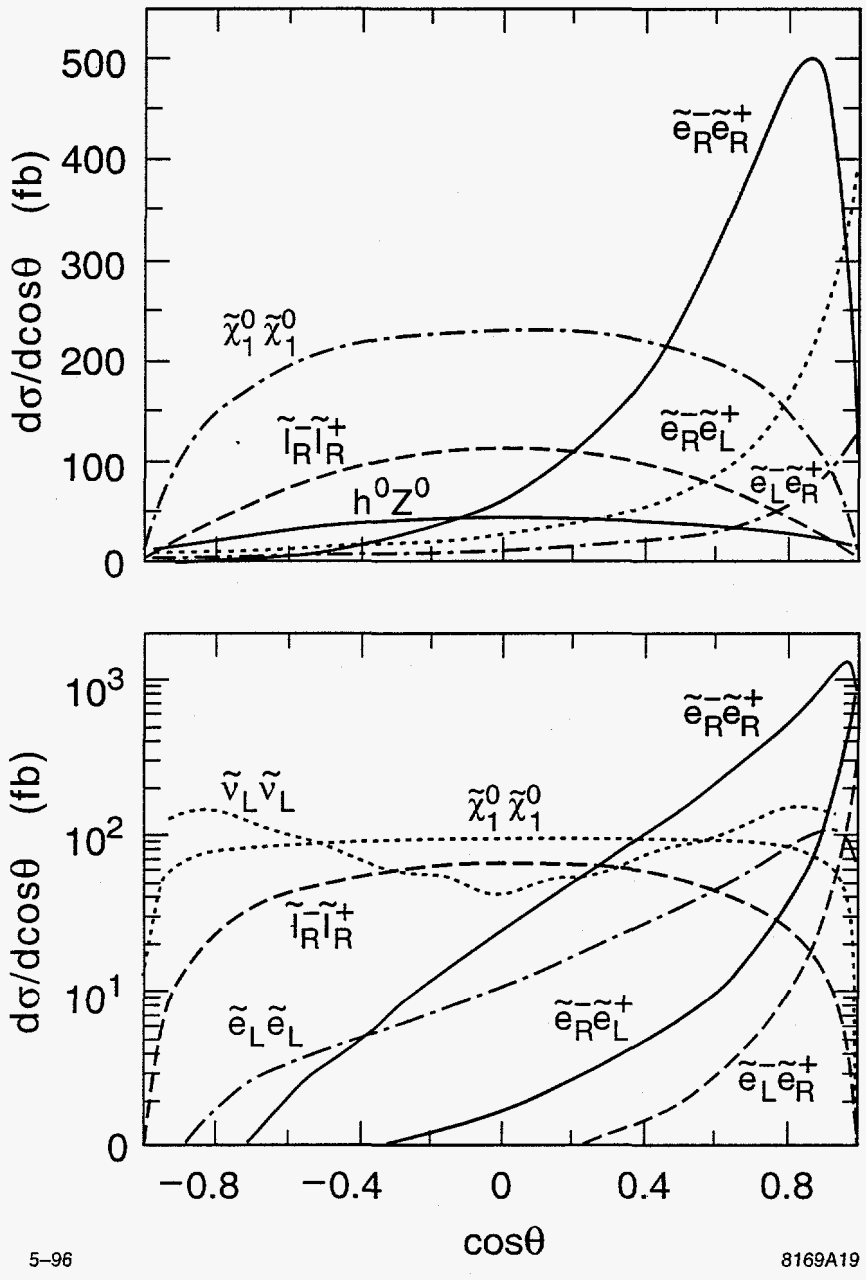

Figure 0.26: The differential cross section of supersymmetric particle production for an 80% polarized right handed electron at $E_{cm} = 0.5$ and 1.0 TeV for point 2 in our parameters list.

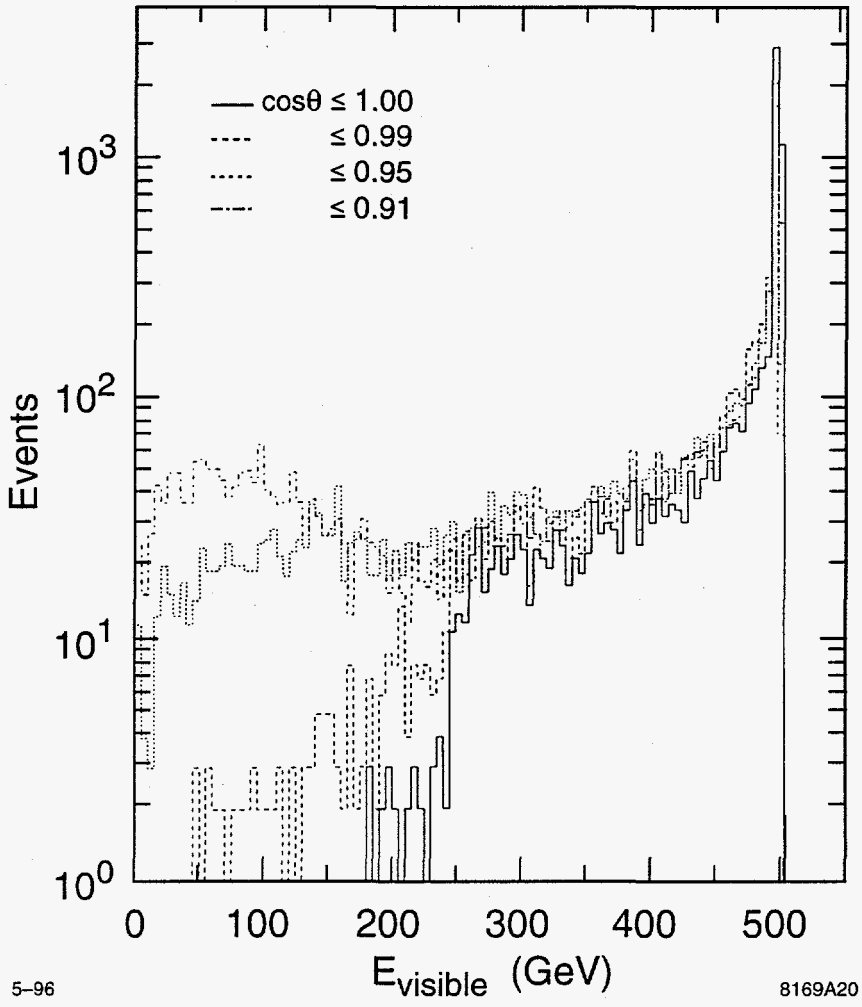

Figure 0.27: The Visible Energy for Standard Model final states W^+W^-, Z^0Z^0, $q\bar{q}$ for various calorimetry coverage. We require that there be at least 3 particles in each hemisphere.

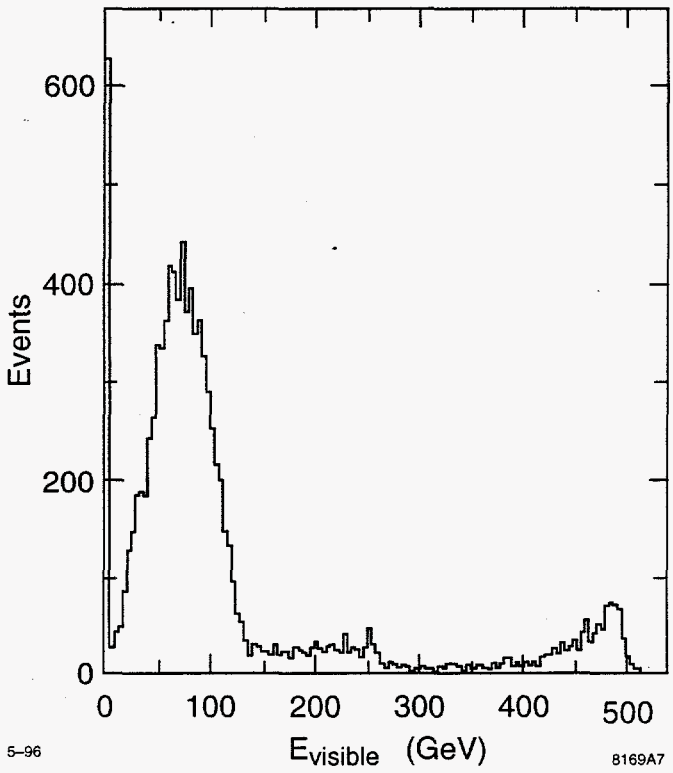

Figure 0.28: The visible energy for the supersymmetric processes defined by the SUGRA parameter set 4 after detector resolution smearing. The peak at 0 is due to $\tilde{\chi}_1^0\tilde{\chi}_1^0$ and $\tilde{\chi}_2^0\tilde{\chi}_1^0 \rightarrow \nu\overline{\nu}\tilde{\chi}_1^0\tilde{\chi}_1^0$ processes. The broad small peak at 500 GeV is due to Z^0h^0, H^+H^-, and H^0A^0 final states.

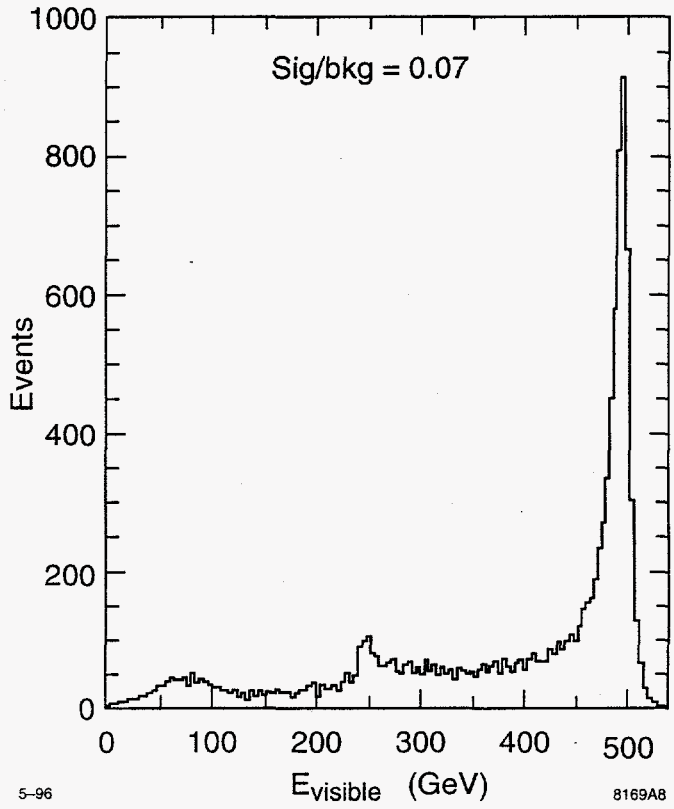

Figure 0.29: The visible energy for the normalized (relative cross-section) SUSY processes associated with SUGRA parameters 4 and the Standard Model processes. The smearing due to detector resolution is included.

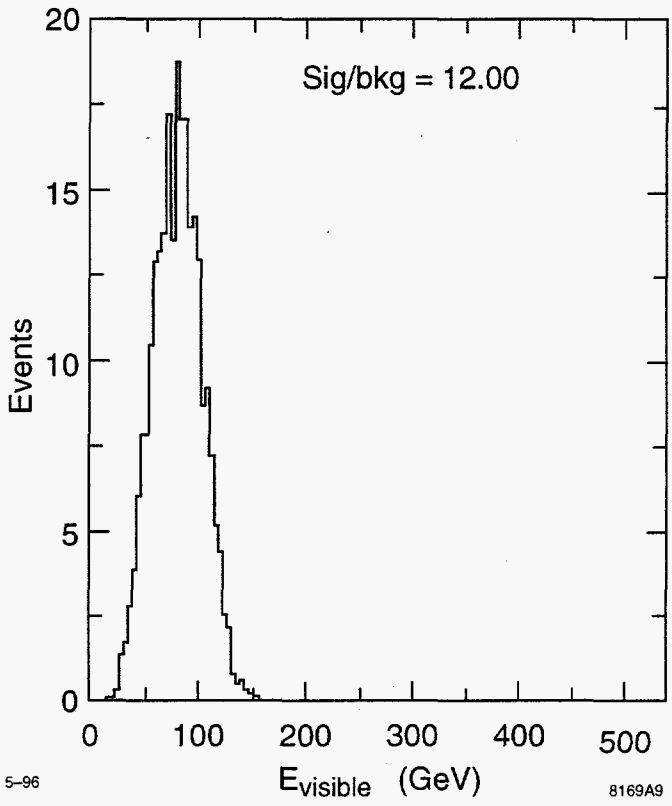

Figure 0.30: The visible energy for the normalized (relative cross-section) SUSY process $e^+e^- \rightarrow \chi_1^+\chi_1^-$ associated with parameter set 4 and Standard Model processes after cuts to enhance the signal over background. The cuts are that there be only 1 broad jet with > 5 particles and with $E_{vis} < 80$ GeV in each hemisphere.

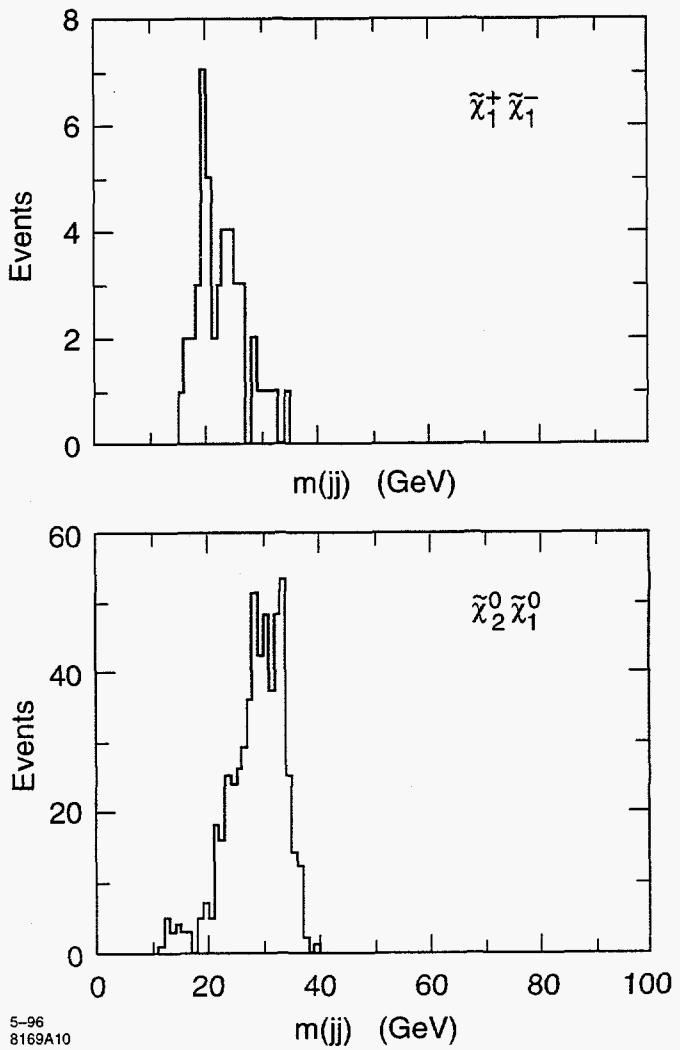

Figure 0.31: The 2-jet mass distribution for the processes $e^+e^- \rightarrow \chi_1^+\chi_1^-(\chi_1^0\chi_2^0) \rightarrow q\bar{q}\chi_1^0 q\bar{q}\chi_1^0(\chi_1^0 q\bar{q}\chi_1^0)$. The cuts require 2 jets with more than 1 particle in each and both jets in one hemisphere only. $E_{visible} < 125, 70$ GeV for the two jets, and $\cos(\theta) < 0.85$ for the thrust axis of the event.

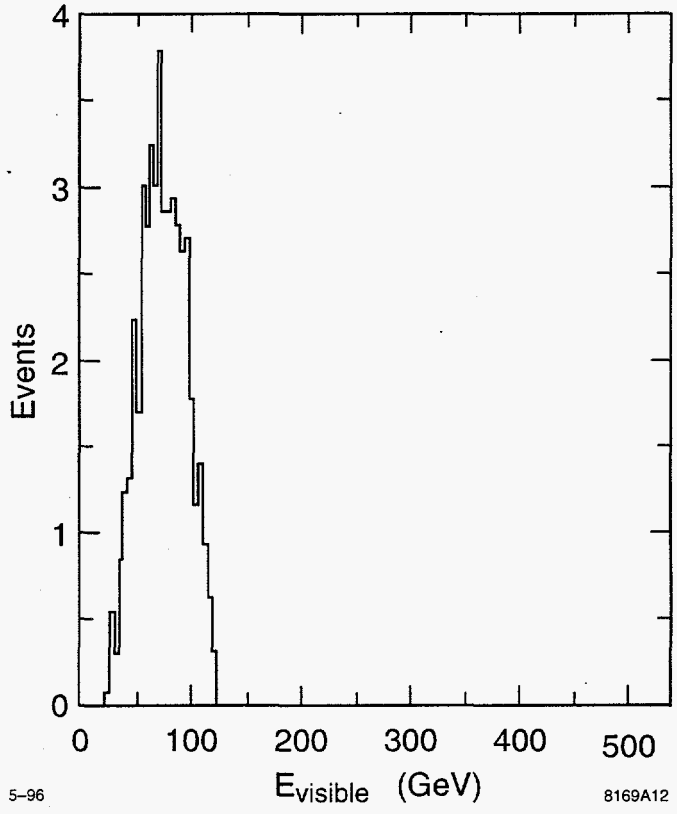

Figure 0.32: The visible energy distribution for the SUSY process $e^+e^- \rightarrow \chi_2^0\chi_1^0$ associated with parameter set 4 and the Standard Model background processes, after the cuts defined in the previous figure to enhance the signal over background.

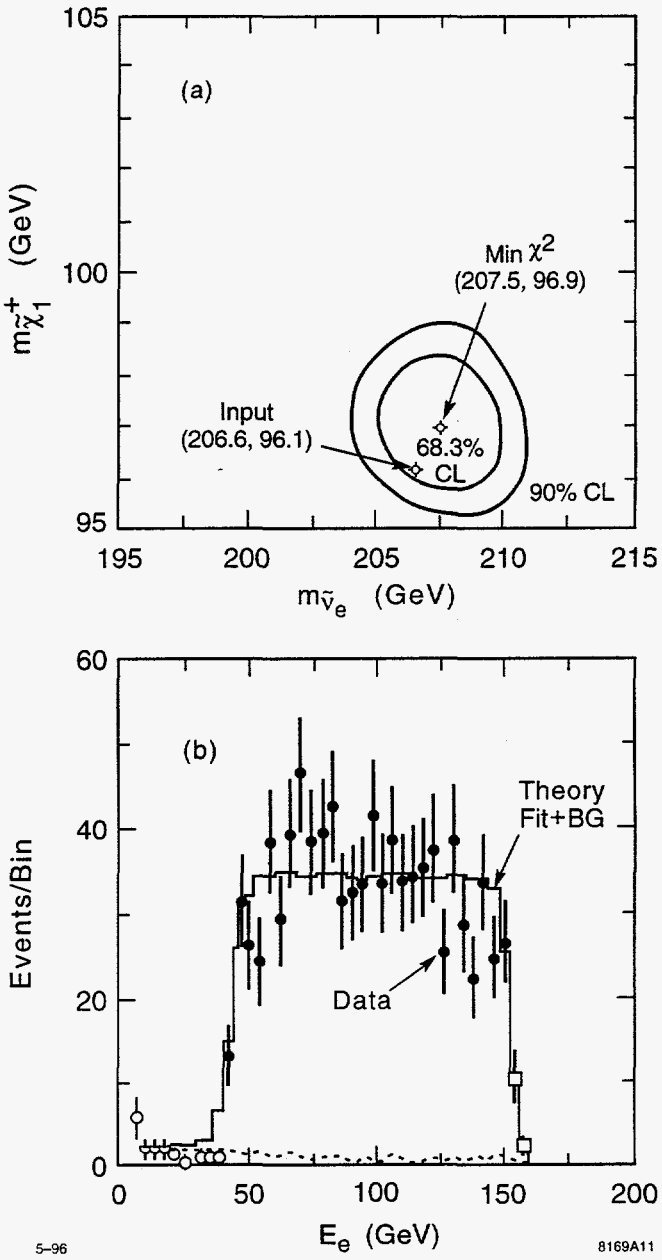

Figure 0.33: The electron energy distribution in the process $e^+e^- \to \tilde{\nu}_e\tilde{\nu}_e \to e^-\chi_1^+e^+\chi_1^- \to e^-\mu^{+-}\chi_1^0e^+\chi_1^0 + 2$ jets and the fit that determines the mass of the $\tilde{\nu}_e = 207.5 \pm 2.5$ GeV and the mass of the $\chi_1^+ = 97.0 \pm 1.2$ GeV at the 68% C.L.

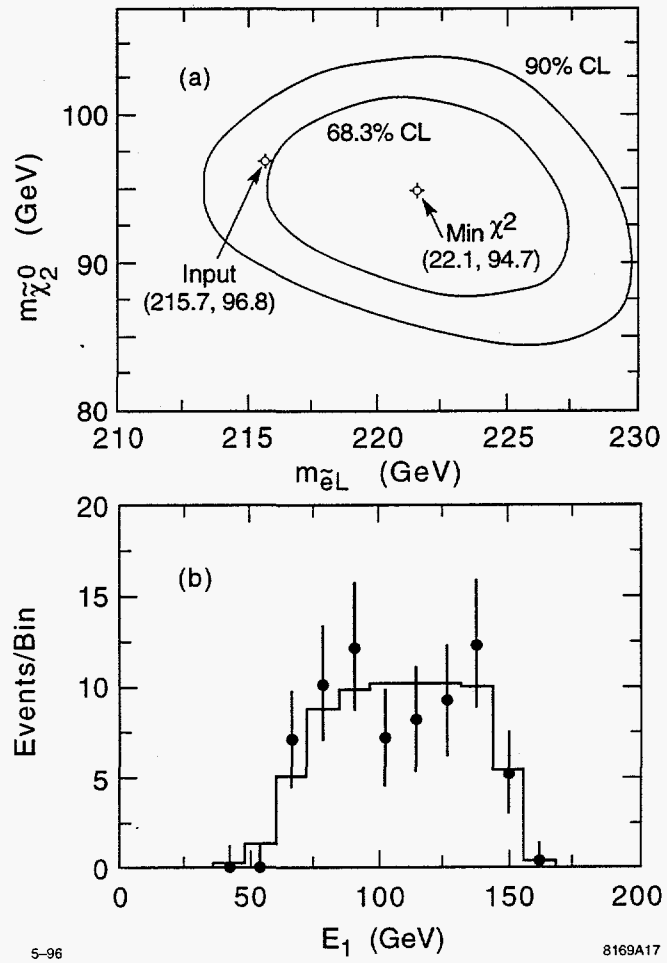

Figure 0.34: The energy distribution of the two highest energy leptons in the process $e^+e^- \rightarrow \tilde{\ell}_L^-\tilde{\ell}_L^+ \rightarrow \ell^-\tilde{\chi}_2^0\ell^+\tilde{\chi}_2^0 \rightarrow \ell^- Z^0\chi_1^0\ell^+ Z^0\chi_1^0 \rightarrow$ six leptons plus missing energy, and the fit that determines the mass of the $\tilde{\ell}_L$ and the χ_2^0. Only those events were considered in which the highest energy leptons were e^+e^- or $\mu^+\mu^-$. The fit gives the mass values $M_{\tilde{\ell}_L} = 221.6 \pm 5.6$ GeV and $M_{\tilde{\chi}_2^0} = 94.7 \pm 5.3$ GeV

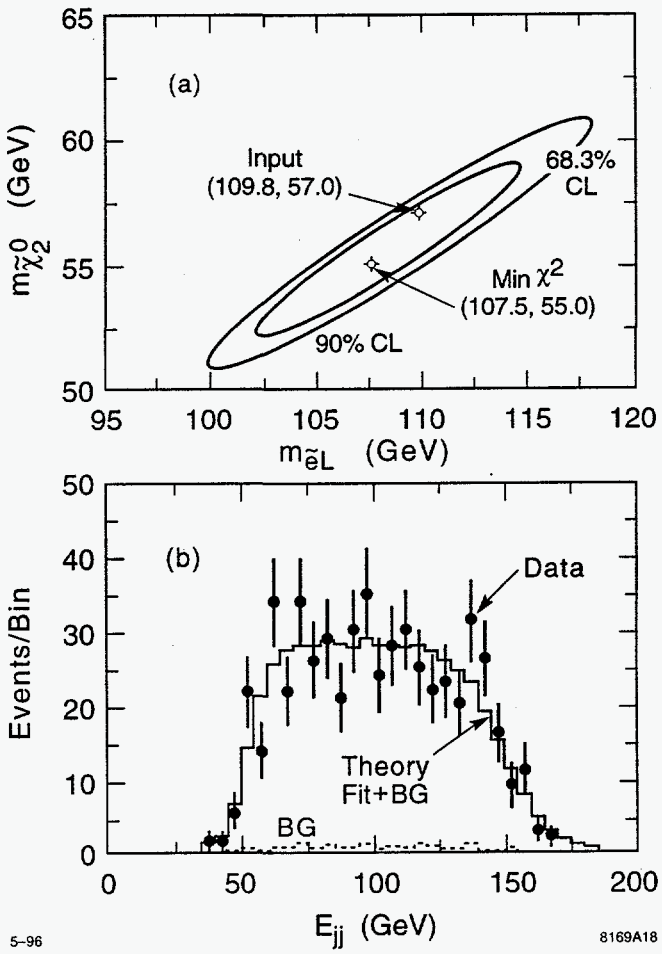

Figure 0.35: The quark pair energy distribution in the process $e^+e^- \to \tilde{\chi}_1^+\tilde{\chi}_1^- \to q\bar{q}\tilde{\chi}_1^0 q\bar{q}\tilde{\chi}_1^0$ and the fit to the $\tilde{\chi}_1^+$, $\tilde{\chi}_1^0$ masses. The fit gives the mass values $M_{\tilde{\chi}_1^+} = 107.5 \pm 6.5$ GeV and $M_{\tilde{\chi}_1^0} = 55.0 \pm 3.5$ GeV.

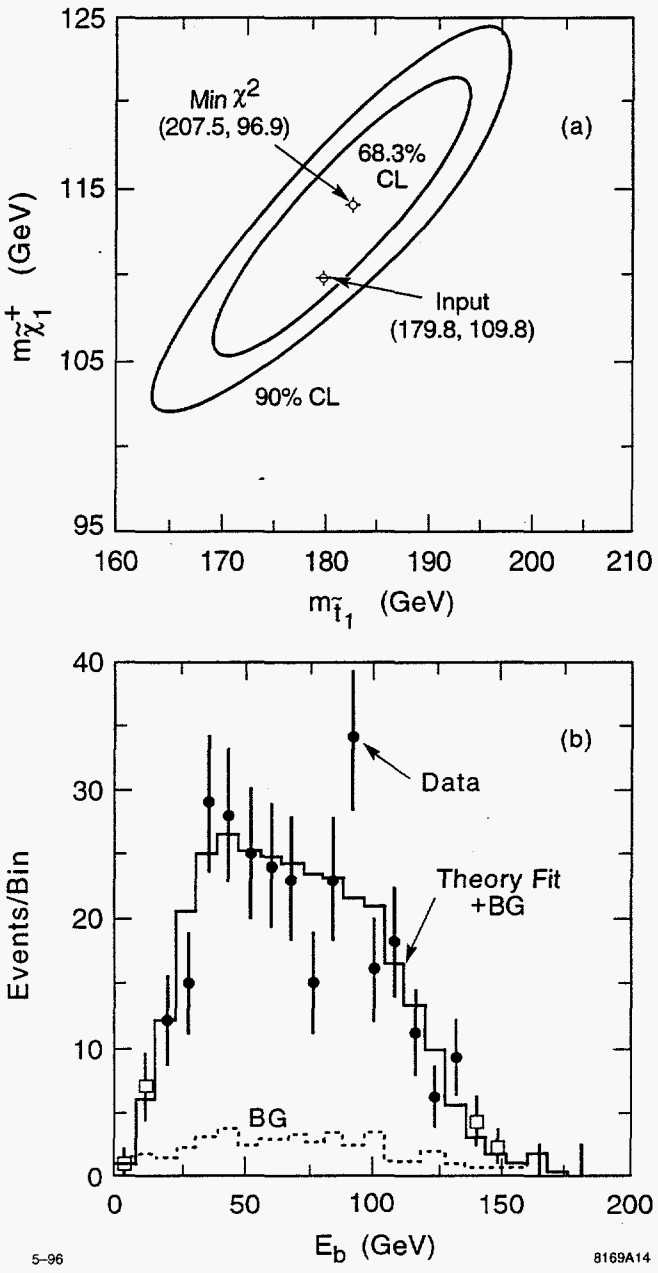

Figure 0.36: The b-jet energy distribution in the process $e^+e^- \to \tilde{t}_1\bar{\tilde{t}_1} \to b\tilde{\chi}_1^+\bar{b}\tilde{\chi}_1^-$ and the fit to the $\tilde{t}_1\tilde{\chi}_1^+$ masses. The fit gives the mass values $M_{\tilde{t}_1} = 182 \pm 11$GeV and $M_{\tilde{\chi}_1^+} = 114 \pm 8$ GeV.

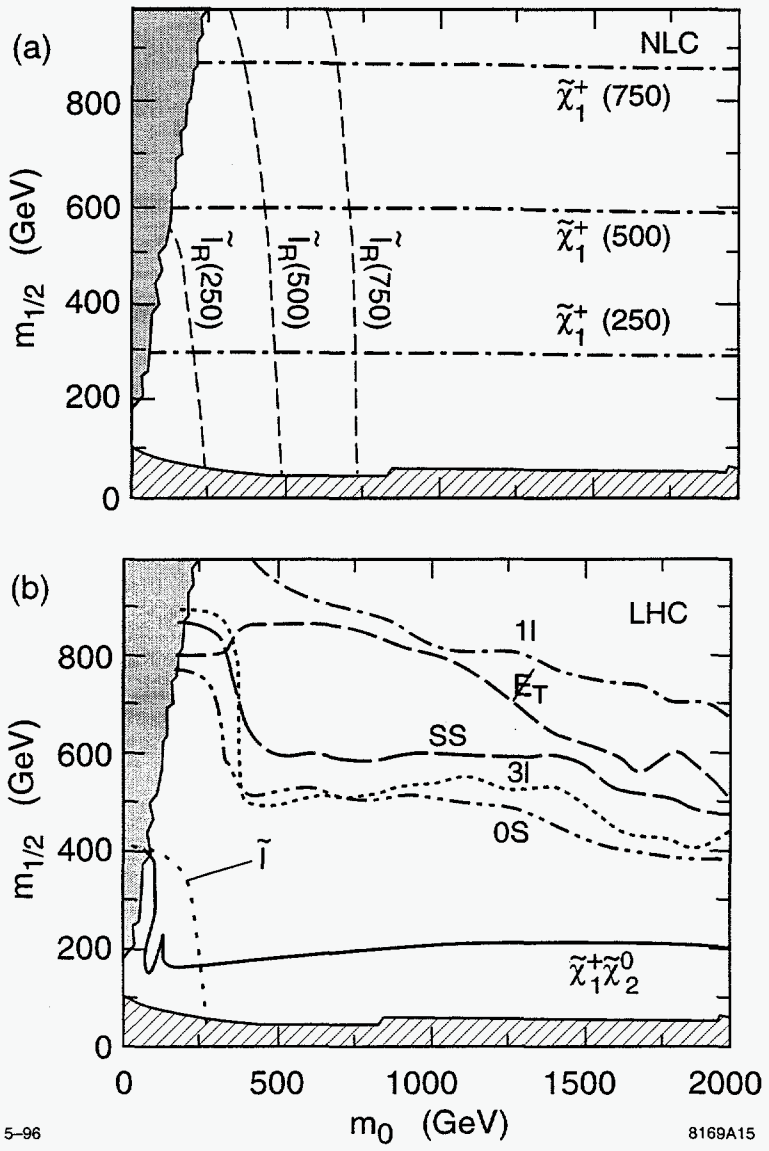

Figure 0.37: Comparison of the reach of the NLC(0.5 TeV), NLC(1.0), NLC(1.5) presented in the top figure, and the LHC assuming an integrated luminosity of 10 fb^{-1} in the bottom figure. The contours are labeled $\tilde{\ell}$ for the slepton reach, $\tilde{\chi}_1^+\tilde{\chi}_1^0$ for the $\tilde{\chi}_1^+\tilde{\chi}_1^0 \to 3\ell$ reach, 1ℓ for the reach via lepton + jets + $\not{E}_T$ events, $\not{E}_T$ for events with multi-jets + $\not{E}_T$, SS for same-sign dileptons + jets + $\not{E}_T$ and 3ℓ for trilepton + jets +$\not{E}_T$.

0.6 Anomalous Gauge Boson Couplings

Although the Standard Electroweak Model has been verified to astounding precision in recent years at LEP and SLC, one important component has not been tested directly with significant precision: the non-Abelian self couplings of the weak vector gauge bosons. Deviations of non-abelian couplings from expectation would signal new physics, perhaps arising from unexpected loop corrections involving propagators of new particles. In addition, as will be discussed in Chapter 8, precise measurements of WWV couplings, where $V = \gamma$ or Z, can provide important information on the nature of electroweak symmetry breaking. Recent results from CDF and D0 indicate the presence of triple gauge boson couplings, but have not yet reached a precision better than order unity [75]. Upcoming measurements at LEP II, at an upgraded Tevatron and at the LHC will improve upon this precision considerably, but cannot the match the expected precision of a 500 GeV NLC, much less that of a 1.0 or 1.5 TeV NLC. There exist indirect constraints on the anomalous couplings from the precision electroweak measurements at the Z^0 resonances, in particular, from the fact that loop diagrams involving weak vector bosons are seen to take the values expected in the standard model. However, the ambiguities in the calculation of these diagrams call for more direct measurements [76].

In this brief report we restrict attention mainly to measurement of possibly anomalous WWV couplings via the process $e^+e^- \to W^+W^-$, but much work has been done on other processes that involve non-abelian couplings in e^+e^- annihilation, including $ZZ\gamma$, $Z\gamma\gamma$, $WWZZ$, and $WWWW$ [75]. In addition, many of these couplings can also be measured independently using the e^-e^-, $e^-\gamma$ and $\gamma\gamma$ options for the NLC. We will describe one common parametrization of anomalous WWV couplings, summarize present and expected pre-NLC measurements of WWV couplings, and discuss in more detail what can be done at NLC.

0.6.1 Parametrization

In parametrizing anomalous couplings, we follow the notation of Ref. [7] in which the generic effective Lagrangian for the WWV vertex is written:

$$\begin{aligned} L_{WWV}/g_{WWV} \;=\; & i\,g_1^V(W^\dagger_{\mu\nu}W^\mu V^\nu - W^\dagger_\mu V_\nu W^{\mu\nu}) + i\,\kappa_V W^\dagger_\mu W_\nu V^{\mu\nu} + \frac{i\,\lambda_V}{M_W^2}W^\dagger_{\lambda\mu}W^\mu_\nu V^{\nu\lambda} \\ & -g_4^V W^\dagger_\mu W_\nu(\partial^\mu V^\nu + \partial^\nu V^\mu) + g_5^V\epsilon^{\mu\nu\rho\sigma}(W^\dagger_\mu \overleftrightarrow{\partial}_\rho W_\nu)V_\sigma + \tilde{\kappa}_V W^\dagger_\mu W_\nu \tilde{V}^{\mu\nu} \\ & +\frac{i\,\tilde{\lambda}_V}{M_W^2}W^\dagger_{\lambda\mu}W^\mu_\nu \tilde{V}^{\nu\lambda} \end{aligned}$$

where $W_{\mu\nu} \equiv \partial_\mu W_\nu - \partial_\nu W_\mu$, $V_{\mu\nu} \equiv \partial_\mu V_\nu - \partial_\nu V_\mu$, $(A\overleftrightarrow{\partial}_\mu B) \equiv A(\partial_\mu B) - (\partial_\mu A)B$, and $\tilde{V}_{\mu\nu} \equiv \frac{1}{2}\epsilon_{\mu\nu\rho\sigma}V^{\rho\sigma}$. The normalization factors are defined for convenience to be $g_{WW\gamma} \equiv -e$ and $g_{WWZ} \equiv -e\cot\theta_W$. The 7 coupling parameters defined in Eq. 0.11 for each of γ and Z include the C and P violating couplings g_5^V as well as the CP-violating couplings $g_4^V, \tilde{\kappa}_V, \tilde{\lambda}_V$. In most studies and in this one, such terms are neglected. In the standard model $g_1^V = \kappa_V = 1$

and $\lambda_V = g_4^V = g_5^V = \tilde{\kappa}_V = \tilde{\lambda}_V = 0$. The couplings in Eq. 0.11 should properly be written as form factors with momentum-dependent values. This complication is of little importance at an e^+e^- collider where the WW center of mass energy is well defined, but it must be borne in mind at hadron colliders where couplings are simultaneously probed over large energy ranges.

We follow the common convention in defining $\Delta g_1^Z \equiv g_1^Z - 1$ and $\Delta\kappa_V \equiv \kappa_V - 1$. The W electric charge fixes $g_1^\gamma(q^2 \to 0) \equiv 1$. In perhaps more familiar notation, one can express the W magnetic dipole moment as $\mu_W \equiv \frac{e}{2M_W}(1 + \kappa_\gamma + \lambda_\gamma)$ and the W electric quadrupole moment as $Q_W \equiv -\frac{e}{M_W^2}(\kappa_\gamma - \lambda_\gamma)$.

In any model with new physics at high energy that couples to the W boson, the anomalous couplings will be induced at some level. A useful way to represent this effect is to write an $SU(2) \times U(1)$-invariant effective Lagrangian to represent the effects of the new physics, and then to couple this to the weak vector bosons by gauging the symmetry. In the literature, this has been done using both linear and nonlinear effective Lagrangians [76]. Typically, the anomalous couplings predicted in such models are suppressed by factors of M_W^2/Λ^2, where Λ is a multi-TeV scale [77], or by factors $\alpha_w/4\pi$. These lead to typical values of the anomalous couplings below 10^{-2} and make it difficult to observe these couplings before directly observing the new physics itself.

For the present discussion, we will restrict the parameter space further by imposing a custodial $SU(2)$ symmetry on the effective Lagrangian in its linear realization. This leads to the 'HISZ Scenario' [79] which involves only two free parameters which we will take to be κ_γ and λ_γ. This restriction of the parameter space has recently been applied to comparative studies of the anomalous W couplings at colliders [75]. It is important to note, however, that studies of $e^+e^- \to W^+W^-$ at the NLC can also test this hypothesis by independently determining the γ and Z couplings to the W [82].

0.6.2 Present and Expected Pre-NLC Measurements

The only present direct measurements of WWV couplings come from the CDF and D0 Experiments [75] at the Tevatron, which have searched for WW, WZ, and $W\gamma$ production. The WW and WZ searches have yielded $O(1)$ candidates and the $W\gamma$ searches have yielded $O(10)$ candidates, consistent with expectation. These observations have led to limits on coupling parameters of order unity. For example, D0 sets a 95% CL range $-1.8 < \Delta\kappa_\gamma < 1.9$ assuming $\lambda_\gamma = 0$ or a range $-0.6 < \lambda_\gamma < 0.6$ assuming $\kappa_\gamma = 0$ (both limits assume $\Lambda = 1$ TeV in the appropriate form factors).

One expects significant improvement at LEP II [80], once the accelerator exceeds the W-pair threshold energy. Techniques similar to those described below will be applied to $e^+e^- \to W^+W^-$ events at c.m. energies ranging from threshold at $\approx$160 GeV to $\approx$195 GeV. Assuming no anomalous couplings are observed after an integrated luminosity of 500 pb^{-1}, 95% CL limits on individual couplings (all others set to zero) of $O(0.1)$ are expected.

After the Main Injector upgrade has been completed, it is expected that the Tevatron

will collect O(1-10) fb^{-1} of data. (Further upgrades in luminosity are also under discussion.) If 10 fb^{-1} is achieved, it is expected [75] that limits on $\Delta\kappa_\gamma$ and λ_γ will be obtained that are competitive with those from LEP II with 500 pb^{-1}.

Finally, one expects the LHC accelerator to turn on sometime before the NLC and to look for the same signatures considered at the Tevatron. The planned luminosity and c.m. energy, however, give the LHC a large advantage over even the Main Injector Tevatron in probing anomalous couplings. The ATLAS Collaboration has estimated [24] that with 100 fb^{-1}, one can obtain (in the HISZ scenario) 95% CL limits on $\Delta\kappa_\gamma$ and λ_γ in the range 5-10 $\times$ 10^{-3}. We should note that these studies do not yet include helicity analysis on the W bosons, which may all some further improvement.

0.6.3 Measurements in W Pair Production at the NLC

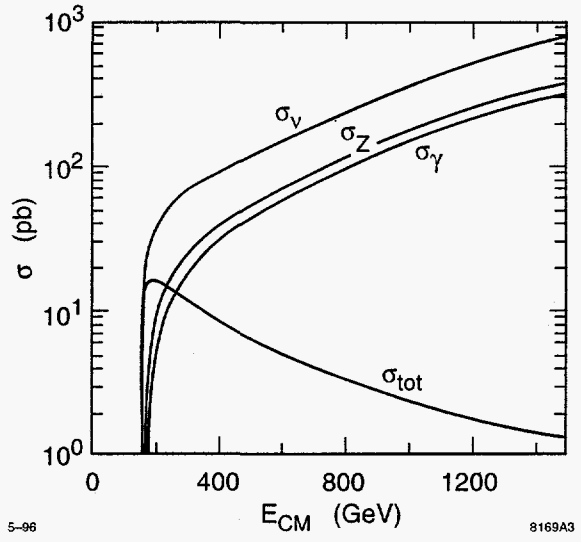

Figure 0.38: Total cross sections *vs* c.m. energy for t-channel ν_e exchange and s-channel γ and Z annihilation diagrams, along with their sum, as expected in the Standard Model with no anomalous couplings.

The fact that expected LHC limits improve dramatically upon those of even a high-luminosity Tevatron indicates the importance of c.m. energy. This can be understood as a consequence of delicate cancellations of large amplitudes that grow with energy. Figure 0.38 shows separately the total cross sections vs c.m. energy from t-channel ν_e exchange and s-channel γ and Z annihilation diagrams, along with their sum, including interference terms, as expected in the Standard Model (no anomalous couplings). At high energies, one expects even tiny modifications of one or more of the underlying amplitudes to spoil the delicate cancellations, leading to a measurable effect.

The NLC has an added advantage over hadron colliders in reconstructing W pair events

due to absence of spectator partons. To a good approximation, full energy and momentum conservation constraints can be applied to the visible final states. Thus an $e^+e^- \to W^+W^-$ event can ideally be characterized by five angles: the production angle $\Theta - W$ of the W^- w.r.t. the electron beam, the polar and azimuthal decay angles θ^* and ϕ^* of one daughter of the W^- in the W^- reference frame, and the corresponding decay angles $\overline{\theta}^*$ and $\overline{\phi}^*$ of a W^+ daughter. In practice, initial-state photon radiation and final-state photon and gluon radiation (in hadronic W decays) complicate the picture. So does the finite width of the W. Nevertheless, for the studies below, we will characterize $e^+e^- \to W^+W^-$ events by these five angles and fit distributions in the angles to obtain values of anomalous couplings.

At high energies, the $e^+e^- \to W^+W^-$ process is dominated by t-channel ν_e exchange, leading primarily to very forward-angle W's where the W^- has an average helicity near minus one. This makes the bulk of the cross section difficult to observe with precision. However, the amplitudes affected by the anomalous couplings are not forward peaked; the central and backward-scattered W's are measurably altered in number and helicity by the couplings. W helicity analysis through the decay angular distributions provides a powerful probe of anomalous contributions. Most studies, including those discussed here, restrict attention to events for which $|\cos\Theta - W| < 0.8$. Not surprisingly, the most powerful channel to use is one in which one W decays leptonically (to $e\nu$ or $\mu\nu$) and the other hadronically ($\approx 30\%$ of all $e^+e^- \to W^+W^-$ events) Although one gains statistics when both W's decay hadronically, one loses considerable discriminating power from being unable to purely tag the charge of the W daughter quarks. The channel in which both W's decay leptonically suffers from both poor statistics and kinematic ambiguities due to two undetected neutrinos. For the leptonic *vs* hadronic channel, the lepton energy carries important information for kinematic reconstruction. For simplicity, most studies have not yet attempted to incorporate $W \to \tau\nu$ decays.

Figure 0.39 (taken from Ref. [81]) shows 95% CL exclusion contours in the plane λ_γ *vs* $\Delta\kappa_\gamma$ in the HISZ scenario for different c.m. energies and integrated luminosities (0.5 fb^{-1} at 190 GeV, 80 fb^{-1} at 500 GeV, and 190 fb^{-1} at 1500 GeV). These contours are based on ideal reconstruction of W daughter pairs produced on mass-shell with no initial-state radiation. The contours represent the best one can do. A previous study [82] assuming a very high-performance detector but including initial-state radiation and a finite W width found some degradation in these contours, primarily due to efficiency loss when imposing kinematic requirements to suppress events far off mass-shell or at low effective c.m. energies. Nevertheless, one attains a precision of $O(10^{-3})$ at NLC(500) and $O(\text{few } \times 10^{-4})$ at NLC(1500). Another nice feature of couplings studies at NLC is the ability to disentangle couplings in models more general than HISZ via tuning of the electron beam polarization [82].

A study [83] undertaken for this workshop has examined the effects of detector resolution on achievable precisions. One might expect *a priori* that the charged track momentum resolution would be most critical since the energy spectrum for the W-daughter muons peaks at a value just below the beam energy, falling off nearly linearly with decreasing energy. One might also expect the hadron calorimeter energy resolution to be important in that it affects

the energy resolution of jets to be identified with underlying W-daughter quarks. Preliminary work indicates, however, that an NLC detector can tolerate a broad range in charged track momentum and hadron calorimeter energy resolutions without significant degradation of precision on extracted anomalous couplings. This insensitivity to detector resolutions stems from the power of an over-constrained kinematic fit in determining the five event angles.

In summary, this study and the previous study [82] including effects of initial-state radiation and finite W width confirm the power of the NLC to extract anomalous couplings. We expect some degradation in coupling parameters precision from the ideal case due to the underlying physical phenomena of initial state photon radiation and the finite W width and a smaller degradation from the imperfection of matching detected particles to primary W daughters, but these effects are not serious and should be straightforward to incorporate in a real measurement.

0.6.4 Measurements in Other Reactions at the NLC

In addition, an NLC e^+e^- collider allows measurement of non-abelian gauge boson couplings in other channels [75]. The process $e^+e^- \to Z\gamma$ probes $ZZ\gamma$ and $Z\gamma\gamma$ couplings, and processes such as $e^+e^- \to WWZ$ probe quartic couplings. The $WW\gamma$ and WWZ couplings can be probed independently via the processes $e^+e^- \to \nu\overline{\nu}\gamma$ and $e^+e^- \to \nu\overline{\nu}Z$, respectively.

Similar measurements can be carried out at e^-e^-, $e^-\gamma$ and $\gamma\gamma$ colliders, where the expected reduction in luminosity is at least partly compensated by other advantages [82, 84]. For example, the process $\gamma e^- \to W^-\nu_e$ probes the $WW\gamma$ coupling, independent of WWZ effects. The polarization asymmetry in this reaction reverses the the energy the collisions is varied, and the location of this zero-crossing provides a sensitive probe of λ_γ [85]. The reaction $\gamma\gamma \to W^+W^-$ also separates effects of the γ couplings from those of the Z, and also probes the possible 4-boson $WW\gamma\gamma$ vertex. The power of this facility is enhanced by its ability to polarize both incoming beams.

0.6.5 Conclusions

Although there will have been a number of measurements of anomalous coupling parameters from LEP II, the Tevatron, and the LHC before the turn-on of NLC, the precisions on couplings attainable with the NLC will quickly overwhelm the previous measurements. Moreover, the higher the accessible energy at NLC, the more dramatic the improvement will be. Figure 0.40 (taken from Ref. [86]) shows a useful comparison among these accelerators. The enormous potential of NLC is apparent.

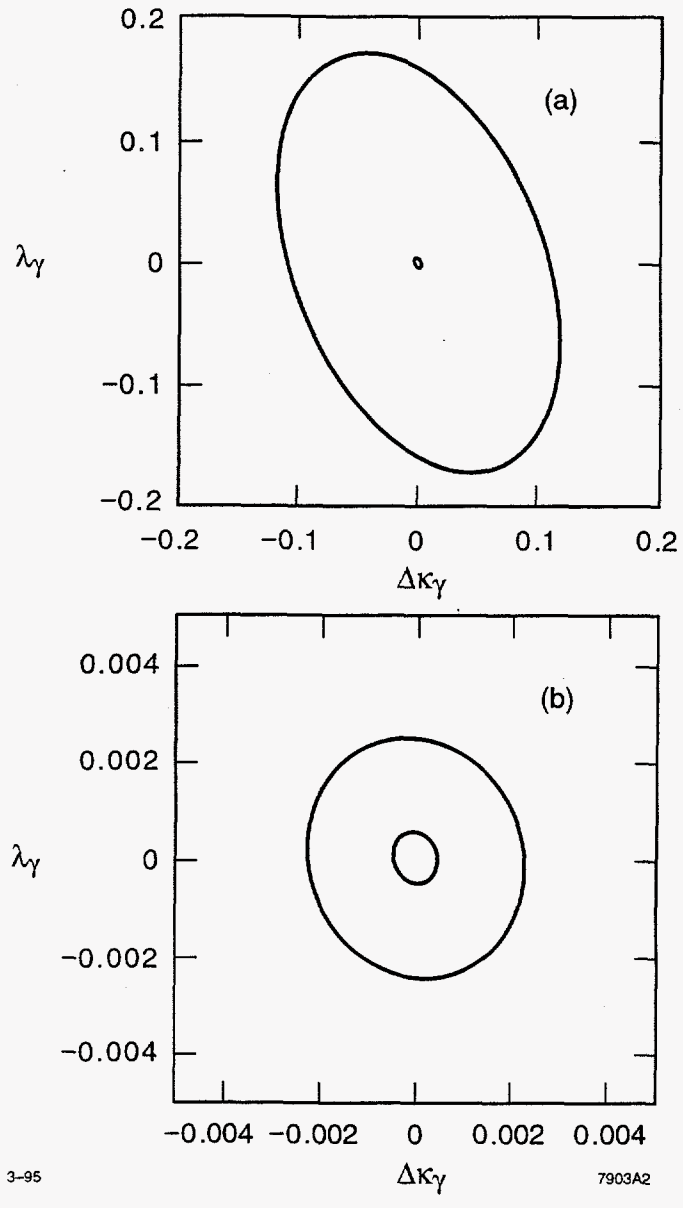

Figure 0.39: 95% CL contours for $\Delta\kappa_\gamma$ and λ_γ in the HISZ scenario. The outer contour in (a) is for $E_{CM} = 190$ GeV and 0.5 fb^{-1}. The inner contour in (a) and the outer contour in (b) is for $E_{CM} = 500$ GeV with 80 fb^{-1}. The inner contour in (b) is for $E_{CM} = 1.5$ TeV with 190 fb^{-1}.

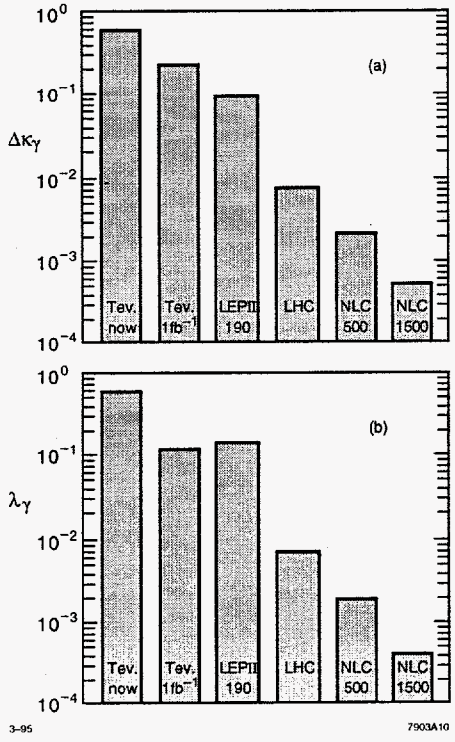

Figure 0.40: Comparison of representative 95% CL upper limits on $\Delta\kappa_\gamma$ and λ_γ for present and future accelerators.

0.7 Strong WW Scattering

In this section we examine how well an e^+e^- linear collider with a center-of-mass energy of 500–1500 GeV can study a strongly interacting Higgs sector. We also compare the estimated sensitivity of such a collider with that of the LHC.

0.7.1 The Reaction $e^+e^- \to W^+W^-$

Strong electroweak symmetry breaking affects the reaction $e^+e^- \to W^+W^-$ through anomalous couplings at the $W^+W^-\gamma$ and W^+W^-Z vertices and through enhancements in $W_L^+W_L^-$ production due to $I = J = 1$ resonances. Here we have used the symbol W_L to denote a longitudinally polarized W boson. Anomalous couplings at the three-gauge boson vertices are related to the chiral Lagrangian parameters L_{9L} and L_{9R} [77]. A technipion form factor F_T is used to parameterize [87] the strong $W_L^+W_L^-$ interaction in the $I = J = 1$ state; it is analogous to the rho–dominated pion form factor in $e^+e^- \to \pi^+\pi^-$.

Whether one is measuring trilinear vector boson couplings or searching for an enhancement in $W_L^+W_L^-$ production, the experimental goal is the same: disentangle the W^+W^- polarization states, and in particular isolate the polarization state $W_L^+W_L^-$. We shall describe the results of a study that utilizes a final-state helicity analysis of all observable final-state variables in order to isolate $W_L^+W_L^-$ production [6].

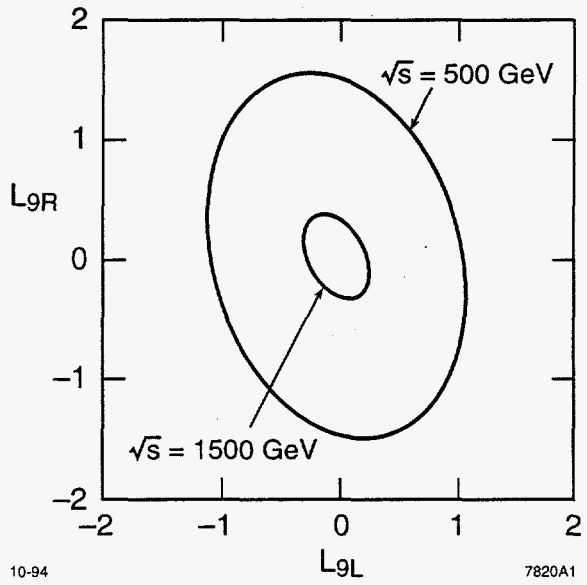

Figure 0.41: The 95% confidence level contours for L_{9L} and L_{9R} at $\sqrt{s} = 500$ GeV with 80 fb^{-1}, and at $\sqrt{s} = 1500$ GeV with 190 fb^{-1}. The outer contour is for $\sqrt{s} = 500$ GeV. In each case the initial state electron polarization is 90%.

The maximum likelihood method is used to fit for chiral Lagrangian parameters or for the real and imaginary parts of the technipion form factor. Figure 0.41 shows the 95% confidence level contours for the chiral Lagrangian parameters L_{9L} and L_{9R} at $\sqrt{s} = 500$ GeV and at $\sqrt{s} = 1500$ GeV. The parameters L_{9L} and L_{9R} are normalized such that values of $\mathcal{O}(1)$ are expected if the Higgs sector is strongly interacting.

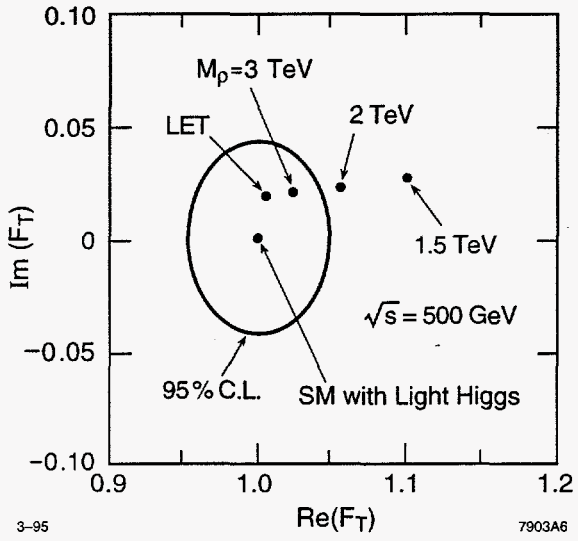

Figure 0.42: 95% confidence level contours for the real and imaginary parts of F_T at $\sqrt{s} = 500$ GeV with 80 fb^{-1}. The values of F_T for various technirho masses are indicated.

Figure 0.42 shows the 95% confidence level contour for the real and imaginary parts of F_T at $\sqrt{s} = 500$ GeV. Also indicated are values of F_T for various technirho masses. The infinite technirho mass point is labelled Low Energy Theorem (LET) since in this limit there is residual $W_L^+ W_L^-$ scattering described by the same low energy theorems that govern low energy $\pi^+\pi^-$ scattering. We see that the NLC at $\sqrt{s} = 500$ GeV can exclude technirho masses up to about 2.5 TeV and can discover technirho resonances with masses of more than 1.5 TeV. The significance of the 1.5 TeV technirho signal would be 6.7σ. A 1.0 TeV technirho would produce a 17.7σ signal. For comparison, the minimal technicolor model predicts a technirho mass of about 2.0 TeV.

Figure 0.43 contains confidence level contours for the real and imaginary parts of F_T at $\sqrt{s} = 1500$ GeV. The non-resonant LET point is well outside the light Higgs 95% confidence level region and corresponds to a 4.5σ signal. The labeling of points here deserves some comment. We use the model of [87] to describe the form factor F_T. In this model, as the vector resonance mass is taken to infinity, its effect on the form factor decreases, and what is left behind is the residual scattering predicted by the LET. The values for high-mass technirho indicate this decoupling. With this understanding, the 6 TeV, 4 TeV and and 3 TeV technirho points correspond to 4.8σ, 6.5σ, and 11σ signals, respectively. A 2 TeV technirho would produce a 37σ signal.

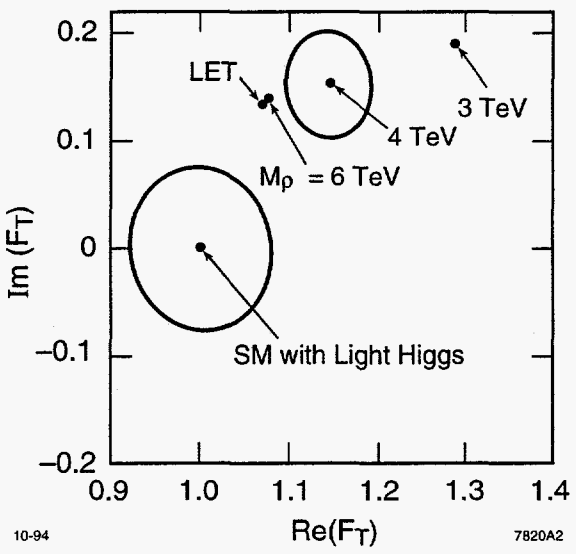

Figure 0.43: Confidence level contours for the real and imaginary parts of F_T at $\sqrt{s} = 1500$ GeV with 190 fb^{-1}. The contour about the light Higgs value of $F_T = (1, 0)$ is 95% confidence level and the contour about the $M_\rho = 4$ TeV point is 68% confidence level.

It might appear that the value of F_T, and hence the significance of technirho signals, would be very sensitive to the technirho width when $\sqrt{s}$ is much less than the technirho mass. In the model we have considered, however, this is not true. The results presented above were obtained assuming that $\Gamma_\rho/M_\rho = 0.22$. If, for example, the technirho width is reduced to $\Gamma_\rho/M_\rho = 0.03$ then the 1 TeV signal at $\sqrt{s} = 500$ GeV is reduced from 17.7σ to 16.3σ, the 1.5 TeV signal at $\sqrt{s} = 500$ GeV is reduced from 6.7σ to 6.4σ, and the 4 TeV signal at $\sqrt{s} = 1500$ GeV is reduced from 6.5σ to 6.3σ.

0.7.2 The Reaction $e^+e^- \to \nu\bar{\nu}W^+W^-$ and $\nu\bar{\nu}ZZ$

The important gauge boson scattering processes $W_L^+W_L^- \to W_L^+W_L^-$ and $W_L^+W_L^- \to Z_LZ_L$ are studied at the NLC with the reactions $e^+e^- \to \nu\bar{\nu}W^+W^-$ and $e^+e^- \to \nu\bar{\nu}ZZ$. We describe the results that Barger *et al.* [88] have obtained by analyzing these processes.

Barger *et al.* use several models to test the effectiveness of their analysis of $e^+e^- \to \nu\bar{\nu}W^+W^-$ and $\nu\bar{\nu}ZZ$. In addition to the Standard Model Higgs boson with mass $m_H = 1$ TeV, they use a Chirally–Coupled Scalar (CCS) model, a Chirally–Coupled Vector (CCV) model, and the LET model. They utilize a series of cuts to produce an event sample that is rich in the final states $\nu\bar{\nu}W_L^+W_L^-$ and $\nu\bar{\nu}Z_LZ_L$. Figure 0.44 shows the M_{WW} and M_{ZZ} distributions after all cuts. The 1 TeV Higgs scalar resonance stands out in both the $\nu\bar{\nu}WW$ and $\nu\bar{\nu}ZZ$ final states. The 1 TeV vector resonance is prominent in the M_{WW} distribution (of course such a resonance would have been seen earlier as a 16σ signal at $\sqrt{s} = 0.5$ TeV, in $e^+e^- \to W^+W^-$). The LET signal is larger for the final state $\nu\bar{\nu}ZZ$ than it is for $\nu\bar{\nu}WW$.

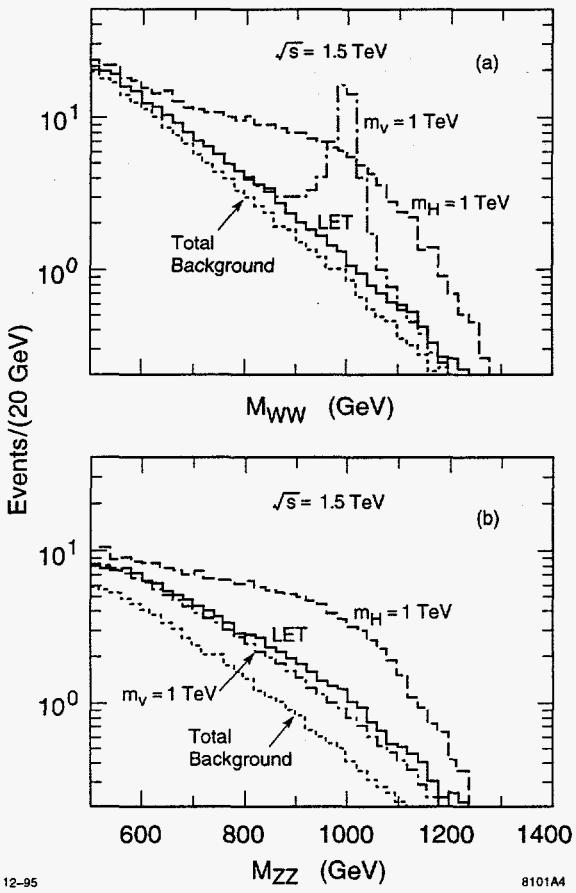

Figure 0.44: Expected numbers of W^+W^-, $ZZ \to (jj)(jj)$ signal and background events after all cuts for 200 fb^{-1} luminosity at $\sqrt{s} = 1.5$ TeV: (a) $e^+e^- \to \nu\bar{\nu}W^+W^-$, (b) $e^+e^- \to \nu\bar{\nu}ZZ$. The dotted histogram shows total SM background. The solid, dashed and dot–dashed histograms show signal plus background for the LET, SM, and CCV models, respectively; CCS model results are close to the SM case.

The statistical significance of the signals for the different models is given in Table 0.8 assuming 100% initial-state e^- polarization at $\sqrt{s} = 1.5$ TeV and $200 fb^{-1}$ luminosity. Note that the statistical significance of the LET signal is 8.5σ in the $\nu\bar{\nu}ZZ$ channel.

The $I = 2$ Goldstone boson scattering channel can be probed at the NLC through the reaction $e^+e^- \to \nu\nu W^-W^-$. Barger *et al.* [89] have studied this reaction and they obtain the statistical significances shown in Table 0.9. An initial state electron polarization of 100% has been assumed for both beams.

Table 0.8: Signal and background for $e^+e^- \to \nu\bar{\nu}W^+W^-$ and $e^+e^-\nu\bar{\nu}ZZ$ with 100% initial state electron polarization.

Signal (S) or Background (B)	SM $M_H = 1$ TeV	Scalar $M_S = 1$ TeV	Vector $M_V = 1$ TeV	LET
$S(e^+e^- \to \nu\bar{\nu}W^+W^-)$	330	320	92	62
B(backgrounds)	280	280	7.1	280
$S/\sqrt{B}$	20	20	35	3.7
$S(e^+e^- \to \nu\bar{\nu}ZZ)$	240	260	72	90
B(backgrounds)	110	110	110	110
$S/\sqrt{B}$	23	25	6.8	8.5

Table 0.9: Signal and background for $e^+e^- \to \nu\bar{\nu}W^-W^-$ with 100% initial state electron polarization.

Signal (S) or Background (B)	SM $M_H = 1$ TeV	Scalar $M_S = 1$ TeV	Vector $M_V = 1$ TeV	LET
$S(e^+e^- \to \nu\bar{\nu}W^-W^-)$	110	140	140	170
B(backgrounds)	710	710	710	710
$S/\sqrt{B}$	4.0	5.2	5.4	6.3

0.7.3 The Reaction $e^+e^- \to \nu\bar{\nu}t\bar{t}$

If there is no light Higgs boson, the process $t\bar{t} \to W^+W^-$ violates unitarity in the multi-TeV energy region. It is natural then to ask if strong symmetry breaking can be detected through the process $W^+W^- \to t\bar{t}$. This process would be studied at the NLC by observing the reaction $e^+e^- \to \nu\bar{\nu}t\bar{t}$.

The total cross sections for $e^+e^- \to e^+e^-t\bar{t}$ and $e^+e^- \to \nu\bar{\nu}t\bar{t}$ have been calculated by Kauffman [90] for an e^+e^- center-of-mass energy of 2 TeV (Fig. 0.45). The cross sections for $\sqrt{s} = 1.5$ TeV should be similar. For $\sqrt{s} = 2$ TeV and $200fb^{-1}$ luminosity we would have 1200 events from $e^+e^- \to e^+e^-t\bar{t}$ and 60 (400) events from $e^+e^- \to \nu\bar{\nu}t\bar{t}$ for $m_H =$ 0.1 (1.0) TeV. A 1 TeV Higgs boson therefore produces a 30% increase in the sum of the cross sections for $e^+e^- \to e^+e^-t\bar{t}$ and $e^+e^- \to \nu\bar{\nu}t\bar{t}$ before any cuts are applied. The same 1 TeV Higgs boson produces only a 0.3% increase in the sum of the cross sections for $e^+e^- \to e^+e^-W^+W^-$ and $e^+e^- \to \nu\bar{\nu}W^+W^-$.

The strong symmetry breaking signal can be further enhanced by performing a helicity

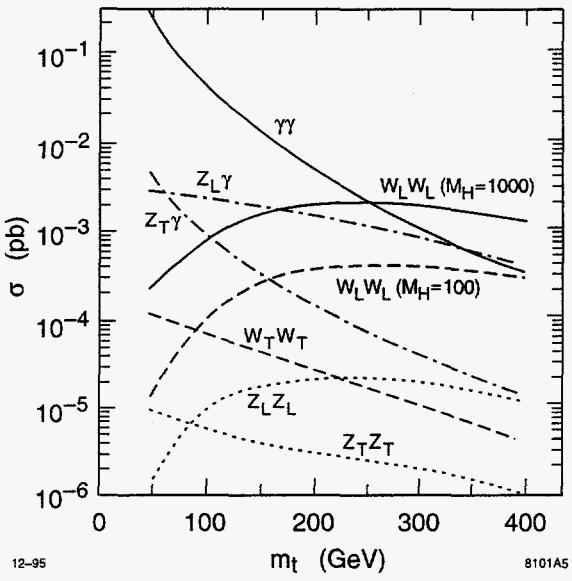

Figure 0.45: Contributions from various subprocesses to the total cross sections for $e^+e^- \to e^+e^-t\bar{t}$ and $e^+e^- \to \nu\bar{\nu}t\bar{t}$. The contributions are plotted as a function of the top quark mass m_t. The e^+e^- center-of-mass energy is 2 TeV.

analysis on the $t\bar{t}$ final state to isolate the polarization states $t_L\bar{t}_L$ and $t_R\bar{t}_R$ corresponding to helicity-flip pair production. Projecting out these helicity combinations would be the analog of projecting out the $W_L^+W_L^-$ and Z_LZ_L final states in gauge boson scattering.

0.7.4 Statistical significances at LHC versus NLC

The statistical significances of strong symmetry breaking signals at the NLC and LHC are summarized in Table 0.10. The LHC results are taken from the ATLAS design report [24]. If an entry is blank it may mean that the process is insensitive to the corresponding model or that the analysis has not been done; no distinction is made between the two possibilities. The entries for the direct gauge boson scattering processes at the NLC ($W^+W^- \to ZZ$ and $W^-W^- \to W^-W^-$) assume that the electron beam always has 90% left–handed polarization. For both the NLC and LHC results it was assumed that the 1.5 TeV technirho had a width of 0.33 TeV.

Some points about Table 0.10 are worth noting:

1. Although the LHC can access larger W^+W^- center-of-mass energies, the statistical significance of the NLC signal is always larger. In most cases, this is a small effect, but it makes an significant point: Electron beam polarization, smaller backgrounds, and the utilization of the full e^+e^- center-of-mass energy for vector resonances has allowed the NLC to more than make up for its lower range of W^+W^- center-of-mass energies.

Table 0.10: Statistical significances of strong symmetry breaking signals at the NLC and LHC.

Collider	Process	$\sqrt{s}$ (TeV)	$\mathcal{L}$ (fb^{-1})	$M_\rho =$ 1.5 TeV	$M_H =$ 1 TeV	LET
NLC	$e^+e^- \to W^+W^-$	.5	80	7σ	–	–
NLC	$e^+e^- \to W^+W^-$	1.0	200	35σ	–	–
NLC	$e^+e^- \to W^+W^-$	1.5	190	366σ	–	5σ
NLC	$W^+W^- \to ZZ$	1.5	190	–	22σ	8σ
NLC	$W^-W^- \to W^-W^-$	1.5	190	–	4σ	6σ
LHC	$W^+W^- \to W^+W^-$	14	100	–	14σ	–
LHC	$W^+W^+ \to W^+W^+$	14	100	–	3σ	6σ
LHC	$W^+Z \to W^+Z$	14	100	7σ	–	–

2. The NLC has a special ability to detect vector resonances. At $\sqrt{s} = 500$ GeV the technirho mass reach of the NLC is equal to that of the LHC. At $\sqrt{s} = 1500$ GeV the NLC is sensitive to strong interaction effects in $I = J = 1$ W^+W^- scattering even when they are nonresonant.

3. Signal significances for $W^+W^- \to t\bar{t}$ were not included in Table 0.10 because detector simulations have not yet been performed. From the discussion in Section 0.7.3, however, it appears that this is a promising reaction for the study of strong symmetry breaking at the NLC. It is probably very difficult to study $W^+W^- \to t\bar{t}$ at LHC due to the large background from $gg \to t\bar{t}$.

Finally it is important to remember that the significances shown in Table 0.10 include statistical errors only. Systematic errors have largely been ignored in analyses so far, both for the LHC and for the NLC.

0.7.5 Conclusion

An e^+e^- linear collider with $\sqrt{s} = 500 - 1500$ GeV would be an effective partner to the LHC in the study of strong symmetry breaking. It provides important complementary capabilities for the discovery of vector resonances and the extraction of chiral Lagrangian parameters. The NLC and LHC are expected to have similar statistical errors for scalar resonance and non–resonant signals in gauge boson scattering; however, the physics environments at the two machines are very different, and the systematic errors for the NLC analyses are probably smaller. The NLC is probably the only machine that can study $W^+W^- \to t\bar{t}$.

0.8 New Gauge Bosons and Exotic Particles

In many extensions to the Standard Model, in particular those involving an enlargement of the $SU(3)_c \times SU(2)_L \times U(1)_Y$ gauge group or compositeness, new particles are expected to exist beyond those associated with either supersymmetry or technicolor. The properties and signatures of exotic particles have recently been reviewed in [91] In almost all cases, these particles can be directly produced and have their properties analyzed in e^+e^- collisions given a sufficiently large center-of-mass energy. If such energies are not available, the indirect influence of the existence of many kinds of exotic particles can also be examined through precision measurements at the NLC.

Perhaps the most well-studied of all exotic particles is the new neutral gauge boson, Z', which is a basic ingredient of all theories with extended gauge sectors. (When the additional group factor is non-abelian, new charged gauge bosons, W', may also be present.) If such a particle exists and is accessible at the TeV scale, it is possible that it may first be directly produced via the Drell-Yan process at the LHC, provided the Z' couples to *both* quarks and leptons as it does in most models. If the Z' does not couple to leptons it cannot be produced at the NLC; in this case, searches at the LHC would also be difficult, since the effects of the Z' would have to be observed as perturbations of di-jet mass distributions. If the Z' couples only to leptons, then the NLC provides the unique means to study it.

It is possible that a Z', though it exists, may not be seen at the LHC due to its mass and/or the nature of its couplings to fermions. In this case the NLC can extend the search reach for some models; in addition the NLC may be able to determine both the mass and couplings of the Z'. A 'lucky' scenario would be one where the mass of the Z' is less than the NLC $\sqrt{s}$; in this case, by sitting on-resonance and repeating the LEP/SLC experimental program, we can determine all of the Z''s couplings to fermions. A much more likely scenario is that $M_{Z'} > \sqrt{s}$ so that deviations in the cross section and associated asymmetries for various flavors could be used to look for *indirect* Z' effects in a manner similar to the observation of the Z at PEP, PETRA, and TRISTAN below the resonance. In some cases, this indirect 'reach' can be as large as $M_{Z'} \simeq 10\sqrt{s}$. Figure 0.46 shows a comparison of the indirect Z' search capability at LEP and the NLC as well as the direct production reach at the Tevatron and LHC for several extended models.

If a Z' exists, we would like to know how it couples to the various flavors so that we can identify the correct extended gauge structure. If the Z' is seen at the LHC and its mass is not much larger than about 1 TeV, several analyses have shown [91] that the LHC and a $\sqrt{s} = 500$ GeV NLC will nicely complement each other in extracting fermion coupling information. If the Z' is more massive, then LHC cannot perform coupling analyses using any of the presently available techniques either due to backgrounds or statistical limitations. However, if the mass of the Z' is less than about 2 TeV, then the NLC running in the $\sqrt{s} = 0.5 - 1$ TeV range can obtain significant coupling information even if the Z' is missed by the LHC and its mass is *a priori* unknown. (This value goes up to $M_{Z'} \simeq 3$ TeV if $\sqrt{s} = 1.5$ TeV energies are available.) A representative example of such an analysis is shown in Fig. 0.47 [92]. Similar results can be obtained for different values of the input

parameters as well as for the other fermion flavors (although less observables are available), thus allowing the structure of the extended gauge model to be determined by comparing the extracted values of these couplings with specific model predictions.

In generic Standard Model extensions, the new gauge bosons are usually accompanied by additional fermionic and/or bosonic degrees of freedom the most common of which are either vector-like or singlets with respect to the Standard Model electroweak group. In addition to new quarks and leptons, some of these particles, such as leptoquarks(LQs) and diquarks, may have atypical B- and L-number assignments. The production and decay of both spin-0 and spin-1 LQs at ep, e^+e^-, and $pp/p\overline{p}$ colliders has been studied by many groups [91, 92]. Allowing for both helicities in their interactions with ordinary quarks and leptons there are 14 possible species of LQs with reasonably strict constraints applicable to their intergenerational couplings. (Low energy constraints also force LQ couplings to be chiral.) At ep colliders, LQ production rates are proportional to the squares of unknown Yukawa couplings so they may easily be missed. By contrast, at hadron colliders, the cross section is the same for all LQ types of a given spin but the signal depends upon how the LQ decays. Thus it will not be possible at hadron colliders to uniquely determine which LQ type is being produced. On the other hand, at e^+e^- machines, the production cross sections and asymmetries are determined solely by the LQ electroweak quantum numbers and spin. Several studies have shown [91] that the LQ species can found and identified in both e^+e^- and γe collisions. In the first case the 'ID reach' is $\simeq 0.45\sqrt{s}$; this improves to $\simeq 0.8\sqrt{s}$ in the γe mode if the Yukawa couplings are of order electromagnetic strength. In a manner similar to the Z' searches discussed above, $t-$ and $u-$channel LQ exchange can be probed for indirectly via the process $e^+e^- \rightarrow q\overline{q}$ provided the Yukawa couplings are sufficiently large. For electromagnetic strength couplings the reach can exceed 6 TeV at the NLC.

Table 0.11 shows a comparison of the search capabilities of LEPII, the Tevatron, the LHC and NLC for a number of different exotic particles. As is clear from the above, great care should be exercised when comparing the capabilities of different machines to find and explore the properties of exotics. The results in the table for e^+e^- colliders are indirect bounds for Z''s but represent direct production limits at hadron colliders. Limits on all other particles in the case of e^+e^- colliders are for direct production except where noted. It is important to remember that in many other cases e^+e^- colliders provide important indirect bounds as in both the Z' and LQ examples. For a W' in the Left-Right Symmetric Model (W_R), a number of additional assumptions are required before search reaches can be quoted for hadron colliders; these are: (i) equal left- and right-handed gauge couplings and CKM matrices, (ii) right-handed neutrinos appear only as missing p_t, (iii) only Standard Model final states are accessible in decays. The possibility of surrendering any or all of these assumptions has been analyzed and was found to lead to downward, potentially drastic, alterations in search expectations via the Drell-Yan process. Searches for new quarks at hadron colliders are also subject to decay mode assumptions and are species dependent. In some cases, for example, flavor changing neutral current decays are at least as important as the more conventional charged current ones.

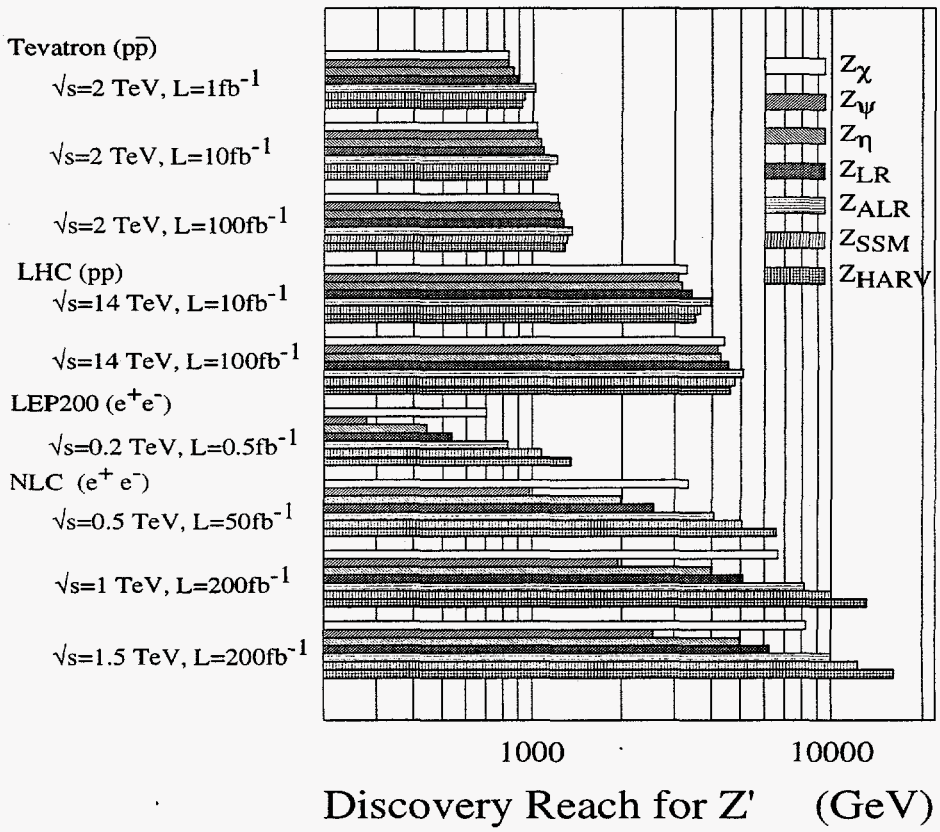

Figure 0.46: Tevatron and LHC bounds are based on 10 events in the $e^+e^- + \mu^+\mu^-$ channels; decays to SM final states only is assumed. LEP and NLC bounds are 99% CL using the observables σ_l, $R^{\rm had}$, A^l_{LR} and $A^{\rm had}_{LR}$.

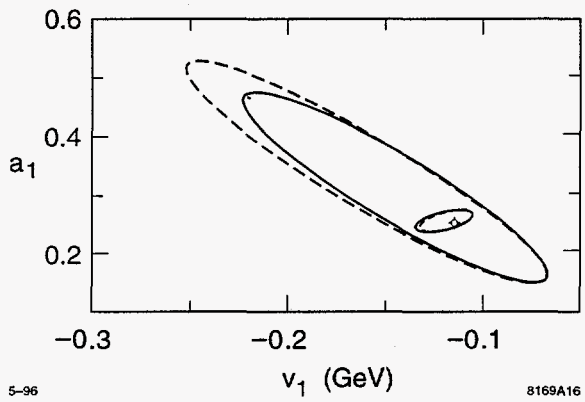

Figure 0.47: Extracted leptonic couplings of a 1.53 TeV Z' at the NLC, at 95% CL, using data at $0.5(70fb^{-1})$, $0.75(100fb^{-1})$, and 1 TeV$(150fb^{-1})$. All leptonic observables were used and generation independence was assumed. The large ovals are applicable when $M_{Z'}$ is unknown a priori and must be obtained from the fit; the solid (dashed) curve corresponds to electron beam polarization $P = 90(80)\%$. The small ovals correspond to the scenario in which $M_{Z'}$ is known (for example, from the LHC); the two curves represent the same two cases. The diamond represents the input values of the couplings.

Table 0.11: Limits and excluded regions in GeV. Run II is $2fb^{-1}$ at 2 TeV; NLC is $200fb^{-1}$; LHC is 14 TeV and $100fb^{-1}$. Z' limits at hadron colliders assume only SM final states are accessible. Z' limits at e^+e^- colliders are indirect. * is the Tevatron limit assuming the standard W' search assumptions. † limit applies when none of the conditions in text are fulfilled; †† result using Z' bound and LR model relationships. $^+$ is from single production. The limit is for first generation spin-0,1 LQs at HERA and the Tevatron including Run 1b estimate; similar numbers will hold for the 2nd generation case at hadron colliders. In the dilepton, diquark and LQ cases, EM strength Yukawas are assumed. $^{++}$ are indirect limits from $e^+e^- \to q\bar{q}$ with these EM strength Yukawas. ** combines several search modes. ‡ is from $e^+e^- \to 2\gamma$. * implies the limit is highly decay mode dependent. The value of '60' as the present limit for the last four entries reflect approximate LEP1.4 null searches. New lepton limits are for both charged and neutral cases. Many entries are estimates.

Particle	Present	LEPII	TeV(Run II)	LHC	NLC(1 TeV)
Z'_{SM}	650	1070	1020	4760	10000
Z'_χ	425	703	910	4380	6670
Z'_ψ	415	278	910	4180	1940
Z'_η	440	443	940	4280	3980
$Z'_{LR}(\kappa = 1)$	445	538	970	4520	5090
Z'_{ALRM}	420	820	1100	5080	8150
W_R	720^*,$300^\dagger$	90	990,$400^\dagger$	5310,$1500^{\dagger\dagger}$	800^+
LQ(spin-0)	180	90,160^+,700^{++}	300,400^{++}	1400,1700^{++}	500,900^+,6000^{++}
LQ(spin-1)	300	90,160^+	440,500^{++}	2200,2500^{++}	500,900^+,$?^{++}$
Axigluon	200-930	150?	1160	5000?	800
E_6 diquark	280-350	90	200-570	5000	500
q^*	90-750^{**}	90,180^+	820	5000-6000?	500,900^+
e^*	60,$127^\ddagger$	90,$180?^+$	500?	4000	500,900^+
new leptons	60	90	??	1000	500
new quarks	60	90	*	*	500
dileptons	60	90	–	–	900^+

0.9 e^-e^-, $e^-\gamma$, and $\gamma\gamma$ Interactions

Up to this point, we have concentrated on the reactions available at the NLC in e^+e^- collisions. However, it is possible with a linear electron collider to study more general processes, and, in fact, to collide e^-, e^+, and γ beams in any combination. A photon beam with substantial brightness at high energy can be created by Compton backscattering of a laser beam from the electron beam. At least for the e^- and γ combinations, the polarizations of the two beams can be controlled independently. The energy spectrum of the backscattered Compton photon beam depends on the relative electron and laser beam polarization the manner shown in Fig. 0.48. Thus, polarization is also useful in tuning the γ energy spectrum, for example, to produce a peak at a fixed energy.

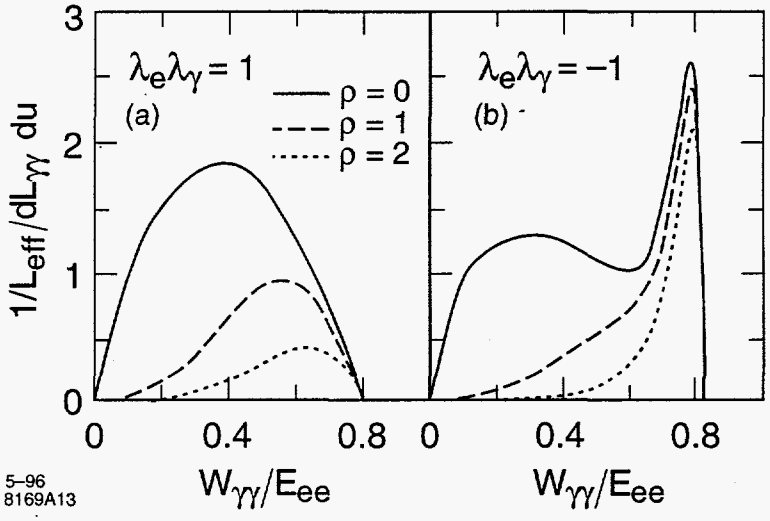

Figure 0.48: $\gamma\gamma$ luminosity for two different combinations of photon and electron polarization, and several values of ρ, the ratio of the intrinsic spread of the photon and electron beams.

The availability of these additional initial states at the NLC adds significantly to the overall physics program. We have already noted their role in the study of Higgs bosons, anomalous electroweak couplings, and strong WW scattering. The exotic quantum numbers of the e^-e^- initial state and the quasi-hadronic nature of the photon also permit searches not available to e^+e^- annihilation. Table 0.12 illustrates the variety of physics issues that have been discussed for each of these modes. The physics expectations for e^-e^- and $\gamma\gamma$ colliders have been recently been reviewed in specialized workshops [93, 94].

In this report, we give special consideration to the possibility of measuring the Higgs boson coupling to $\gamma\gamma$ by creating the Higgs boson as a resonance in $\gamma\gamma$ scattering. We will then review a number of other physics topics which are special to e^-e^- or $\gamma\gamma$ reactions. We conclude this section with a discussion of the expectations for the luminosity and the interaction region design for these reactions.

Table 0.12: A listing of topics that will be investigated at a TeV-level linear collider. Check marks show which different initial states contribute prominently to their study, highlighting the unique contributions that e^-e^-, $e^-\gamma$, and $\gamma\gamma$ options will be able to make.

	QCD	$t\bar{t}$	H	SUSY	Anomalous Couplings	e^*	ν_M	Z'	X^{--}
e^-e^-			√	√	√	√	√	√	√
e^+e^-	√	√	√	√	√			√	
$e^-\gamma$	√		√	√	√	√			√
$\gamma\gamma$	√	√	√	√	√				

0.9.1 Higgs Boson Studies

A photon linear collider provides a clean method to search for an intermediate mass Higgs boson, via the reactions $\gamma\gamma \rightarrow H \rightarrow b\bar{b}$ or ZZ. It is complementary to searches using hadron and e^+e^- machines, being sensitive to different models and couplings. More importantly, a $\gamma\gamma$ linear collider permits a direct measurement of the two-photon width of the Higgs. The coupling of the Higgs boson to two photons involves loops in which any charged fermion or boson with couplings to the Higgs must contribute. The dominant contributions come from species heavier than that Higgs boson. Thus, a measurement of the two-photon width is quite sensitive to new physics even at higher mass scales. Supersymmetric models, and other extensions of the standard model with more complicated Higgs sectors typically predict Higgs spectra and two-photon couplings which differ substantially from those of the standard model [95]. In the minimal supersymmetric model (MSSM), the heavy neutral bosons A^0 and H^0 can be studied for to higher masses than in the e^+e^- mode [96]. In technicolor models, in which Higgs bosons are composite, there are often light CP-odd bound states with cross sections for $\gamma\gamma$ production similar to those of elementary Higgs bosons [97]. Finally, the dependence of the Higgs production on the photon polarization tests the CP properties of the Higgs boson, and may reveal CP violation in the Higgs sector [57, 98].

For a standard model Higgs boson with mass below about 300 GeV, the beam energy spread of a $\gamma\gamma$ collider is much greater than the total width of the Higgs boson, and so the number of $H \rightarrow X(=b\bar{b}, WW, ZZ)$ events expected is

$$N_{H\rightarrow X} = \left.\frac{dL_{\gamma\gamma,J_z=0}}{dW_{\gamma\gamma}}\right|_{M_H} \frac{4\,\pi^2\,\Gamma(H\rightarrow\gamma\gamma)\,B(H\rightarrow X)\,(1+\lambda_1\lambda_2)}{M_H^2}, \qquad (0.11)$$

where $W_{\gamma\gamma}$ is the two-photon invariant mass. Note that since the Higgs boson has spin zero, the initial photons must be in a $J_Z = 0$ state. Event rates for Higgs production and decay into the three primary final states of interest are shown in Fig. 0.49 [99].

In the intermediate mass region (< 150 GeV) the Higgs decays dominantly to $b\bar{b}$. With vertex tagging to remove the backgrounds from light quark production, the most important

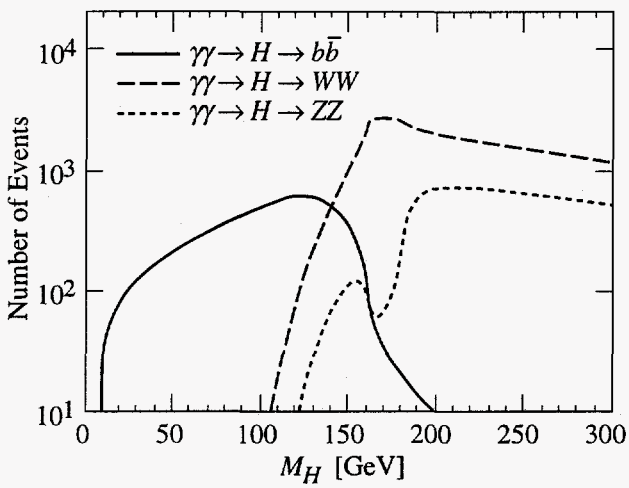

Figure 0.49: Event rates for $\gamma\gamma \to H \to b\bar{b}$ and $\gamma\gamma \to H \to WW, ZZ$, assuming a luminosity function of 4×10^{-2} fb^{-1}/GeV and $\lambda_1\lambda_2 = 1$.

backgrounds arise from continuum production of heavy quarks. These backgrounds are quite large, but can be actively suppressed by exploiting the polarization dependence of their cross-sections, which are dominated by the $J_z = \pm 2$ configurations of initial photons, and by the use of angular cuts. Additional event shape and jet width cuts must be used to suppress radiative processes [100].

Several additional potential backgrounds might fake the presence of a Higgs boson with mass close to the Z mass. The most important of these is the reaction $e\gamma \to eZ \to eb\bar{b}$, initiated by a residual electron left over from the original Compton backscatter. To avoid this background, it will be necessary to sweep these spent electrons away from the interaction point. The process $\gamma\gamma \to f\bar{f}Z$, where the $f\bar{f}$ go down the beam pipe and the Z decays to $b\bar{b}$ provides a background of the same order of magnitude as that of a ≈ 90 GeV Higgs signal [101]. These backgrounds are less important if the mass of the Higgs boson is known a priori, for example, from its observation in $e^+e^- \to ZH$.

For Higgs boson masses above about 150 GeV, the dominant Higgs decay is to WW, where one of the W's may be virtual. However, the large continuum cross section is not easily suppressed, so the WW final state will be a difficult one to use for doing Higgs physics. Fortunately, the ZZ or ZZ^* decay channel can be utilized. Except for Higgs masses between the WW and ZZ thresholds, the Higgs has a branching fraction into this channel of approximately 1/3 into this mode, while the standard model cross section for $\gamma\gamma \to ZZ$ is small. Hadronic decays of the Z bosons predominate, but the huge $\gamma\gamma \to WW$ cross section results in a large number of background events in which both W's are misidentified as Z's. Thus, to tag the Higgs unambiguously, it is necessary to require that at least one Z decays leptonically. For Higgs masses above about 350 GeV, the $\gamma\gamma \to ZZ$ continuum background

becomes large and makes detection of the Higgs very difficult [102].

Detailed Monte Carlo studies [99, 103] indicate that it should be possible to measure the two-photon width of a Higgs to a precision better than 10% over most of the mass range up to 250 GeV. Measurements of this quality should distinguish among many of the competing models for Higgs production. Further discrimination will be supplied if several Higgs bosons can be detected and their $\Gamma_{\gamma\gamma}$ values obtained.

For e^-e^- collisions, we note that the Standard Model Higgs signals from the reactions $e^-e^- \to e^-e^-H, e^-e^-ZH$, and $e^-\nu_e W^-H$ have cross sections of order 10% of the leading modes for the e^+e^- initial state. Moreover, in the intermediate mass range where $H \to b\bar{b}$ decays dominate, there are effective cuts which lead to very clean data samples [104]. For $m_H > 200$ GeV, the process $e^-e^- \to e^-e^-H$ via ZZ fusion becomes a very favorable discovery channel for the Higgs: It overtakes the process $e^+e^- \to ZH$ in cross-section with rising $\sqrt{s}$, and the background rejection is more effective than in $e^+e^- \to H\nu\nu$ via WW fusion because there is no missing momentum and both electrons can be detected [105]. In certain models with extended gauge symmetries, e^-e^- collisions also offer the possibility of double Higgs production H^-H^- [106] doubly-charged Higgs production (H^{--}) [107].

0.9.2 Other New Physics Signatures

Experiments on e^-e^-, $e^-\gamma$, and $\gamma\gamma$ collisions can also give additional insight into many of the other physics topics we have discussed. In the study of the top quark, for example, the $e^-\gamma$ reactions offers the possibility of creating top quarks singly in a well-controlled way through $e^-\gamma \to \nu\bar{t}b$. This reaction has been suggested as a method for obtaining a very accurate value of V_{tb} [108].

In supersymmetric theories, the reaction $e^-e^- \to \tilde{e}^-\tilde{e}^-$ is a promising mode for the discovery and study of the selectron. In regions of parameter space where the neutralinos are heavy or degenerate, this reaction has the advantage of exceptionally low background [109]. In addition, since it proceeds by neutralino exchange, the cross section for this reaction can be used to measure the neutralino masses and mixings. If the selectron is heavy, the kinematic reach for its discovery can be extended by searching for single selectron production via $e^-\gamma \to \tilde{e}\tilde{\gamma} \to e\tilde{\gamma}\tilde{\gamma}$ [110].

We have discussed the utility of $e^-\gamma$ and $\gamma\gamma$ collisions in the study of anomalous W couplings at the Section 6.4. In Section 7.2, we have pointed out the importance of the reaction $e^-e^- \to \nu\bar{\nu}W^-W^-$ in the general program of studies of a strongly interacting Higgs sector. We should also point out the possibility of studying WW scattering at $\gamma\gamma$ colliders. The probability for a photon to branch into a virtual W^+W^- is large at high energies. Thus, it is interesting to observe the process $\gamma\gamma \to W^+W^-W^+W^-$ and to use the spectator W's at relatively low transverse momentum to define the kinematics of a hard WW scattering process. It has been shown that it is possible to extract a significant signal for the scattering of longitudinal W bosons in $\gamma\gamma$ collisions at 1.5 TeV [111, 112].

In the study of exotic particles and extended gauge groups, there are many interesting

reactions which are probed most easily in e^-e^- scattering. If heavy Majorana neutrino exist and mix with the Standard Model neutrinos, the reaction $e^-e^- \to W^-W^-$ might have a significant cross section, estimated at 150 events/$100fb^{-1}$ at a 1 TeV NLC [113]. This process would directly probe lepton number violating couplings. If the gauge group is just $SU(2) \times U(1)$, the signal should appear only in the specific polarization state $e_L^- e_L^-$. Unified models in which the three generations are embedded into a single representation of the gauge group predict the existence of gauge bosons with dilepton quantum numbers. These can be discovered as s-channel peaks in e^-e^- scattering [114]. An $e^-\gamma$ collider can also be sensitive to dilepton gauge bosons over almost the whole mass region less than $\sqrt{s}$, down to coupling strengths as small as $10^{-4}\alpha$ [115]. Other exotic states such as leptoquark bosons can be studied in $e^-\gamma$ and $\gamma\gamma$ reactions in a manner which complements their observation in e^+e^- annihilation [116]. In particular, models of leptoquark bosons typically predict zeros in the angular distribution for production in $e^-\gamma$, and the identification of these features can be a powerful tool in discriminating different models [117].

Finally, Møller scattering at high energy is an ideal way to search for lepton compositeness and other sources of lepton contact interactions. For example, with 50 fb^{-1} of data and 90% polarized beams, the measurement of $e^-e^- \to e^-e^-$ can establish a 95% confidence limit on the electron compositeness parameter Λ_{LL}^+ of 140 TeV [118]. Similarly, the sensitivity to the presence of a Z' boson is somewhat greater in Møller scattering than in Bhabha scattering at the same energy and luminosity [119, 120], though e^+e^- annihilation offers many additional channels to study. The $e^-\gamma$ option allows for searches for excited electrons via $e^-\gamma \to e^* \to e^-\gamma$ which are sensitive almost up to the kinematic limit for couplings of size $10^{-5}\alpha$, and the $\gamma\gamma$ option offers similar sensitivity up to masses of $0.7\sqrt{s}$ for excited lepton searches in $\gamma\gamma \to ee^*, \mu\mu*, \tau\tau*$ [121].

0.9.3 Accelerator, Lasers, and the Interaction Region

As will be explained in Chapter 3, the NLC will include a bend before the interaction region to remove muon and other lower-energy background in the beam. Thus, it is possible to have two interaction regions, one on each side of the linear accelerator. It is natural to design one of these interaction region to be optimized for $e^-\gamma$ and $\gamma\gamma$ collision. Since these modes require e^-e^- beams to allow complete control of the polarization [122], it is natural to carry out e^-e^- experiments also in this separate region and also consider a final focus configuration optimized for e^-e^- running. The detailed design of this interaction region has been begun in [1]. We now summarize some of the design considerations.

Of the three reactions to be studied in this interaction region, e^-e^- is the easiest to realize. The major difference from e^+e^- is that the like charges of the beams causes a repulsion which tends to reduce the luminosity by about a factor of 3 relative to the e^+e^- design if no adjustment is made in the final focus. In the $\gamma\gamma$ and $e^-\gamma$ cases, there is an inefficiency in converting an electron beams to a photon beam and preserving the tiny spot size required to achieve high luminosity. On the other hand, photon beams do not have a

strong beam-beam interaction with beamstrahlung radiation and e^+e^- pair creation, so it is possible to recover part of what is lost by colliding more intense beams and by making the beams round rather than flat, as required for e^+e^- operation. For an e^+e^- collider capable of producing a luminosity of 5×10^{33} cm^{-1}sec^{-1}, a reasonable goal would be to obtain luminosities of 2.5×10^{33} cm^{-1}sec^{-1} in e^-e^-, 3×10^{33} cm^{-1}sec^{-1} in $e^-\gamma$, and 10^{33} cm^{-1}sec^{-1} in $\gamma\gamma$. In the γ reactions, this goal refers to the luminosity within a 10% band width in center of mass energy.

To produce a γ beam by Compton backscattering from an electron beam, the final focus must accommodate a system of mirrors designed to focus light from intense laser beams onto Compton conversion points located about 5 mm from the interaction point. The laser required for the Compton conversion must have tens of kilowatts of average power, compressed to a peak power of 1 Terawatt in a pulse matched to the electron bunch. A wavelength of about 1 micron is required, with close to 100% polarization. The laser pulse timing should match that of the electron beam. Such a laser could be built by either combining diode pumping and chirped pulse amplification in solid state lasers or by a free electron laser driven by an induction linac and using chirped pulse amplification. We note that the SLAC experiment E-144 [123] has succeeded in creating Terawatt laser pulses, at a repetition rate of about 1 Hz, and has demonstrated their collisions with the beam spot of the Final Focus Test Beam.

Round beams are required both to maximize the luminosity and to match the laser beam profile at the conversion point. Focussing with $\beta_x^* = \beta_y^* \approx 0.5$ mm would produce a beam spot size $\sigma_x^{CP} = 718$ nm, $\sigma_y^{CP} = 91$ nm at the conversion point. For these conditions, the Compton conversion efficiency is about 65% per beam, so the luminosity in $\gamma\gamma$ collisions is necessarily less then 40% of the geometric luminosity. Only about 20% of this is in the spectral peak at high energy shown in Fig. 0.48), so the resulting luminosity in high-energy $\gamma\gamma$ collisions is about 10% of the geometrical expectation. After Compton scattering, the degraded electrons continue towards the interaction point and must be deflected when e^-e^- or $e^-\gamma$ collisions are not desired. The simplest way of doing this is to bring the beams together with a small vertical offset ($\approx 1\sigma_y$), and then rely on the mutual repulsion of the electrons to bend these away. There are alternative proposals which involve using a small sweeping magnet or plasma lens near the interaction point; these will require more study to see if they can be implemented without degrading luminosity and detector performance. The dispersion of the degraded electrons also requires a somewhat larger crossing angle (currently estimated as 30 mrad) at the interaction point than is planned for e^+e^- collisions.

While the inclusion of the hardware of the interaction region puts some special requirements on the second detector, the physics goals demand performance to that in e^+e^-. Certain backgrounds may be more severe, especially those due to the spent electron beams. Luminosity monitoring will require special, low-angle detectors for Møller scattering in e^-e^- mode and for $\gamma\gamma \to \ell^+\ell^-$.

0.10 Precision Tests of QCD

Tests of QCD are both enriching and essential to the program of measurements to be made at the NLC. Since QCD *is* our theory of strong interactions it would be irresponsible not to test it at the highest energy scales available in different hard scattering processes. But in addition, the precise determination of the strong coupling α_s is key to a better understanding of high energy physics. For example, the current precision of $\alpha_s(m_Z^2)$ measurements, limited to 5–10%, results in the dominant uncertainty on our prediction of the energy scale at which grand unification of the strong, weak and electromagnetic forces takes place [124]. Measurements of hadronic event properties at high energies, combined with existing lower energy data, would allow one to test the gauge structure of QCD by searching for anomalous 'running' of observables, such as the 3-jet event rate, and to set limits on models which predict such effects, for example those involving light gluinos. Gluon radiation in $t\bar{t}$ events is expected to be strongly regulated by the large mass and width of the top quark; $t\bar{t}g$ events will hence provide an exciting new domain for QCD studies. Conversely, measurements of gluon radiation patterns in $t\bar{t}g$ events may provide valuable additional constraints on the top quark decay width. In addition, searches could be made for anomalous chromo-electric and chromo-magnetic moments of top quarks, which modify the rate and pattern of gluon radiation and for which the phase space increases as the c.m. energy is raised. Finally, polarized electron beams could be exploited to allow tests of symmetries using multi-jet final states.

0.10.1 Precise Measurement of α_s

Tests of QCD can be quantified in terms of the consistency of values of the yardstick $\alpha_s(m_Z^2)$ measured in different experiments. Measurements of $\alpha_s(m_Z^2)$ have been performed over a range of Q^2 from roughly 1 to 10^4 GeV^2 [125], and are consistent within the errors; an average yields $\alpha_s(m_Z^2) = 0.117 \pm 0.006$, implying that QCD has been tested to a precision of about 5%, which is modest compared with the achievement of sub-1% level tests of the electroweak theory. This is due primarily to the *theoretical uncertainties* that dominate the measurements. These uncertainties are due to both the restriction of perturbative QCD calculations to low order, and non-perturbative ('hadronization') effects that are presently incalculable in QCD. We consider whether a measurement of $\alpha_s(m_Z^2)$ at the 1%–level of precision is possible at the NLC by extrapolation of a recent measurement from e^+e^- annihilation at the Z^0 resonance by the SLD Collaboration, based on 15 hadronic event shape observables measured with a sample of 50,000 hadronic events [126]:

$$\alpha_s(m_Z^2) \quad = \quad 0.1200 \pm 0.0025\ (\text{exp.}) \pm 0.0078\ (\text{theor.})\ . \tag{0.12}$$

In this expression, the experimental error is composed of statistical and systematic components of about ± 0.001 and ± 0.002 respectively, and the theoretical uncertainty has components of ± 0.003 and ± 0.007 arising from hadronization and missing higher order terms, respectively.

Based on this experience, we can estimate the errors to be expected for a similar measurement of α_s at a 500 GeV NLC as follows:

Statistical error: At design luminosity, the NLC would deliver roughly 200,000 $q\overline{q}$ (q=u,d,s,c,b) events per year implying that a statistical error on $\alpha_s(m_Z^2)$ of about $\pm$ 0.0005 could be obtained. Cuts for rejection of W^+W^- and $t\bar{t}$ backgrounds, based on kinematic information and as well as beam polarization and b-tagging, will not substantially reduce the $q\overline{q}$ sample size.

Systematic error: This results primarily from the uncertainty in modeling the jet resolution of the detector. The situation may be improved at the NLC both from an improved calorimeter and from the naturally improved calorimeter energy resolution for higher energy jets. It is not unreasonable to suppose that the current systematic error of ± 0.002 could be reduced by a factor of two, but more convincing demonstration of this point would require a simulation of the detector, as well as the event selection and analysis cuts [127].

Hadronization uncertainty: Since jets of hadrons, rather than partons, are observed in detectors it is necessary to correct hadronic distributions for any smearing and bias effects that occur in the hadronization process. Such corrections are usually estimated from Monte Carlo simulations incorporating hadronization models and in Z^0 decays are typically at the level of 10% [126]. Webber has argued [128] that non-perturbative corrections to jet final states in e^+e^- annihilation can be parametrized in terms of inverse powers of the hard scale Q, and that for a generic observable X the ratio of non-perturbative to perturbative QCD contributions is dominated by a term of the form:

$$\frac{\delta X^{\text{non-pert}}}{X^{\text{pert}}} \sim \frac{\ell n Q}{Q} . \tag{0.13}$$

Increasing Q from 91 GeV to 500 GeV decreases this ratio by a factor of 5, implying that hadronization corrections should be of order 2% at NLC. Assuming that these corrections can be estimated to better than $\pm 50\%$, the hadronization uncertainty on $\alpha_s(m_Z^2)$ should be less than ± 0.001.

Uncertainty due to missing higher orders: Currently perturbative QCD calculations of hadronic event measures are available complete up to $\mathcal{O}(\alpha_s^2)$. Since the data contain knowledge of all orders one must estimate the possible bias inherent in measuring $\alpha_s(m_Z^2)$ using the truncated QCD series. It is customary to estimate this from the dependence of the fitted $\alpha_s(m_Z^2)$ on the QCD renormalization scale, yielding a large and dominant uncertainty of about ± 0.007 [3]. At 500 GeV this uncertainty will be reduced only slightly to ± 0.006.

Summary: From this simple analysis it seems reasonable to conclude that achievement of the luminosity necessary for 'discovery potential' at the NLC will result in a $q\overline{q}$ event sample of sufficient size to measure $\alpha_s(m_Z^2)$ with a statistical uncertainty of better than 1%. Construction of detectors superior in performance to those in operation today should enable reduction of systematic errors to the 1% level. Hadronization effects should be significantly smaller and imply a sub–1% uncertainty. The missing ingredient for an overall 1%-level $\alpha_s(m_Z^2)$ measurement at 500 GeV is the calculation of $\mathcal{O}(\alpha_s^3)$ perturbative QCD contributions, which should be actively pursued.

0.10.2 Energy Evolution Studies

The non-Abelian gauge structure of QCD implies that the strong coupling decreases roughly as $1/\ell n\, Q$. Existing hadronic final states data from e^+e^- annihilation at the PETRA, PEP, TRISTAN, SLC and LEP colliders span the range $14 \leq Q \leq 91$ GeV, although hadronization uncertainties are large on the data below 25 GeV [6]. A 2 TeV NLC would increase the lever-arm in $1/\ell n\, Q$ by almost a factor of two, allowing detailed study of the energy evolution of QCD observables proportional to α_s, such as the rate of 3-jet production R_3. This would provide not only a test of the fundamental structure of the $SU(3)_c$ group, but also a search-ground for new physics that might produce 'anomalous' running. One such possibility is the existence of a light, electrically neutral colored fermion that couples to gluons, for example, a light gluino. The existence of such a particle would manifest itself via a modification of gluon vacuum polarization contributions involving fermion loops, effectively increasing the number of light fermion flavors N_f entering into the QCD β-function. For the case of a light gluino, which leads to a 10% increase in the value of R_3 at 500 Gev, a 1% measurement of α_s would allow this effect to be detected with a significance of many standard deviations.

However, data from experiments at different e^+e^- colliders contributing to this analysis, some of which were recorded more than 10 years ago, were treated differently by the various experimental groups, and have relatively large systematic errors that are at least partly uncorrelated from point to point. It is clear that the precision of searches for anomalous running of QCD observables at NLC would be improved significantly if new data were taken at lower c.m. energies with the *same* detector and analysis procedures. Table 0.13 shows the number of $q\overline{q}$ events delivered per day at various c.m. energies by the NLC operating at design luminosity; more luminosity would be delivered per day than was recorded in total by the original lower energy colliders! The ability to maintain high luminosity at low center of mass energies presents a formidable challenge to the design of the collider, but even running at lower luminosity could deliver substantial data samples, especially at the Z^0, although the high event rates would present extreme requirements on the triggering and data processing capabilities of the detector.

Table 0.13: $q\overline{q}$ events per day delivered by NLC at design luminosity

CM Energy Q (GeV)	$q\overline{q}$ events/day
500	1750
91	20,000,000
60	75,000
35	150,000

0.10.3 Symmetry Tests Using Beam Polarization

For polarized e^+e^- annihilation to three hadronic jets one can define the triple-product $\vec{S_B} \cdot (\vec{k_1} \times \vec{k_2})$ ($B = \gamma, Z^0$), which correlates the boson polarization vector $\vec{S_B}$ with the normal to the three-jet plane defined by $\vec{k_1}$ and $\vec{k_2}$, the momenta of the highest- and the second-highest-energy jets respectively. The triple-product is even under reversal of CP, and odd under T_N, where T_N reverses momenta and spin-vectors without exchanging initial and final states. Standard Model T_N-odd contributions of this form at the Z^0 resonance have been investigated [129] and are found to be of order $\beta \sim 10^{-5}$; the first experimental study of this quantity has been made by SLD [130], yielding limits: $-0.022 < \beta < 0.039$. Above the Z^0 the dominant Standard Model contributions remain smaller than 2 parts in 10^5, presenting a background-free observable for new contributions from beyond the Standard Model, for example, due to rescattering of new gauge bosons that couple only to baryon number [131].

0.10.4 Gluon Radiation in $t\bar{t}$ Events; Anomalous Couplings

The large mass and decay width of the top quark serve to make the study of gluon radiation in $t\bar{t}$ events a new arena for testing QCD. The mass m_t acts as a cutoff for collinear gluon radiation, and the width Γ_t acts as a cutoff for soft gluon radiation, allowing reliable perturbative QCD calculations to be performed. We have noted in Section 3.1 the influence of the large top quark width on the rate and pattern of gluon radiation in $t\bar{t}$ events.

The existence of anomalous couplings of top quarks to gluons could manifest itself via a modification of the rate and pattern of emitted gluon radiation, beyond effects such as those just discussed. A parametrization of anomalous couplings in the strong-interaction Lagrangian may be written:

$$\mathcal{L}^{q\bar{q}g} = g_s \bar{q} T_a \left(\gamma_\mu + \frac{i\sigma_{\mu\nu} k^\nu}{2m_t} (\kappa - i\tilde{\kappa}\gamma_5) \right) q G_a^\mu \qquad (0.14)$$

where κ and $\tilde{\kappa}$ represent anomalous 'chromomagnetic' and 'chromoelectric' dipole moments, respectively. The chromoelectric moment gives rise to CP-violating effects; the chromomagnetic case has been calculated at leading order in α_s [132]. At $Q = 1$ TeV limits at the level of $|\kappa| \leq 0.1$ appear possible. Ignoring theoretical uncertainties, limits of comparable statistical precision may be obtainable from measurement of the $t\bar{t}$ cross section at the Tevatron with 10 times the current integrated luminosity. Comparable limits from LHC would require a $t\bar{t}$ cross section measurement to better than $\pm 20\%$.

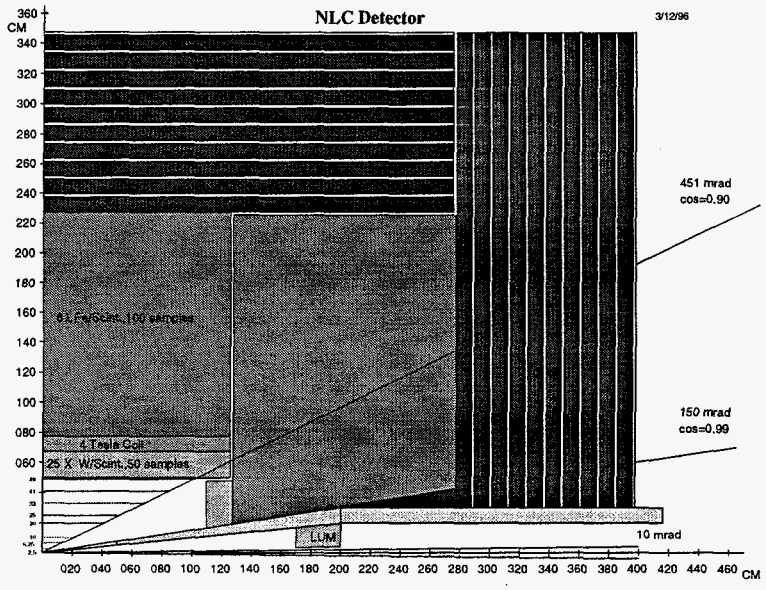

Figure 0.50: NLC Detector.

0.11 Design of the NLC Detector

Now that we have described the expected physics program of the NLC, we must discuss in more detail what experimental facilities should be necessary. In this section, we will present a sample design of an NLC detector and discuss the general issues which constrain this design. This detector takes into account the particular features of the NLC accelerator and its machine-related backgrounds. A more complete discussion of the machine/detector interaction is given at the end of Chapter 3.

A general plan of a detector for the NLC is shown, in quadrant view, in Fig. 0.50. This detector is at a very early conceptual design stage. The architecture is a "standard" solenoid, and is just one possible approach. A 3 or 4 layer CCD vertex detector surrounds a beryllium vacuum pipe. The momentum measurement is carried out by layers of silicon microstrip detectors in a 4 Tesla field, which is produced by a superconducting solenoid outside of the electromagnetic calorimeter. A hadronic calorimeter is located outside the coil, and the structure is wrapped in laminated iron for a flux return and muon identification system. The final focus quadrupoles are located inside the detector at an L^* of 2m. A summary of the components and expected performance of the detector is given in Table 0.14.

The small volume 4 Tesla field is well matched to the expected backgrounds, cost, and technology. The small size of the tracking system eases the mechanical problem of stabilizing the final focus elements relative to one another at the required nanometer level. However, this design increases the complexity of the elements inside the detector. For example, the final quadrupoles, envisioned as permanent magnets, would have to be shielded by a small super conducting solenoid. The tracking system is modeled as 5 layers of Si microstrips with 5 micron spatial resolution. The expected momentum resolution, including multiple

Table 0.14: Basic Components of the NLC Detector

Vertex	$3-5$ CCD Layers $2.6 \oplus (13.7/p\sin^{3/2}\theta)$
Tracking	5 Si Layers $\lvert\cos\theta\rvert \leq 0.9$ $\delta p_T/p_T = 2\times 10^{-4}$ at 100 GeV at $\cos\theta = 0.9$
Coil	4T, 2–3 X_0
EM Calorimeter	$25X_0$, 50 samples $\frac{\sigma_E/E=12\%}{\sqrt{E\sin\theta}\oplus 1\%}$
Hadronic Calorimeter	Fe Scintillator 6λ, 100 samples $\sigma_E/E = (45\%/\sqrt{E}) \oplus 2\%$
Return Flux	6λ, 10 samples

scattering, is shown in Figure 0.51. Agreement that this performance is a reasonable match to the physics goals is probably the most important question for the overall detector design. The cylindrical layers extend to $\cos\theta = 0.9$. This leaves sufficient space for the ends of the support structure, electronics, cabling, and cooling. End cap trackers could be added for improved coverage. Experience with SLC/SLD confirms the idea that backgrounds from a linear collider can be very severe for conventional wire chambers. A silicon strip system would be extremely robust.

The electromagnetic calorimeter would be inside the coil, 25 radiation lengths thick, and with angular segmentation in the range of 30 to 40 mrad^2. Possible structures include tungsten scintillator sampling towers and BGO or perhaps more exotic crystals. The crystals would be interesting not so much for their good resolution but for their lack of interconnections. The calorimetry is extended by endcaps to $\cos\theta = 0.99$.

The superconducting coil has an inner radius of 70 cm and a half length of 1.2 m. Since there are only weak constraints on the thickness of the coil, given that it is outside the electromagnetic calorimeter, and since it is a relatively small coil, it should be a reasonable coil to design and build. This design will be made more challenging, however, by its required integration with the quadrupole shields and supports.

The hadronic calorimeter is assumed to be an iron scintillator sampling system, 6λ thick and 100 samples. At this time, no magnetic modeling of the structure has been done. It is unclear whether the advantages of an iron based calorimeter in containing the magnetic flux would be outweighed by the structural problems.

Finally, the detector is wrapped in a flux return 6λ thick with 10 layers for muon detectors.

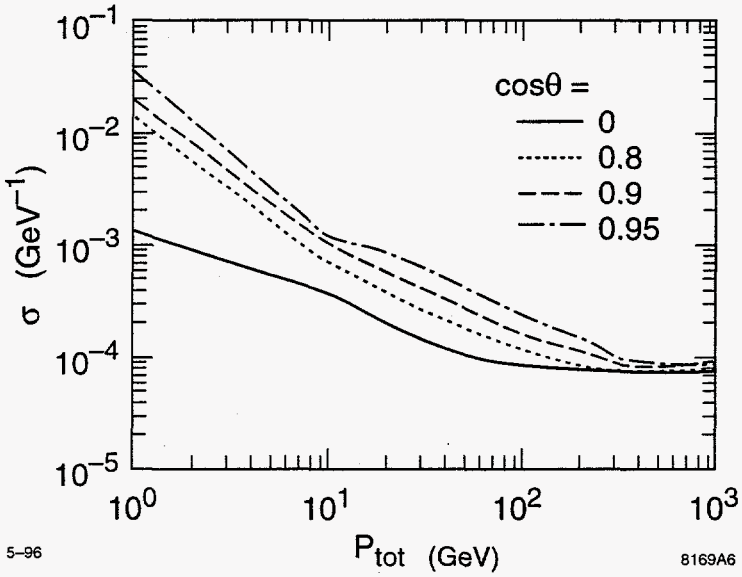

Figure 0.51: NLC Detector tracking parameters.

Questions of overall geometry for internal access and vibration control are completely open.

The crossing of the two beams at the interaction point produces an irreducible e^+e^- pair background at small $p_\perp$. These particles can be kept away from a small radius vertex detector by the relatively high 4 Tesla magnetic field. A reasonable vertex detector for this environment would be a successor to the SLD vertex detector using large area CCDs with 20 micron square pixels. The CCDs could be read out in a time equivalent to a small number of beam crossings, and the beams could be suppressed subsequent to a trigger if necessary. At SLD the innermost layer of the vertex detector, at $r = 2.5$ cm with $B = 0.6$ T, sees 0.4 hits/mm^2 summed over its 19 machine pulse readout time. Vertex hits are successfully attached to tracks extrapolated from a conventional drift chamber whose closest wire is at $r = 22$ cm. Thus a conservative estimate for the tolerable background is 1 hit/mm^2. Were the NLC vertex detector to extrapolate hits from its own high resolution outer layers into an inner layer, the much smaller search area would allow a much larger (10-20 hits/mm^2) background to be tolerated.

Fig. 0.52 shows the hit density from the e^+e^- pair background, per bunch train (a series of 90 bunch collisions), at a radius of 3 cm and at 2 cm. The results are shown as a function of z for a 4 Tesla field. At $r = 3$ cm the background is nonexistant out to $z = 45$ cm. At $r = 2$ cm the background is similar to that tolerated by an existing detector out to $z = 17$ cm, a length adequate to provide vertexing coverage well beyond the $\cos\theta = 0.90$ currently used in the physics simulations.

In addition to the irreducible background of pairs emanating from the interaction point, the vertex detector will see a background of very low energy backscattered particles resulting from the interaction of the pairs that have been curled up by the field and gone forward to

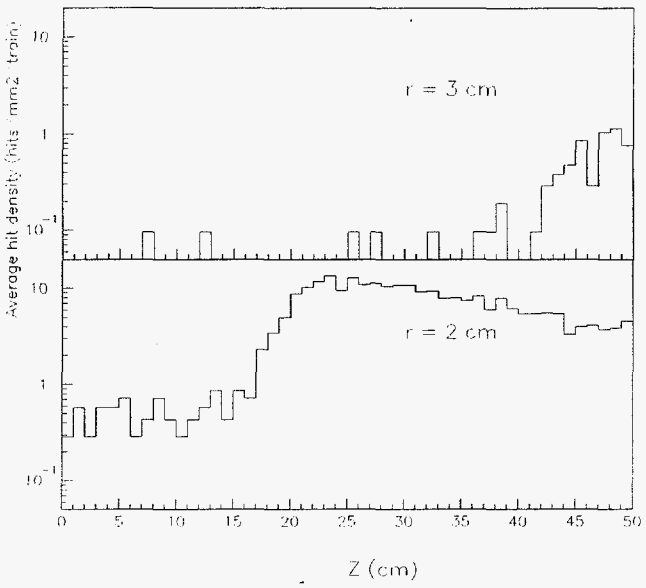

Figure 0.52: Electron pair hit density per mm^2 per train of 90 bunches, computed with the Monte Carlo program ABEL. As the pairs leave the IP in a 4 Tesla field, hits are scored (a) at $r = 3$ cm, and (b) at $r = 2$ cm.

strike the quad faces, septum, and luminosity monitor. In the current interaction region design the calculated rate is 2.0 hits/mm^2/train at $r = 3$ cm, flat in z, and roughly constant down to $r = 2$ cm, then rising at lower radii. This background rate, already sufficiently low at $r = 2$ cm for efficient vertexing, is very sensitive to the details of the interaction region design. Efforts to reduce the flux of these soft particles, by, for instance, the use of low-Z coatings, are underway.

As experience in the collider operation is gained, one may want to consider vertex detection at smaller radii. Even at the very aggressive radius of 1 cm, in a 4 Tesla field the pair background hit rate remains below 10/mm^2/train out to $z = 3$ cm. Moreover, since the tracking system radius largely drives the scale of the entire detector, a small tracker permits consideration of relatively small L^* as a possible future upgrade of the final focus design. The small L^* is plausible because the axial extent of the tracker is small, about 1m for $\cos\theta < 0.9$. This leads to significant improvements in required tolerances in the final focus system.

0.12 Physics Processes which Constrain Detector Performance

In general, the requirements of the NLC physics program do not put strong constraints on the detector design and performance. For most physics analyses, the performance of the detectors constructed for SLC and LEP would be quite sufficient. These detectors already include the basic requirements for the study of e^+e^- annihilation at high energy: calorimetry with good energy resolution, segmentation, and charged lepton identification; tracking with high momentum resolution, good forward angular acceptance and overall granularity; and excellent secondary vertex tagging. However, it is always interesting to consider advanced detectors with improved performance in one or another of these areas. In this section, we enumerate those physics topics which put exceptional or unusual demands on the detector and which might motivate a more advanced detector design.

A basic benchmark for detector performance is that given by standard model Higgs production in the all-hadronic mode: $e^+e^- \to Zh \to jj + b\bar{b}$. This sets a standard of hadronic energy resolution, angular coverage for high acceptance, and b-tagging efficiency. The recognition of the Z in its hadronic decay is required, more generally, for high-statistics branching ratio determinations for the Higgs boson.

For the Higgs boson of the Minimal Supersymmetric Model, it is possible for the Higgs boson to decay by mechanisms very different from those of the Standard Model. The interesting mode $e^+e^- \to hA \to b\bar{b}b\bar{b}$ places a premium on angular coverage and efficiency of b-tagging. More generally, it is important in this theory to be able to recognize the production of the Higgs boson in $e^+e^- \to Zh$ making as few assumptions as possible on the final state to which the Higgs decays. Such a model-independent search for the Higgs boson is possible if the Z can be reconstructed as an $\ell^+\ell^-$ pair superimposed on any reasonable Higgs boson final state. This analysis constrains the momentum resolution and two-track separation of the tracking device.

For studies of the W boson vertices in $e^+e^- \to W^+W^-$, it is necessary to completely reconstruct the final state kinematics by measurement of a lepton + 2 jet system. This would seems to demand high-quality tracking. However, it has been shown that the tracking requirements are less severe if kinematic fitting is used to determine the jet energies [83].

In the study of WW scattering, the reactions $e^+e^- \to \nu\bar{\nu}WW$ and $e^+e^- \to \nu\bar{\nu}ZZ$ give signatures for distinct models of a strongly interacting Higgs sector, as explained in Section 7.2. Thus, it is necessary to distinguish these processes experimentally. Because the event rate is rather small, it is necessary to rely on detection of W and Z in their hadronic decay modes. Thus, it is important that the calorimetric mass resolution for W and Z be sufficiently small that these particles can be distinguished on the basis of their masses. The analysis discussed in Section 7.2 assumed a probability of about 10% for confusing each W for a Z or vice versa [88]. In addition, this analysis requires good forward coverage for high-energy electrons and positrons, to remove background from the processes $e^+e^- \to e^+e^-W^+W^-$ and $e^+e^- \to e\nu WZ$ which are induced by virtual photons.

Finally, we note that the study of the top quark threshold is affected by the energy spread of the e^+e^- collisions, which is determined by the accelerator design. For this study to be carried out optimally, the beam energy spread from beamstrahlung should be kept to the level of initial state radation, about 3%, and the intrinsic beam energy spread of the accelerator should be kept to 0.1%. These requirements are quite reasonable for the machine design discussed in Chapter 3. In addition, since the differential luminosity spectrum depends on the beam parameters, it is necessary to measure this directly. This requires the measurement of acollinearity angles in small-angle Bhabha scattering to better than 1 mrad for $\theta \sim 200$–500 mrad. The detector design in Section 11 includes an appropriate electromagnetic shower detector placed inside the synchrotron radiation mask.

0.13 Conclusions

The Standard Model of strong and electroweak interactions represents a tremendous scientific achievement. It provides an elegant and well tested description of fundamental forces based on underlying local symmetry concepts. However, despite those successes, some basic questions remain unanswered. Addressing those issues should guide us to a deeper understanding and better appreciation of Nature's laws.

What is the origin of electroweak symmetry breaking and mass generation? That outstanding problem drives high energy physics and establishes its experimental goals. Fortunately, resolution of that puzzle appears to be within reach of the next generation of hadron and lepton colliders, the LHC and the NLC.

In this report, we have described some of the physics goals and capabilities of the NLC, emphasizing both its unique features and complementarity to the LHC program planned at CERN. The envisioned project would start with an initial variable center-of-mass energy up to about 500 GeV and be upgradable to 1–1.5 TeV. It would feature a highly polarized e^- beam as well as e^-e^-, γe^- and $\gamma\gamma$ collider options.

The first phase of the NLC guarantees extensive physics capabilities and interesting discovery potential. Sitting at and above the $t\bar{t}$ threshold will allow unprecedented precision measurements of the top quark's mass, partial decay widths, gauge and Higgs boson couplings etc. Its very large mass may be a signal of the top quark's special role in elementary particle physics and electroweak symmetry breaking. We must, therefore, explore its properties and search for additional anomalous features. In that endeavor, the LHC will be a top quark factory, capable of producing and studying samples of order 10^7 tops in a number of characteristic signatures. The NLC will complement such studies as a precision instrument which is sensitive to the broad range of top couplings to strong and weak gauge bosons. Similarly, studies of gauge boson pair production at the NLC will provide high precision measurements of triple-gauge boson couplings at the level of 1–0.1% (with increasing center-of-mass energy). At that level of sensitivity anomalous properties could become unveiled, particularly if there is new strong dynamics at ~ 1 TeV.

If a fundamental Higgs scalar exists and has mass below 350 GeV, it will be found and studied in the first phase of the NLC via $e^+e^- \to ZH$. That mass reach is extremely broad and encompasses a most important domain. If the Standard Model is perturbative up to grand-unification energies, then $m_H \lesssim 200$ GeV. If supersymmetry is manifested at the electroweak scale, then the lightest scalar satisfies $m_h < 150$ GeV. The first stage of the NLC will be definitive in confirming or negating those expectations. A higher mass Higgs (> 350 GeV) would be easily accessed at the LHC or higher energy phases of NLC. Additional Higgs scalars of SUSY scenarios, or pseudo-Goldstone bosons of dynamical symmetry breaking schemes, would be unveiled in pair-production unveiled as their thresholds are passed at the NLC. The clean environment of that facility would allow detailed studies of their decay patterns. A compelling feature of e^+e^- colliders is the ability to not only produce new particles, but to thoroughly explore their properties.

If supersymmetry manifests itself near the electroweak scale, a plethora of new particles, the supersymmetric partners of quark, leptons, and gauge bosons, awaits discovery. Unfolding that entire spectrum and its properties will require the full capabilities of the LHC and NLC. The first direct evidence for production of gluinos and squarks should be found at LHC, if not already at the Tevatron. On the other hand, the study of color-singlet superpartners is best carried out at e^+e^- colliders. Since these particles are typically lighter, they determine the decay patterns of the particles produced in strong interactions. Thus, the NLC will be essential for unraveling the entire spectrum and precisely measuring the new particle properties. The study of superpartners will be greatly facilitated by use of the high e^- polarization both for suppressing backgrounds and enhancing signals. High precision determinations of SUSY parameters will provide important insight and constraints on the mechanism of SUSY breaking and as well as a potential new window to the physics of grand unification and superstrings.

If new strong dynamics is responsible for electroweak symmetry breaking, it may be difficult to uncover and fully explore. In such a scenario, the NLC will be an extremely valuable instrument. It will probe the new dynamics via $W^+W^- \to W^+W^-$ and $W^+W^- \to t\bar{t}$ scattering, and through anomalous gauge boson couplings and other probes in $e^+e^- \to W^+W^-$. Such studies will become ever more revealing as the higher energy upgrades are attained. In addition, new strong dynamics is likely to imply a wealth of spectroscopy at very high energies. The NLC, particularly its highest energy phase, should be a very important facility for discovering and studying such states.

The new energy domain opened up by the NLC will also allow systematic searches for new particles such as Z' bosons, heavy fermions, leptoquarks, etc. If such particles are found, the e^- polarization will be extremely useful for deciphering their properties.

The physics capabilities of the NLC can be greatly expanded by the e^-e^-, γe^-, and $\gamma\gamma$ collider options possible at such an accelerator. Those collision modes will complement e^+e^- studies and could prove particularly useful to provide new observables of supersymmetric particles, to study the Higgs boson as an s-channel resonance, and to explore W^-W^- scattering.

During the twentieth century, elementary particle physics emerged as a scientific discipline. Since its inception, progress and advancement have followed our ability to probe shorter distances via high energy collisions. By pushing to even higher energies, we should be able to continue the advancement. In this report, we have reviewed the questions that are now at the frontier of particle physics, and we have shown that the NLC has a central role is answering every one. We thus view the NLC as a forefront facility for particle physics, an essential tool for probing the hidden symmetries of Nature, a well tuned instrument for the start of our next millennium.

Bibliography

[1] NLC ZDR Design Group, *Zeroth Order Design Report for the Next Linear Collider*, SLAC report (1996).

[2] F. Paige and S. Protopopescu, in *Supercollider Physics* (Snowmass 1986), D. Soper, ed. (World Scientific, Singapore, 1986); H. Baer, F. Paige, S. Protopopescu, and X. Tata, in *Proceedings of the Workshop on Physics at Current Accelerators and Supercolliders*, J. Hewett, A. White, and D. Zeppenfeld, eds. (Argonne National Laboratory, 1993).

[3] A. Miyamoto, in *Physics and Experiments with Linear e^+e^- Colliders*, F. A. Harris, S. L. Olsen, S. Pakvasa, and X. Tata, eds. (World Scientific, Singapore, 1993).

[4] C. Ahn *et al.*, *Opportunities and requirements for Experimentation at High Energy e^+e^- Colliders*, SLAC-report-329, May 1988.

[5] T. Sjöstrand, *Comp. Phys. Comm.* **82**, 74 (1994).

[6] T. Barklow, preprint SLAC-PUB-7087, to appear in the proceedings of the Workshop on Physics and Experiments with Linear Collider, LCWS95.

[7] K. Hagiwara, K. Hikasa, R. D. Peccei, D. Zeppenfeld, *Nucl. Phys.* **B282**, 253 (1987).

[8] F. Abe, *et al.* (CDF Collaboration), *Phys. Rev. Lett.* **74**, 2626 (1995); S. Abachi, *et al.* (D0 Collaboration), *Phys. Rev. Lett.* **74**, 2632 (1995).

[9] M. Jezabek, J. H. Kuhn, and T. Teubner, *Z. Phys.* **C56**, 653 (1992).

[10] G. Jikia, *Phys. Lett.* **B257**, 196 (1991).

[11] V. A. Khoze, L. H. Orr, and W.J. Stirling, *Nucl. Phys.* **B378**, 413 (1992).

[12] K. Fujii, T. Matsui, and Y. Sumino, *Phys. Rev.* **D50**, 4341 (1994).

[13] M. Strassler and M. Peskin, *Phys. Rev.* **D43**, 1500 (1991).

[14] V. Fadin and V. Khoze, *JETP Lett.* **46**, 525 (1987), *Sov. J. Nucl. Phys.* **48**, 309 (1988).

[15] Y. Sumino, K. Fujii, K. Hagiwara, H. Murayama, and C.-K. Ng, *Phys. Rev.* **D47**, 56 (1993); M. Jezabek, J. Kuhn, and T. Teubner, *Z. Phys.* **C56**, 653 (1992).

[16] P. Igo-Kemenes, M. Martinez, R. Miquel, and S. Orteu, in *Physics and Experiments with Linear e^+e^- Colliders*, F. A. Harris, S. L. Olsen, S. Pakvasa, and X. Tata, eds. (World Scientific, Singapore, 1993).

[17] H. Murayama and Y. Sumino, *Phys. Rev.* **D47**, 82 (1993).

[18] W. Bernreuther and M. Suzuki, *Rev. Mod. Phys.* **63**, 313 (1991).

[19] G. A. Ladinsky and C. P. Yuan, *Phys. Rev* **D49**, 1994 (4415); and references therein.

[20] R. Harlander, M. Jezabek, J. H. Kuhn, and T. Teubner, *Phys. Lett.* **B346**, 137 (1995); R. Harlander, M. Jezabek, J. H. Kuhn, and M. Peter, hep-ph/9604328.

[21] S. Parke and Y. Shadmi, preprint FERMILAB-PUB–96/042-T.

[22] R. Frey, preprint SLAC-PUB-7075, to appear in the proceedings of the Workshop on Physics and Experiments with Linear Colliders, LCWS95.

[23] C. R. Schmidt, preprint hep-ph/9504434.

[24] ATLAS Collaboration, Technical Proposal. CERN/LHC/94-43.

[25] R. Harlander, M. Jezabek, and J. H. Kühn, preprint hep-ph/9506292.

[26] A. Djouadi, J. Kalinowski and P. M. Zerwas, *Z. Phys.* **C54**, 255 (1992).

[27] P. Comas, R. Miquel, M. Martinez, and S. Orteu, preprint CERN-PPE/96-40, to appear in the proceedings of the Workshop on Physics and Experiments with Linear Colliders, LCWS95.

[28] K. Fujii, to appear in the proceedings of the 1995 SLAC Summer Institute.

[29] S. Bar-Shalom, D. Atwood, G. Eilam, R. Mendel, and A. Soni, *Phys. Rev.* **D53**, 1162 (1996).

[30] D. Amidei and R. Brock, eds., *Future ElectroWeak Physics at the Fermilab Tevatron*, FERMILAB-PUB-96/046.

[31] C. R. Schmidt and M. E. Peskin, *Phys. Rev. Lett.* **69**, 410 (1992).

[32] C.-P. Yuan, *Mod. Phys. Lett.* **A10**, 627 (1995).

[33] P. W. Higgs, *Phys. Lett.* **12**, 132 (1964).

[34] J. F. Gunion, H. E. Haber, G. L. Kane and S. Dawson, *The Higgs Hunter's Guide* (Addison-Wesley, Redwood City, 1990).

[35] J. F. Gunion, A. Stange and S. Willenbrock, in *Electroweak Symmetry Breaking and New Physics at the TeV Scale*, T. Barklow, S. Dawson, H. Haber, and J. Seigrist, eds. (World Scientific, Singapore, 1996).

[36] H. P. Nilles, *Phys. Repts.* **110**, 1 (1984).

[37] H. Haber and G. Kane, *Phys. Repts.* **117**, 75 (1985).

[38] T. Moroi and Y. Okada, *Phys. Lett.* **B295**, 73 (1992); G. L. Kane, C. Kolda, J. D. Wells, *Phys. Rev. Lett.* **70**, 2686 (1993).

[39] J. F. Grivaz, preprint LAL-95-83 (1995), to appear in the proceedings of the International Europhysics conference on High Energy Physics, Brussels, 1995.

[40] D. Abbaneo, *et al.*(LEP Electroweak Working Group) and E. Etion, *et al.*(LEP Heavy Flavor Group), preprint LEPEWWG/96-01.

[41] M. Carena and P. Zerwas *et al.*, *Higgs Physics*, to appear in the proceedings of the LEP2 Workshop, CERN Yellow Report, eds. G. Altarelli *et al.*

[42] S. Mrenna and G. L. Kane, preprint hep-ph/9406337.

[43] G. L. Kane, G. D. Kribs, S. P. Martin, and J. D. Wells, *Phys. Rev.* **D53**, 213 (1996).

[44] P. Janot, in *Physics and Experiments with Linear e^+e^- Colliders*, F. A. Harris, S. L. Olsen, S. Pakvasa, and X. Tata, eds. (World Scientific, Singapore, 1993).

[45] J. Gunion, in *Physics and Experiments with Linear e^+e^- Colliders*, F. A. Harris, S. L. Olsen, S. Pakvasa, and X. Tata, eds. (World Scientific, Singapore, 1993).

[46] S. Komamiya, in *Physics and Experiments with Linear Colliders*, R. Orava, P. Eerola, and M.Nordberg, eds. (World Scientific, Singapore, 1992); H.E. Haber, *ibid.*; J.-F. Grivaz, in *e^+e^- Collisions at 500 GeV: The Physics Potential*, P. M. Zerwas, ed., DESY-92-123.

[47] Y. Fujii, in *Physics and Experiments with Linear e^+e^- Colliders*, F. A. Harris, S. L. Olsen, S. Pakvasa, and X. Tata, eds. (World Scientific, Singapore, 1993); JLC-1 Design Report, KEK Report 92-16.

[48] P. Janot, in *Physics and Experiments with Linear Colliders* F. A. Harris, World Scientific, 1993, eds. F.A. Harris *et al.*, Waikoloa, Hawaii.

[49] M. D. Hildreth, T. L. Barklow, and D. L. Burke, *Phys. Rev.* **D49**, 3441 (1993).

[50] P. Burchat, D. Burke, and A. Petersen, *Phys. Rev.* **D38** (1988) 2735; J. Alexander, *et al.*, in *High Energy Physics in the 1990s* (Snowmass 1988), S. Jensen, ed. (World Scientific, Singapore, 1989); F. Richard, in *Proceedings of the Workshop on Physics at Future Accelerators* (La Thuile), CERN 87-07, 1987.

[51] A. Djouadi, W. Kilian, and P. Ohmann, preprint hep-ph/9512312, to appear in the proceedings of the Workshop on Physics and Experiments with Linear Collider, LCWS95.

[52] M. Carena, J. R. Espinosa, M. Quiros, and C. E. M. Wagner, *Phys. Lett.* **B335**, 209 (1995); M. Carena, M. Quiros, and C. E. M. Wagner, *Nucl. Phys.* **B461**, 1996 (;) H. E. Haber, R. Hempfling, and A. H. Hoang, preprint CERN-TH-95-216.

[53] A. Sopczak, *Charged Higgs Boson Discovery Potential at a 500 GeV e^+e^- Linear Collider*, CERN-PPE/93-197; A. Sopczak, in *e^+e^- Collisions at 500 GeV: The Physics Potential*, P. M. Zerwas, ed., DESY-93-123C.

[54] J. Rosiek and A. Sopczak, *Phys. Lett.* **B341**, 419 (1995).

[55] K. Kawagoe, in *Physics and Experiments with Linear e^+e^- Colliders*, F. A. Harris, S. L. Olsen, S. Pakvasa, and X. Tata, eds. (World Scientific, Singapore, 1993).

[56] B. Grządkowski and J. F. Gunion, *Phys. Lett* **B350**, 218 (1995).

[57] J. F. Gunion and B. Grządkowski, *Phys. Lett.* **B294**, 361 (1992).

[58] J. F. Gunion and J. G. Kelly, *Phys. Lett.* **B333**, 220 (1994).

[59] M. L. Stong, preprint hep-ph/9504345.

[60] H. Haber, preprint hep-ph/9505240.

[61] J. Kamoshita, Y. Okada, and M. Tanaka, preprint hep-ph/9512307.

[62] I. Nakamura and K. Kawagoe, preprint hep-ex/9604010; I. Nakamura, to appear in the proceedings of the Workshop on Physics and Experiments with Linear Colliders, LCWS95.

[63] H. E. Haber, in *Recent Directions in Particle Theory (TASI-92)*, J. Harvey and J. Polchinski, eds. (World Scientific, Singapore, 1993).

[64] H. Murayama, in *Physics with High Energy Colliders*, S. Yamada and T. Ishii, eds. (World Scientific, Singapore, 1995).

[65] M. E. Peskin, preprint hep-ph/9604339, to appear in the proceedings of the Yukawa International Seminar YKIS'95.

[66] R. Arnowitt and P. Nath, contributed paper in this volume.

[67] H. Baer, R. Dubois, S. Fahey, S. Manly, R. Munroe, U. Nauenberg, X. Tata, D. L. Wagner, contributed paper in this volume.

[68] T. Tsukamoto, K. Fujii, H. Murayama, M. Yamaguchi, and Y. Okada, *Phys. Rev.* **D51**, 3153 (1995).

[69] H. Murayama, I. Watanabe,and K. Hagiwara, *HELAS: Helicity Amplitude Subroutines for Feynman Diagram Evaluations*, KEK-91-11 (1992).

[70] R. Becker and C. Vander Velde, in *Physics and Experiments with Linear Colliders*, F. A. Harris, S. L. Olsen, S. Pakvasa, and X. Tata, eds. (World Scientific, Singapore, 1993).

[71] K. Fujii, T. Tsukamoto, and M. M. Nojiri, preprint hep-ph/9511338, to appear in the proceedings of the Workshop on Physics and Experiments with Linear Collider, LCWS95.

[72] J. L. Feng, H. Murayama, M. E. Peskin, and X. Tata, *Phys. Rev.* **D52**, 1418 (1995).

[73] J. L. Feng and D. E. Finnell, *Phys. Rev.* **D49**, 2369 (1994).

[74] H. Baer, C. H. Chen, F. Paige and X. Tata, *Phys. Rev.* **D53**, 6241 (1996).

[75] H. Aihara *et al.*, in *Electroweak Symmetry Breaking and New Physics at the TeV Scale*, T. Barklow, S. Dawson, H. Haber, and J. Seigrist, eds. (World Scientific, Singapore, 1996).

[76] M. Einhorn, in *Physics and Experiments with Linear e^+e^- Colliders*, F. A. Harris, S. L. Olsen, S. Pakvasa, and X. Tata, eds. (World Scientific, Singapore, 1993).

[77] J. Bagger, S. Dawson, and G. Valencia, *Nucl. Phys.* **B399**, 364 (1993).

[78] C. Artz, M.B. Einhorn, and J. Wudka, *Phys. Rev.* **D49**, 1370 (1994).

[79] H. Hagiwara, S. Ishihara, R. Szalapski, and D. Zeppenfeld *Phys. Lett.* **B283**, 353 (1992)

[80] Z. Ajaltouni *et al.*, preprint hep-ph/9601233, to appear in the proceedings of the CERN Workshop on LEP II Physics.

[81] T. L. Barklow, in *Proceedings of the International Symposium on Vector Boson Self-Interactions*, U. Baur, S. Errede, and T. Müller, eds. (American Inst. Press).

[82] T. L. Barklow, in in *Physics and Experiments with Linear Colliders*, R. Orava, P. Eerola, and M.Nordberg, eds. (World Scientific, Singapore, 1992).

[83] K. Riles, contributed paper in this volume.

[84] D. Choudhury and F. Cuypers, *Nucl. Phys.* **B429**, 33 (1994).

[85] S. J. Brodsky, T. G. Rizzo, and I. Schmidt, *D52* **4929**, 1995 (.)

[86] T. L. Barklow, S. Dawson, H. E. Haber, and J. L. Siegrist, in *Particle Physics: Perspectives and Opportunities*, R. Peccei, M. E. Zeller, D. G. Cassel, J. A. Bagger, R. N. Cahn, P. D. Grannis, and F. J. Sciulli, eds. (World Scientific, Singapore, 1995).

[87] M. Peskin, in *Physics in Collisions IV*, A. Seiden, ed. (Éditions Frontières, Gif-Sur-Yvette, 1984).

[88] V. Barger, K. Cheung, T. Han, and R.J.N. Phillips, *Phys. Rev.* **D52**, 3815 (1995).

[89] V. Barger, J. F. Beacom, K. Cheung, and T. Han, *Phys. Rev.* **D50**, 6704 (1994).

[90] R. P. Kauffman, *Phys. Rev.* **D41**, 3343 (1990).

[91] M. Cvetic and S. Godfrey, in *Electroweak Symmetry Breaking and New Physics at the TeV Scale*, T. Barklow, S. Dawson, H. Haber, and J. Seigrist, eds. (World Scientific, Singapore, 1996); A. Djouadi, J. Ng, and T. G. Rizzo, *ibid.*

[92] T. G. Rizzo, contributed paper in this volume.

[93] C. A. Heusch, ed., *Proceedings of the Electron-Electron Linear Collider Workshop*, *Int. J. Mod. Phys.* **11**, 1523 (1996).

[94] *Proceedings of the Workshop on Gamma-Gamma Colliders*, *NIM* **355**, 1 (1995).

[95] J. F. Gunion and H. E. Haber, *Phys. Rev.* **D48**, 5109 (1993).

[96] J. Gunion and J. Kelly, *Phys. Lett.* **B333**, 110 (1994); S. Moretti, *Phys. Rev.* **D50**, 2016 (1994); M. Kramer *et al.*, *Z. Phys.* **C64**, 21 (1994).

[97] J. Tandean, *Phys. Rev.* **D52**, 1398 (1995).

[98] H. Anlauf, W. Bernreuther, and A. Brandenberg, *Phys. Rev.* **D52**, 3803 (1995).

[99] D. L. Borden, D. A. Bauer, and D. O. Caldwell, *Phys. Rev.* **D48**, 4018 (1993).

[100] D. L. Borden V. A. Khoze, W. J. Stirling, and J. Ohnemus, *Phys. Rev.* **D50**, 4499 (1994).

[101] I. F. Ginzburg and V. G. Serbo, *Phys. Rev.* **D49**, 2623 (1994).

[102] G. V. Jikia, *Phys. Lett.* **B298**, 224 (1993), *Nucl. Phys.* **B405**, 24 (1993).

[103] O. J. P. Eboli, M. C. Gonzalez-Garcia, F. Halzen, and D. Zeppenfeld, *Phys. Rev.* **D48**, 1430 (1993); M. Baillargeon, G. Belanger, and F. Boudjema, *Phys. Rev.* **D51**, 4712 (1995).

[104] T. Han, *Int. J. Mod. Phys.* **11**, 1541 (1996).

[105] K. Hikasa, *Phys. Lett.* **B164**, 1985 (.)

[106] T. Rizzo, *Int. J. Mod. Phys.* **11**, 1563 (1996).

[107] J. F. Gunion, *Int. J. Mod. Phys.* **11**, 1551 (1996).

[108] N. V. Dokholyan and G. V. Jikia, *Nucl. Phys.* **B374**, 83 (1992).

[109] F. Cuypers G. J. van Odenborgh, and R. Ruckl, *Nucl. Phys.* **B409**, 128 (1993).

[110] D. Choudhury and F. Cuypers, *Nucl. Phys.* **B451**, 16 (1995).

[111] S. J. Brodsky, in *Physics and Experiments with Linear e^+e^- Colliders*, F. A. Harris, S. L. Olsen, S. Pakvasa, and X. Tata, eds. (World Scientific, Singapore, 1993).

[112] K. Cheung, *Phys. Lett.* **B323**, 85 (1994).

[113] C. A. Heusch and P. Minkowski, *Nucl. Phys.* **B416**, 1 (1994).

[114] P. H. Frampton, *Phys. Rev. Lett.* **69**, 2889 (1992).

[115] N. Leporé, B. Thorndyke, H. Nadeau, and D. London, *Phys. Rev.* **D50**, 2031 (1994).

[116] H. Nadeau and D. London, *Phys. Rev.* **D47**, 3742 (1993); G. Bélanger, D. London, and H. Nadeau, *Phys. Rev.* **D49**, 3140 (1994).

[117] F. Cuypers, preprint hep-ph/9508397.

[118] T. Barklow, *Int. J. Mod. Phys.* **11**, 1579 (1996).

[119] D. Choudhury, F. Cuypers, and A. Leike, *Phys. Lett.* **B333**, 531 (1994).

[120] F. Cuypers, *Int. J. Mod. Phys.* **11**, 1571 (1996), preprint hep-ph/9602426.

[121] F. Boudjema, A. Djouadi, and J. L. Kneur, *Z. Phys.* **C57**, 425 (1993).

[122] V. Telnov, *NIM* **A355**, 3 (1995).

[123] J. G. Heinrich, *et al.*, SLAC Proposal E-144 (1991).

[124] P. Langacker and N. Polonsky, *Phys. Rev.* **D47**, 4028 (1993), *Phys. Rev.* **D52**, 3081 (1995).

[125] S. Bethke, *Nucl. Phys.* **B** Proc. Suppl. **39C**, 198 (1995).

[126] K. Abe *et al.* (SLD Collaboration), *Phys. Rev.* **D51**, 962 (1995).

[127] S. Bethke, in *Physics and Experiments with Linear e^+e^- Colliders*, F. A. Harris, S. L. Olsen, S. Pakvasa, and X. Tata, eds. (World Scientific, Singapore, 1993).

[128] B. R. Webber, preprint hep-ph/9411384. (1994).

[129] A. Brandenburg, L. Dixon, and Y. Shadmi, *Phys. Rev.* **D53**, 1264 (1996).

[130] K. Abe *et al.* (SLD Collaboration), *Phys. Rev. Lett.* **74**, 4173 (1995).

[131] C. Carone and H. Murayama, *Phys. Rev. Lett.* **74**, 3122 (1995); D. Bailey and S. Davidson, *Phys. Lett.* **B348**, 185 (1995).

[132] T. G. Rizzo, *Phys. Rev.* **D50**, 4478 (1994).